8-2013

# Mobile Robot Navigation for Person Following in Indoor Environments

Ninad Pradhan
*Clemson University*, npradha@g.clemson.edu

# Mobile Robot Navigation for Person Following in Indoor Environments

A Dissertation
Presented to
the Graduate School of
Clemson University

In Partial Fulfillment
of the Requirements for the Degree
Doctor of Philosophy
Computer Engineering

by
Ninad Pradhan
August 2013

# Abstract

Service robotics is a rapidly growing area of interest in robotics research. Service robots inhabit human-populated environments and carry out specific tasks. The goal of this dissertation is to develop a service robot capable of following a human leader around populated indoor environments. A classification system for person followers is proposed such that it clearly defines the expected interaction between the leader and the robotic follower. In populated environments, the robot needs to be able to detect and identify its leader and track the leader through occlusions, a common characteristic of populated spaces. An appearance-based person descriptor, which augments the Kinect skeletal tracker, is developed and its performance in detecting and overcoming short and long-term leader occlusions is demonstrated. While following its leader, the robot has to ensure that it does not collide with stationary and moving obstacles, including other humans, in the environment. This requirement necessitates the use of a systematic navigation algorithm. A modified version of navigation function path planning, called the predictive fields path planner, is developed. This path planner models the motion of obstacles, uses a simplified representation of practical workspaces, and generates bounded, stable control inputs which guide the robot to its desired position without collisions with obstacles. The predictive fields path planner is experimentally verified on a non-person follower system and then integrated into the robot navigation module of the person follower system. To navigate the robot, it is necessary to localize it within its environment. A mapping approach based on depth data from the Kinect RGB-D sensor is used in generating a local map of the environment. The map is generated by combining inter-frame rotation and translation estimates based on scan generation and dead reckoning respectively. Thus, a complete mobile robot navigation system for person following in indoor environments is presented.

# Dedication

*To my parents, for their love and sacrifice.*

*To my sister Meeta, for her altruism and compassion.*

*To Kaveri, without whom it would be impossible to see any part of this become reality.*

# Acknowledgments

My advisors, Dr. Burg and Dr. Birchfield, were kind enough to accept mentoring me during my Ph.D., and I thank them for helping me understand the complexity of research. There were times where I was myopic about my own research and, looking back, I realize how incomplete this dissertation would be without their encouragement to never lose sight of the bigger picture.

Dr. Walker and Dr. Woodard were always available for advice and feedback, and the points they raised during my proposal presentation went a long way towards providing corrective inputs for the final outcome. During my collaboration with Dr. Neeraj Gohad, I benefited from his insights and his passion and excitement for research.

Lane Passalacqua Swanson went out of her way to help me when I had to face the perfect storm of qualifier preparations and medical issues. Having people like her and Elizabeth Gibisch in the department staff has made life easier for me and countless other graduate students. I also thank David Moline and John Hicks for their help on many occasions.

The example of dedication and diligence set by my friends and roommates Nihar Ranjan and Sunil Kumar will stay with me for a long time. We share a love for long discussions and for endless debates. Their humor and congeniality were vital to a great friendship.

From nearly the beginning of my Clemson years, Ravi Joseph Singapogu has been a steadfast friend and a wonderful source of encouragement. He, his wife Rachel, and his children David, Asha, and Priya, have been my window into life beyond the lab in our college town.

Any mention of my Clemson years would be incomplete without of those who I have been lucky to know since the very beginning: Utpal, Ujwal, Lalit, Neha, Radhika, Swapna, Sushant.

Without my colleagues and friends Apoorva Kapadia, Tony Threatt, Jessica Merino, and Bryan Willimon, these past few years would be much less fun.

My research benefited from collaborating or discussing ideas with Brian Peasley and Sean Ficht. Vikram Iyengar, Sumod Mohan, Vidya Gayash, and Nitendra Nath were exemplary in their aptitude and love for research and problem solving.

Rahul Saxena, Raghvendra Cowlagi, and Salil Wadhavkar constantly amaze me with their proficiency and deep insights on diverse topics. They, along with Chetan Danait, Rohit Pradhan, Ananya Sanyal, Abhijeet Malik, and Rajula Subramanian, were a vital part of my undergraduate years and remain close to me still.

In Shripad Kulkarni, Bankim Ghelani, and Aditi Nerikar, I have been lucky to have friends who have been a solid and constant influence in my life for many years.

My family has always shown me the way, and my strengths, such as they might be, can be attributed to the example of my parents, sister, aunt, and grandparents.

Finally, I have been fortunate to have the permanent presence and support of Kaveri, Shamila Thakur-Bhatia, Gautam Bhatia, and Dinesh Thakur through these years.

Such are the many reasons I have been able to write this dissertation.

# Table of Contents

# List of Tables

# List of Figures

# Chapter 1

# Introduction

As robots make a gradual transition from industrial settings to household or personal applications, direct interaction between humans and robots has become an emerging area of research. In this dissertation, a person following mobile robotic system is developed and its results presented.

Person followers are part of the larger robot classification called ‘service robots’ [1]. Service robots are robots which operate in human populated environments and assist people in their daily activities. This is a broad definition which is satisfied by a growing number of robotics systems described in recent literature.

## 1.1 Service robots in recent literature

‘Grace’, developed in 2007 by Kirby et al. [2], was designed to accompany a person around using verbal and non-verbal cues for interaction. Scans from a laser range finder were used to infer the presence and location of a person, with whom the robot communicated using vocalization. The leader was informed by the robot when a change of state, such as the leader stopping or moving out of robot sensor range, was detected. 'Minerva', developed in 2000 by Thrun et al. [3], was designed to act as a tour guide. The robot localized itself relative to a map of its test environment, the Smithsonian Museum of American History. The robot avoided collisions with visitors and executed multiple tours of the museum as a guide. Its predecessor, 'Rhino' [4], developed in 1995 by Buhmann et al., achieved similar objectives of mapping and avoiding collisions in an indoor environment. 'BIRON', developed in 2004 by Haasch et al. [5], is another well known service robot which was designed to actively interact with its user by means of speech and gesture recognition. 'MKR', developed in 2010 by Takahashi et al. [6], is a hospital service robot which transports luggage, specimens, etc. around hospital passages using potential fields for navigation.

Some recent service robotics systems are close to, or already in the process of, commercial production and distribution. Probably the best known of these is the 'Care-o-bot®3', developed in 2009 by Reiser et al. [7]. This robot is equipped with laser range scanners, a vision system, and a 7-DOF (Degrees-of-freedom) manipulator arm. One typical application of this robot is to serve as a robotic butler. For example, a customer may ask for a drink using a touchscreen on the robot. The robot then identifies the requested object in the inventory of bottles or cans using an object recognition module, and the grasping mechanism then lifts the correct object and the robot returns to the customer to serve it. This robot is a typical example of integrating various modules to create a useful robotic system. 'Johnny', developed in 2012 by Breuer et al. [8], can be considered to be another state-of-the-art service robot. Based on the requirements of the RoboCup@Home challenge [9], this robot was designed to serve in a restaurant-like environment, where it received seat reservations, waited on guests, and delivered orders to them.

Providing service and care in domestic environments is a fairly prevalent theme in service robotics research. 'Flo', developed in 2000 by Roy et al. [10], was a service robot designed to interact with people with mild dementia. It was equipped with telepresence software, which would allow remote medical consultation, and with a speech recognition system which would allow the user to communicate with the robot. The robot navigated around an indoor environment by first creating a map using learning techniques and then being able to move to an arbitrary location using this map. ‘CompanionAble’, developed in 2011 by Gross et al. [11], was designed to assist the elderly who suffer from mild cognitive impairment, in home environments. This project was geared towards developing home robots with telepresence and with the capability to detect hazardous events such as falls and using telepresence to allow the patient to communicate with caregivers. With a growing fraction of the elderly living alone in the US [12], such robots are placed to fill a void in the care afforded to this section of the population. ‘Hein II’, developed in 2011 by Tani et al. [13], was designed as a person follower for home oxygen therapy patients. Such patients need to tether around an oxygen supplier tank, which can be physically exhausting. A large number of people in Japan, where this robot was designed, are dependent on home oxygen therapy [14], and such a robotic follower would provide an improvement to their quality of life. Thus service robots, or ‘socially assistive robots’, as they have also been called [15], are gradually maturing into a useful technology.

## 1.2 Person followers

The development of the person following mobile robot system described here was characterized by the same desire to realize a robot capable of interacting with humans in an everyday environment.

An environment populated with humans poses multiple challenges to a robot which seeks to follow a leader within it:

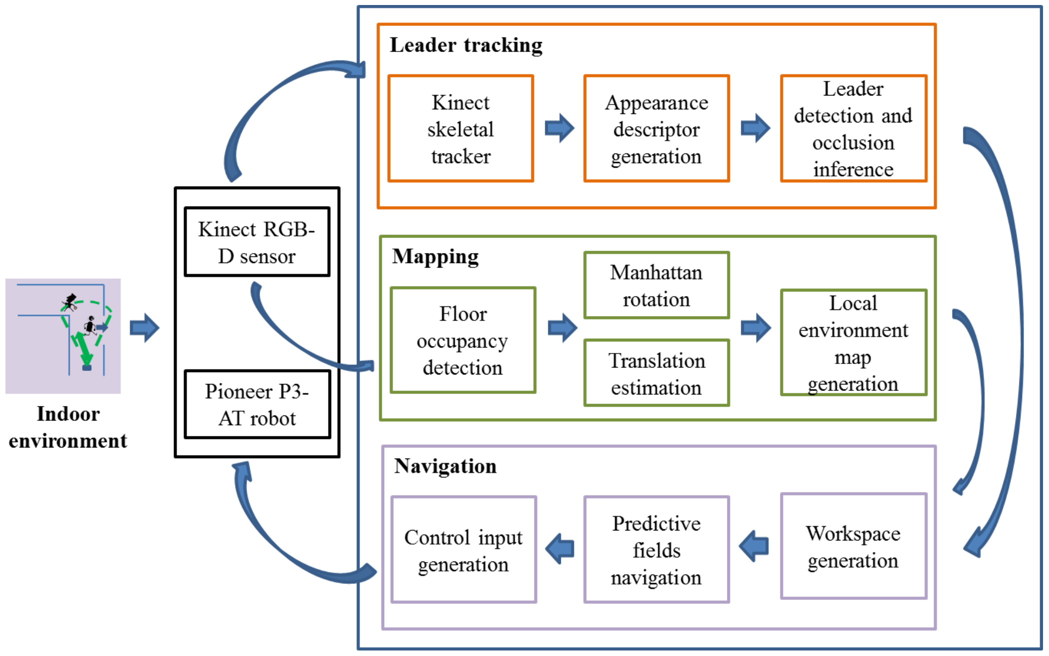

Figure 1.1: Block diagram of the person follower system.

- Detecting and tracking the leader.
- Detecting and handling leader occlusion.
- Avoiding collisions with walls, people, and objects.
- Identifying the local environment of the robot, i.e. mapping.

The person following problem is thus well defined in terms of the tasks which the robot might be expected to carry out. But any scenario in which the leader and the robot are expected to collaborate is incompletely defined until the expectations from *both* the robot and the leader are detailed. In the widely cited work by Yoshimi et al. [16], the expectations from the robot have been outlined in a manner similar to the list enumerated above. But current literature does not address the question of expectations from the leader in the person following system. To address this, in Section 4.1, a classification of person followers based on expected leader behavior or collaboration is proposed. Some contemporary person followers are categorized according to this system to illustrate how it may be used to describe the capabilities of a person following system. When person following service robots become common, the standardization of this or a similar classification system would likely assist human leaders in deciding which one best suits their needs. This will be similar to decisions made about the 'class' of an automobile best suited for a person or household.

A simplified block diagram, developed from the above list of robot requirements, that will be used to guide the development of a new person follower, is given in Figure 1.1. In the rest of this section, developments related to specific modules or capabilities of the proposed person follower are discussed, and specific innovations made while developing the new person following system are highlighted.

### 1.2.1 Leader detection and tracking

Some person followers contain indigenously developed person detection and tracking modules. Chen and Birchfield [17] used a stereo camera pair and a sequential combination of feature tracking, disparity based segmentation, and motion based segmentation (called Binocular Sparse Feature Segmentation) to detect the leader for the system. Tracking KLT features across frames was used to maintain leader position information and follow the leader. Yun [18] used mean-shift color histogram tracking to track the person and potential fields to avoid collision with obstacles. Miura et al. [19, 20] used SVM trained depth templates for person detection. Ma et al. [21] combine a model of upper body clothing using histograms and laser range finder data to track an unoccluded person using an unscented particle filter.

A number of contemporary person followers have used state-of-the-art person detection algorithms for leader detection and tracking. Person or pedestrian detection [22, 23, 24, 25, 26] is an independent research area in computer vision because of its applicability to automobile systems [27, 28, 29], surveillance [30], gaming [31], and analytics [32, 33]. These detectors use either image information, 3D, or a combination of the two to achieve their purpose. Brookshire [34] and Weinrich [35, 36] use Histograms of Oriented Gradients (HOG) [37] for person detection. HOG, one of the landmark contributions in person detection, generates image intensity edge descriptors over image regions and compares them to a trained model to detect a human silhouette. Brookshire [34] develops a system which uses HOG for person detection and stereo for depth estimation. When the leader is thus localized, a particle filter is used to track the leader over outdoor trials. Weinrich et al. [35, 36] generate a SVM decision tree based on HOG detections to detect the upper body orientation of people.

The advent of real time RGB-D sensors such as the Microsoft Kinect has introduced new possibilities in the approach towards person detection and tracking. Depth data, and as a consequence, 3D point clouds, which used to be available only by using a stereo rig or by learning depth from monocular data [38, 39], are now available in the form of raw sensor data. In case of the Kinect, depth and image pixel positions are related to each other through a known transformation, which allows a correspondence to be established between RGB and D. Xia et al. propose a person detection system [40] which leverages this richness of Kinect sensor information.

The Kinect SDK contains an implementation of a person detection and tracking algorithm proposed by Shotton et al. [31]. The algorithm is trained, using a deep randomized forest classifier, to detect human body parts using variation in human depth images without the use of temporal data. Training is carried out on a large synthetic depth dataset representative of variations in the human shape and silhouette. A depth feature is generated at each pixel in the image, and is labeled as belonging to one of multiple joints (20) in the human skeletal representation used by this algorithm. This pixel-wise labeling is used to infer the 3-D position of each joint in the skeletal representation. Thus, given a single depth image, the Kinect skeletal tracker is able to deduce the location and pose of a person. The skeletal tracker is also able to track up to 6 individuals in the field of view of the sensor. The entire detection and tracking sequence has been shown to run at close to 50 fps on a CPU in the original paper [31]. Doisy et al. [41] have used the Kinect skeletal tracker in their person following system.

The Kinect SDK skeletal tracker is a state-of-the-art person tracking technology of choice for our person following system. Over multiple trials, the skeletal tracker was found to be reliable and is well within acceptable range of operation for the person follower described in this dissertation.

Another candidate tracking method, HOG in combination with particle filtering, was also extensively tested. However, HOG detections were less consistent than skeletal tracker detections, especially when the pose of the person changed. Also, particle filter tracks were less reliable than the tracking performance of the skeletal tracker for typical indoor environments with multiple persons walking in front of the robot. Section 4.2.1 gives more information about the capabilities and output of the Kinect skeletal tracker.

### 1.2.2 Occlusion detection and handling

Person detection and tracking systems are not traditionally equipped to handle occlusions and recover from them, though there are a few exceptions [42, 43]. This may be because the scope of applications of these systems, e.g. a generic person counting application in a crowd, may not require assigning 'identity' to an individual and maintaining it through occlusions. However, the question of identity is of primary importance to a person following robot.

Various attempts have been made to ensure that a person follower maintains leader identity. At one end of this spectrum are systems where it is assumed that the leader is unoccluded, which gives the person tracking modules a chance to use motion or color consistency to localize the leader relative to the robot. Yoshimi et al. [16] demonstrate a person following robot which has the leader in sight at all times. Brookshire [34] also assumes this condition is met, and focuses on sensor integration to develop a robot that can follow a person outdoors through variations in illumination conditions and terrain. Hence, these and other comparable systems [18, 41] maintain leader identity by assuming that the leader is always visible, and focus research efforts on other challenges such as motion planning around obstacles or variability in test conditions.

Some systems forego the condition of constant visibility and use motion or color information to keep track of the leader through partial or complete occlusions. Tarokh and Merloti [44] develop a person tracking system which is initialized using a color patch on the person's shirt or top. HSI (Hue-Saturation-Intensity) information is learned from this patch, and in subsequent frames, similar image patches are inferred as being tracked locations of the person. Their algorithm can track and follow a person using vision information through partial occlusions, but makes the assumption that no object of a similar color profile appears in the field of view during a trial. Satake and Miura [20] developed a person follower which uses depth data and a Support Vector Machine (SVM) based verification system to detect people, and leader occlusion is inferred using a difference in leader and occluding person depth. EKF (Extended Kalman Filter) is used for tracking the leader, and once the detected occlusion has passed, leader tracking and following resumes.

Tracking capabilities of the Kinect skeletal tracker are limited in the same sense as many other person tracking systems, i.e. to situations when the person is unoccluded. If a person is occluded and reappears, the skeletal tracker can once again detect and track the person, but it assumes that a new person has appeared in front of the sensor. There is no attempt to recognize or handle occlusions by reidentifying a person. However, the skeletal tracker is excellent at detecting and tracking people in the absence of occlusions.

This reliability in unoccluded tracking is leveraged by the occlusion detection and handling system proposed in Section 4.2. Skeletal information for the initialized robot leader is augmented with a color descriptor. The descriptor is built using HSI and L*a*b* (CIE 1976) color spaces, and extracts color values for each bone detected by the tracker. In each frame, a descriptor is generated for the tracked leader and compared with the initialized descriptor to confirm that the skeletal tracker has correctly kept track of the leader. When the skeletal tracker reports a lost skeletal track, descriptor matching takes over and the robot moves to the last observed leader location in an attempt to reacquire the leader and overcome occlusion. Unlike motion based occlusion handling approaches, the duration of the occlusion is inconsequential.

This ability to overcome occlusions of arbitrary period is very useful for practical human populated environments. Using motion consistency or history to detect the position of the leader is possible only in a limited sense. A simple sequence of events such as the leader pausing when occluded or moving in an entirely different direction can lead to tracking errors in motion-dependent methods. The appearance based occlusion detection and handling method is thus capable of detecting occlusions and recovering after they have been removed. The actual process of overcoming occlusions is carried out by the path planning and navigation module of the system.

### 1.2.3 Robots in populated environments

Robot navigation in sparsely populated indoor environments may be considered to be a subset of the general topic of robot navigation through crowds, which has seen interest in recent literature. Treuille et al. [45] modeled large crowds in a simulated environment. A dynamic potential field method was used to move individual agents in the crowd. This work was later used by Henry et al. [46] as the test environment for their work on robot crowd navigation. Reinforcement learning was used to teach the robot the ‘correct’ method of navigating crowds. After the learning phase was complete, a robot used Gaussian processes to make navigation decisions during runtime. Trautman and Krause [47] also explored the problem of dense crowd navigation using Gaussian processes which modeled interaction between people in crowds to plan a path for the robot in such an environment. Ziebart et al. [48] also demonstrated a robot crowd navigation method for a known workspace, in which data learned over many days is used to infer a motion cost function for places within that environment.

Some of the principles of crowd navigation find an analog in solutions for person following in populated environments. The most important of these might be considered to be a representation of the motion of humans in the scene to improve the robot’s navigation algorithm. Bennewitz et al. [49] learn typical motion patterns of people using a combination of the Expectation Maximization (EM) algorithm with Hidden Markov Model (HMM) used for predicting the person’s position. These forecasted person trajectories are used by the A* algorithm [50] for robot navigation. Weinrich et al. [35] track person motions using a 9-D Kalman filter and project robot and person positions into the future to determine a cost function to help the robot avoid the path of the approaching human. After every interaction, the robot updates parameters of its cost function to keep learning human behavior to improve collision avoidance in the future.

The ability of the robot navigation algorithm to plan a path for the robot after incorporating obstacle motion is very relevant for person followers. It allows the robot to stay at a safe distance relative to other humans while it is navigating towards its leader. However, a number of contemporary person followers do not encode such information in their path planning or navigation modules [16, 18, 41], primarily because the obstacles in question are assumed to be static objects such as furniture or boxes on the floor.

The navigation objectives of a mobile robot person follower in indoor environments may be stated as follows:

- Keep a fixed position relative to the leader.
- Identify obstacles (moving or stationary) which may hinder a direct route to leader.
- Plan a path around obstacles, while avoiding collision with them.

One of the challenges for mobile robot navigation with an onboard camera is the question of self-localization. The robot needs to know where it is situated relative to an absolute coordinate system. Such a representation can be generated by means of a local map of the environment, in which the view of the environment at each frame is stitched together based on an estimate of robot motion between frames. This problem of map generation is commonly called SLAM (Simultaneous Localization and Mapping). A detailed tutorial on the SLAM problem and relevant literature was prepared by Bailey and Durrant-Whyte [51, 52].

Using an RGB-D sensor, the SLAM problem is most commonly solved by using calibrated vision inputs or by using depth-only cues. When calibrated vision inputs are used, the technique for map generation is called visual odometry [53, 54]. Inter-frame correspondence is established using feature correspondences, and knowing the depth to each feature, corresponding 3-D points can be estimated. These correspondences are then used to estimate inter-frame transformations using a method such as least squares [55] or Iterative Closest Point [56]. Alternately, depth data may be used to generate 2-D scans, which can then be compared using scan matching techniques [57, 58] to estimate inter-frame transformations.

Some of the commonly used SLAM techniques assume sufficient information in the environment for correspondence based techniques to be successful. Indoor hallways, in which our system is intended to be used, do not provide consistent richness in texture or depth variations for either the visual odometry or scan matching techniques to generate consistently accurate estimates. To cope with this, the proposed system uses a combination of Manhattan rotation estimates [59, 60] with translation estimates from dead reckoning to generate a map of the robot's environment. To get Manhattan rotation estimates, lines are detected in a 2-D scan of the workspace and a dominant direction for these lines is inferred. This dominant direction is compared with a reference which is established in the map initialization frame. The Manhattan assumption is that lines in an indoor environment are orthogonal to each other. This property is used to estimate frame by frame rotation. Section 4.3 explains this mapping technique.

To satisfy the requirements for path planning, the classic navigation function method [61] is chosen for our system, the history of its development explained, and the research contributions relative to its modification are highlighted in the next section.

### 1.2.4 Navigation function path planning

In the work proposed here, the ‘predictive fields path planner’, an extension of navigation function path planning, is developed. Navigation functions, in turn, are a special type of potential fields path planner.

In a seminal article, Khatib [62] introduced potential fields path planning in robotics. The simple yet powerful idea which formed the basis of this paper was a topological representation of the robot workspace in which the robot was being attracted to its goal position and repelled by obstacles. Attraction and repulsion were both forces which were acting on the robot ‘virtually’, and the actual steering input to the robot to the goal was calculated simply as the net force acting on it at any given time. In effect, the workspace was pervaded with potential fields, such as the attractive well at the goal position and the high potentials at obstacle boundaries.

The potential field approach was adopted rapidly, and its variations used in other well known robot navigation methods such as the schema approach by Arkin [63] and the generalized potential field method of Krogh and Thorpe [64]. However, in 1991, Koren and Borenstein [65] provided a mathematical analysis of the weaknesses of the potential field method. In their work, they identified the following major problems with potential fields, paraphrased here from their paper:

- Local minima, where attractive and repulsive forces cancel out, exist.
- If obstacles are closely spaced, there is no path between them to goal.
- Robot oscillates close to obstacles and narrow passages between obstacles.

Despite this set of limitations, potential fields retain their appeal in robotics because of the speed and simplicity of their implementation. They have been used in subsequent robotics literature with some modifications, e.g. using a composite of various potentials to drive the robot [66] or defining potentials such that robot can converge to goal in the presence of nearby obstacles [67].

Using the idea of topological representation of the workspace to create navigation gradients for the robot, Rimon and Koditschek, in a series of papers [61, 68, 69, 70] introduced the idea of navigation functions. Navigation functions path planning is an integrated path planning, motion planning, and controls approach in which the following mathematical guarantees are shown to exist:

- Only a single global minimum exists at the goal position.
- Robot avoids collisions with obstacles.
- Robot stays within the boundary of the workspace.

In Section 2.1 details of the navigation function formulation have been provided. Because of their mathematical guarantees and the simplicity in their formulation, navigation functions were chosen as the path planning basis for our system. However, a number of modifications needed to be made to the framework to make it useful in real-world applications.

Since their introduction, navigation functions have been used in multi-agent robot simulations [71, 72] and in collision avoidance for articulated non-holonomic robots [73]. However, they have seen only limited experimental usage [74, 75] for two reasons:

- Highly variable magnitude of control inputs generated for the robot.
- Practical workspaces need to be transformed to circular workspaces before navigation functions can be used.

In Section 2.3, a normalized control input is developed and it is shown that this input yields a stable navigation system. In Section 2.4, a practical workspace representation is proposed. This representation obviates the need for estimating transformations to a circular world, which are typically difficult to find for practical geometries. A similar effort has been made by Filippidis and Kyriakopoulos [76], who extend the utility of navigation functions to curved, non-circular worlds, and who use normalized control inputs in [77].

With the mechanism for using navigation functions in practical environments in place, the need to incorporate obstacle motion into the path planning framework for a robotic person follower can be addressed. Navigation functions in their original form [61] were designed for use in static environments. However, it was shown mathematically by Chen et al. [72], and experimentally by Widyotriatmo and Hong [74] that the stability of this path planner is not affected by its use in dynamic obstacle environments. Hence, in our own previous work [78, 79], we used a modification of navigation functions called 'predictive fields path planning' to incorporate the motion of obstacles into the navigation function path planner. To do this, each obstacle with an ellipse which is representative of its direction of motion and velocity along that vector. Then, the repulsion felt by the robot from an obstacle was characterized by a function of the actual obstacle position and its predicted path inside its elliptical envelope. This formulation has echoes of the concept of 'danger' posed by an obstacle's motion, which has been used in the context of potential fields path planning [80, 81, 82, 83]. The elliptical field formulation and its simulation results are presented in Sections 2.2.1 and 2.2.4, respectively.

The elliptical field formulation was tested experimentally using a non-person following robot before it was integrated into the person follower system. This was a significant step in the development and prototyping of this path planner and, as mentioned earlier, one of the first demonstrable experimental results for navigation function path planning. The details of this experimental setup have been covered in

Chapter 3.

Finally, the predictive fields path planner was prototyped as a system module in the person follower in Section 4.4.3. In addition to the modifications to navigation functions described earlier, another modification was required for such a system, i.e. the ability to systematically cope with a moving target. This is because classic navigation functions assume a fixed goal position. The description of a workspace generation method which works around this limitation is given in Section 2.4.

In summary, a robotic person follower system was equipped with the ability to detect leader occlusions and overcome them using an indigenously developed path planner. The organization of the document is briefly reviewed in the next section.

## 1.3 Dissertation outline

In Chapter 2, the theoretical development of predictive fields path planning is motivated and explained. The assumptions and predicted performance are compared and contrasted with the original navigation functions path planning. Simulation results are provided to demonstrate the utility of this path planning framework.

In Chapter 3, the experimental results for predictive path planning tests with a non-person follower is detailed. Various modules of the system, including sensing, hardware and software interfacing, and navigation are explained.

In Chapter 4, the Kinect skeletal tracker, appearance descriptor for the leader, and mapping module which localizes the robot and feeds the path planner, are described. Proof of concept experimental results for the use of predictive fields path planning are provided.

Finally, in Chapter 5, results from the previous chapters are summarized and possible future directions for this research topic are discussed.

# Chapter 2

# Development of predictive fields path planning

The conceptualization and theoretical development of predictive fields path planning is presented in this chapter. Predictive fields build upon the seminal work of navigation function path planning by Rimon and Koditschek [61, 68, 69, 70]. Navigation functions, in turn, were influenced by the work of Khatib [62], in which the robot was guided to the goal position using a net driving force that was the vector sum of an attractive force to the goal and repulsive forces away from obstacles. Navigation functions are a compelling path planning solution because of the mathematical guarantee of convergence to goal. However, certain requirements and features of this method make it untenable for practical applications, including:

- Navigation functions are only proven to work for workspaces containing static obstacles.
- Navigation function path planners may generate impracticably large velocity inputs to the robot, created on account of a large scaling gain in the formulation.

- Navigation functions can be applied to real workspaces only after estimating a complicated geometric transformation called the star world transformation.

- Navigation functions can only be applied when the goal position is static.

In this chapter, methods to address each of the above limitations of the classic navigation function approach are presented [78, 79]. The term 'predictive fields', used to describe this modified navigation function method, alludes to the use of envelopes around moving obstacles to allow the robot to leverage obstacle motion information in the path planning paradigm. A stable, normalized velocity controller is proposed to obviate the need for the scaling gain and, in turn, for large input velocities. Finally, a new representation of workspaces circumvents the requirement to find complex star world transformations for workspaces. This representation has the added feature of being usable when the goal position for the robot is moving, a condition disallowed by the navigation function path planner.

This chapter begins with a review of the navigation function method and subsequent sections present the predictive fields approach and its results.

## 2.1 Navigation function path planning

The theory of navigation function path planning was proposed in a series of papers by Rimon and Koditschek [61, 68, 69, 70]. The eponymous 'navigation function' in this path planning method was a mathematical construct which pushed the robot to its goal position and away from obstacles. Certain information about the system was assumed to be available for path planning. The known information included:

- The position and size of the robot,

- The position and size of each obstacle,
- The location of the goal position for the robot, and
- The size of the workspace, assuming that the workspace at least encompassed the robot, goal, and all obstacles.

Assuming this information, the navigation function path planner was formulated to achieve the following objectives:

- **Objective 1**: The robot position was constrained to always lie within its workspace,
- **Objective 2**: The robot avoided collisions with all obstacles in the workspace, and
- **Objective 3**: The robot reached its goal position.

Given this setup, the authors proved that the navigation function, when constructed following a set of mathematical constraints, guaranteed convergence to the goal for any initial configuration.

### 2.1.1 The navigation function

The form of the navigation function was defined by Rimon and Koditschek [61, 68, 70] as follows. Let $q \in \mathbb{R}^{1\times 2}$ denote robot position. Let $q^* \in \mathbb{R}^{1\times 2}$ be the goal point in the interior of a robot free configuration space $F$. A map $\varphi : F \to [0, 1]$ is defined to be a navigation function if it is

- analytic on $F$,
- polar, with a unique minimum at $q^*$,

- admissible on $F$, and
- a Morse function.

Mathematically, a solution is proposed as

$$\varphi(q) = \frac{K_s \|q - q^*\|^2}{\left[\|q - q^*\|^{2k} + G(q)\right]^{1/k}}, \tag{2.1}$$

where $k \in \mathbb{N}$ is called the navigation gain, and $K_s \in \mathbb{R}$ is an unknown scaling factor between the dimensionless navigation function and units of the practical environment. The term $G \triangleq G_0 G_1 \in \mathbb{R}$ is a composite of workspace envelope avoidance ($G_0$) and obstacle avoidance ($G_1$) functions. The scalar functions $G_0, G_1 \in \mathbb{R}$ are defined as follows

$$\begin{aligned} G_0(q) &= \beta_0(q) \\ G_1(q) &= \prod_{i=1}^{n} \beta_i(q) \end{aligned} \tag{2.2}$$

where $\beta_0$ and $\beta_i$ are repulsion terms for workspace envelope and obstacles, respectively, and are discussed in subsequent sections. To converge to goal, the robot navigates along the gradient of the navigation function (2.1).

The destination of the robot, $q^*$, is assumed to be static and within the workspace. It has to be noted that the requirement of the goal position to be static makes it impossible to use this path planning approach for the motivating application, i.e. person following. For use in a practical situation, it is necessary to represent leader motion in such a way that the static goal requirement is not violated.

### 2.1.2 An overview of repulsion functions

Repulsion terms (2.2) of the navigation function (2.1) are designed to steer the robot away from the workspace envelope and other obstacles. They have been called 'obstacle functions' in literature [61]. Note that the workspace envelope itself is an 'obstacle' the robot must avoid, even though it may not have a physical presence in the environment. The terminology is changed here to 'repulsion function' to avoid confusing the workspace envelope with obstacles inside it. The envelope of the workspace is referred to as the 'workspace envelope' from here on, and 'obstacles' refers to the objects that lie inside the boundary, after the robot and its goal position are excluded from the list.

These functions need to follow the simple rule that their value is zero at the boundary of the obstacle and at the workspace envelope, i.e. when the robot touches either, and non-negative otherwise. This rule allows for repulsion functions to be formulated using different types of smooth curves. One of the research contributions of the predictive fields formulation is to identify the means by which repulsion functions for obstacles can be changed to account for the motion of these obstacles.

### 2.1.3 Repulsion function - workspace envelope

The formulation used for workspace envelope repulsion is derived from the work of Chen et al. [72, 84, 85]. If the robot is sufficiently distant from the workspace envelope, the boundary repulsion term does not contribute to the navigation function, i.e. $\beta_0(q) = 1$. When the robot of radius $r$ comes within a distance $r_s$ of the envelope, $r_s > r$, the repulsion term begins to contribute to the navigation function until, at the point of contact, this value reduces to 0 as per the requirements of repulsion functions. The transition of the function's value from 1 down to 0 is represented by

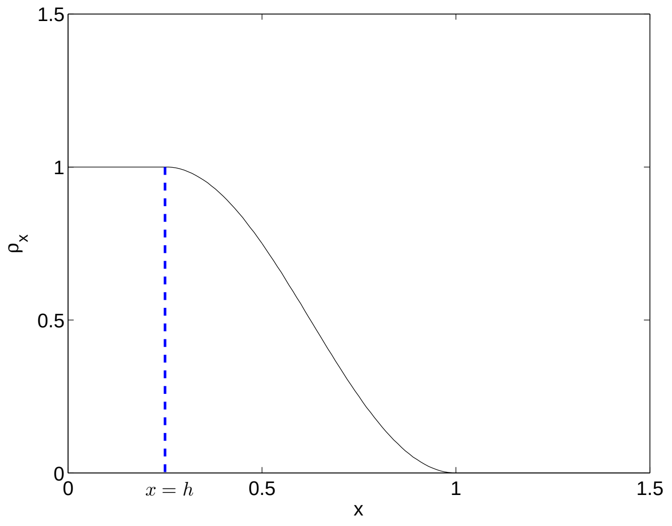

Figure 2.1: Bump function used for workspace envelope repulsion.

a smooth function called the bump function (Figure 2.1), first used in [86].

The workspace envelope repulsion function is thus represented as:

$$\beta_0(q) = \begin{cases} 1 & \text{if} \quad f(q) < h. \\ \frac{1}{2}\left[1 + \cos\left(\pi \frac{f(q)-h}{1-h}\right)\right] & \text{if} \quad h \leq f(q) < 1 \\ 0 & \text{if} \quad f(q) \geq 1 \end{cases} \tag{2.3}$$

The first condition implies that the robot has sensed the boundary but is not touching it, the second that the robot has touched the workspace envelope, and the final term indicates that the robot is far away from the workspace envelope. The function $f$ is defined as

$$f(q) = \frac{1}{r_{o0} - r} \left\| q - q_{o0} \right\|,$$

where $r$ is the radius of the robot, $r_{o0}$ is the radius of the workspace, and $q_{o0} \in \mathbb{R}^2$ is the center of the workspace. The parameter $h$ is defined as

$$h = \frac{r_{o0} - r_s}{r_{o0} - r},$$

where $r_s$ is the distance from the robot within which the repulsive term is activated. Since $r < r_s < r_{o0}$, $0 \leq h < 1$. This formulation describes the bump function curve seen in Figure 2.1.

### 2.1.4 Repulsion function - obstacles

It is assumed that the workspace contains all interior obstacles and the robot and goal positions. Past work on designing interior obstacle repulsion functions [61, 72] uses the quadratic form:

$$\beta_i = \left[ \|q - q_{oi}\|^2 - (r + r_{oi})^2 \right] \tag{2.4}$$

where $q_{oi} \in \mathbb{R}^+$ is the center and $r_{oi} \in \mathbb{R}^+$ the radius of the $i^{th}$ obstacle. When the robot and obstacle touch, the value of $\beta_i$ goes to zero as per the requirement of the beta function. As defined earlier, $r$ is the radius of the robot and $q$ is its position in the workspace.

The weaknesses of this formulation are discussed in Section 2.2 and an improved formulation is discussed in the same section.

### 2.1.5 Navigation inputs to robot

It is assumed [72] that the robot can be described by the following kinematic model

$$\dot{q} = u, \tag{2.5}$$

where $u \in \mathbb{R}^2$ is the control input to the robot, given by

$$u = -K \left( \frac{\partial \varphi}{\partial q} \right)^T, \tag{2.6}$$

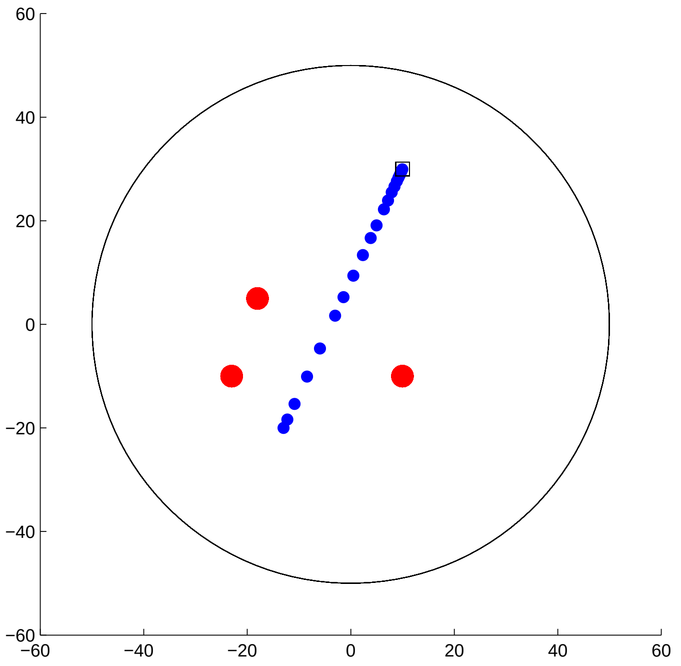

Figure 2.2: Path to goal using standard navigation functions.

The robot, marked using blue circles, approaches the goal, marked using a black square, in the presence of three stationary obstacles, marked using red circles. During this straight line traversal to goal, the robot stays within bounds of the workspace, marked using a black circular envelope.

Eq. (2.6) commands the robot to descend down the slope of the navigation function to its goal position. Though Rimon and Koditschek prove that this guarantees a global minimum exists at the goal which the robot will eventually reach, it requires accurate tuning of a few very sensitive parameters. Consider a relatively simple setup demonstrated in Figure 2.2 and tested using MATLAB Simulink. The robot has a clear path to goal (marked by the black square) in the presence of three obstacles (red circles), and it follows this path as indicated by the blue circles. However, this particular behavior could be observed only after the navigation gain $k$ (from (2.1)) was heuristically tuned to a value of $k = 20$, and the controller gain $K$ (from (2.6)) was tuned to the very large and quite unintuitive value of $K = 1.2 \exp 14$. Velocity inputs to the robot are seen in Figure 2.3, with the red lines representing $x$

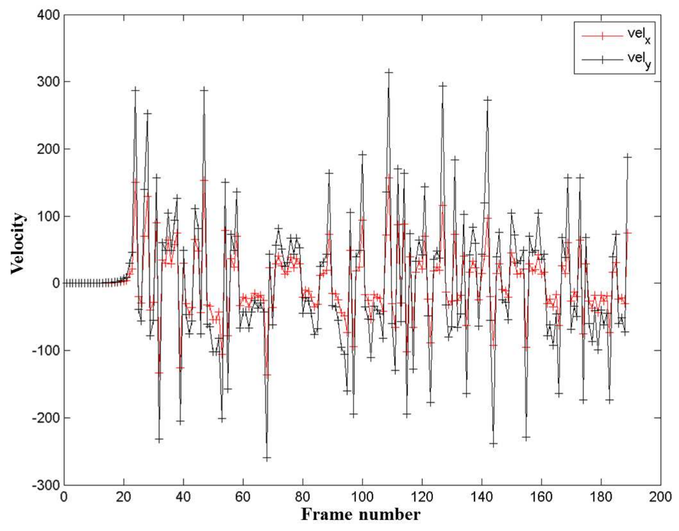

Figure 2.3: High velocity inputs to robot.

Using the standard form of navigation functions, the robot receives navigation inputs of unpredictable magnitude. Red lines show $x$ inputs and black lines show $y$ direction inputs.

velocity inputs and black lines representing $y$ velocity inputs. As seen for this trial, and typically observed in most trials, these values were found to be very high, in the hundreds or greater. Such inputs are not directly usable as an input to a practical mobile robotic platform during experiments. Finding the right combination of $k$ and $K$ was found to be a time consuming process with no real payoff at the end in terms of getting a usable velocity control input for the mobile robot. Hence, an improved control input was desirable for this form of the navigation function path planner. Such an input is proposed in Section 2.3.

### 2.1.6 Star world transformation

For the original Rimon-Koditschek formulation to be usable in a practical workspace, the workspace has to satisfy the definition of a 'star world'. A workspace is defined to be a star world if it contains a point called a 'center point' in [61]. Rays

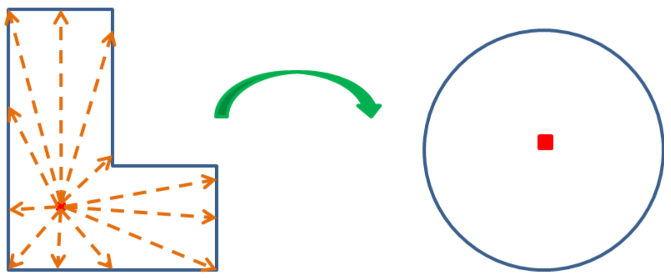

Figure 2.4: Transformation from a star world to a circular world.

The "star world" shape to the left contains a center point which is marked by the red dot. Orange dotted lines indicate that rays emanating from the center point intersect the workspace envelope only once. To use navigation functions for this workspace, a transformation to the circular workspace to the right needs to be estimated.

drawn to all points on the boundary of the workspace from the center point must intersect the boundary once and only once (Figure 2.4). If the workspace is shown to have such a center point within it, then it can be transformed to a circular world. Navigation functions can only be used in worlds which are circular and which contain circular objects.

The problem with using star world transformations is that they mandate two features for any practical workspace before they can be used in navigation function path planning:

- The workspace has to be a star world, i.e. there has to be a certainty that a center point exists. This cannot be guaranteed for all practical workspaces.
- The transformation requires an implicit shape representation for the star world. Such a parametric representation of the practical workspace may not be available during an experimental trial.

In Section 2.4, a practical workspace representation is proposed such that the need for computing this potentially complicated transform is removed.

This concludes a summary and critique of the advantages and limitations of the classic navigation function path planner. In subsequent sections, various modifications to navigation function path planning are proposed. These modifications address the limitations of the approach outlined in the chapter introduction and in this section.

## 2.2 Development of an elliptical repulsion function

The first of the limitations of navigation function path planners is that obstacle motion is not encoded in them in any manner. In its original form, obstacle repulsion is defined by Eq. (2.4). The original definition of $\beta_i$ satisfies the requirements of the repulsion function from Section 2.1.2 and has the favorable property that beta changes quadratically as the robot moves toward the obstacle. This rate of change ensures that the robot's approach to an obstacle's current position is strongly repelled. However, this definition does not account for the manner in which an obstacle has been moving or is expected to move. It does not convey the level of threat posed by an obstacle to the robot's approach to the goal. For example, even if the current position of the obstacle is not between the robot and the goal, is there a chance that the obstacle will move in between the robot and target at a later instant, when the robot has moved dangerously close to the obstacle? A solution to this is to represent the obstacle motion using an elliptical field. This concept was first introduced our work [79], and has since been subject to rigorous mathematical treatment by Filippidis and Kyriakopoulos [76], in which it was shown that the entire elliptical envelope can be used to compute navigation function terms.

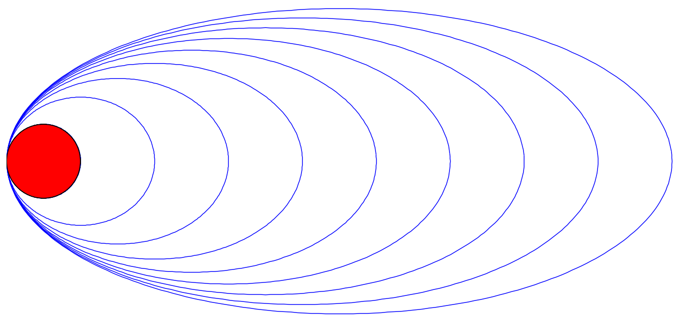

Figure 2.5: Transition from circular to elliptical field.

The red circle represents the obstacle's physical envelope. Various blue ellipses around it demonstrate the model used to encapsulate the obstacle's predicted motion direction and velocity.

## 2.2.1 Using an ellipse to create a predictive field

The original beta function for obstacles in (2.4) is modified to incorporate information about the motion and expected future state of an obstacle. As demonstrated in Section 2.2.4, this new formulation makes the robot more responsive to the threat posed by the motion of an obstacle, and it skews the gradient of the navigation function in such a way that the region in which the obstacle may be expected to appear is avoided by the robot. To begin the discussion, consider a general ellipse equation:

$$\frac{\left[(x-h_e)\cos(\theta)+(y-k_e)\sin(\theta)\right]^2}{a^2}+\frac{\left[-(x-h_e)\sin(\theta)+(y-k_e)\cos(\theta)\right]^2}{b^2}=1 \quad (2.7)$$

centered at $(h_e, k_e)$ and fully containing the obstacle. $\theta$ is the angle of the ellipse major axis with respect to the $x$ axis. $a$ and $b$ are lengths of the semi-major axis and semi-minor axis respectively.

Then the obstacle's motion is captured using the ellipse from Eq. (2.7). This ellipse is defined to the 'predictive field' of the obstacle, with the lengths of the major axis $2a$ and the minor axis $2b$ of the ellipse representing one aspect of obstacle motion information each. When the obstacle is either known to be stationary or nothing is known about its motion, the ellipse collapses into a circle the size of the obstacle to indicate no motion information. As we learn (based on estimates from the vision system) the motion of the obstacle, the circle is skewed in the direction of motion. Therefore, the direction of the major axis indicates the estimated direction of motion, and the length of the major axis indicates the estimated speed. The length of the minor axis then indicates the uncertainty in the direction estimate. Thus, various scenarios are captured by the construction of this elliptical field, enabling it to explain the influence of predictive fields in potential field based path planning. Typical evolution of the elliptical field is illustrated in Figure 2.5.

It is assumed that sensors and algorithms working in parallel with the path planner can track objects, quantify their behavior, and uses this data to provide suitable values of $a$ and $b$ to guide the path planner. In case the sensing system is not sufficiently sophisticated to provide these values, a fixed-size ellipse could also be used on the basis of motion history.

### 2.2.2 Constraints on the size of the ellipse

The elliptical predictive field is an estimate of where we expect the obstacle to be at a future time instant. This estimate should obviously contain the current position of the obstacle, so its radius should not extend outside the perimeter of the ellipse. If the obstacle of radius $r_o$ is placed at the focus of the ellipse, then this means that the radius of the obstacle should be less than the periapsis (the smallest radial distance) of the ellipse:

$$r_o \leq a - \sqrt{a^2 - b^2}, \tag{2.8}$$

which rearranging terms yields a constraint on the length of the minor axis:

$$b \geq \sqrt{r_o\,(2a - r_o)}.$$

The limiting case of (2.8) is when the ellipse is a circle, i.e., $a = b$. This leads to the following constraint on the length of the major axis:

$$a \geq r_o.$$

### 2.2.3 Formulation of repulsion function

Now that the elliptical field has been defined to capture motion trends of an object, the repulsive term in (2.4) needs a redefinition to leverage this information. It needs to be noted that the ellipse is a *likely* region for the presence of the obstacle, and the robot is allowed to be inside the ellipse as long as the robot does not touch the measured position of the obstacle. The requirement that $\beta_i$ should go to zero on physical contact between the robot and obstacle still needs to be obeyed, and the robot should be repelled from the obstacle at any other position in the workspace, whether inside or outside the ellipse.

In addition to the above observations, the following requirements are introduced for beta redefinition:

- The elliptical predictive field should provide the obstacle's repulsive force when the robot is outside the ellipse.
- The circular formulation from Eq. (2.4) should come into play only when the robot is inside the ellipse.

A modified beta function is proposed as follows:

$$\beta_i = \begin{cases} 0 & \text{robot touches the boundary of an obstacle} \\ \beta_{c_i} & \text{robot is inside the ellipse} \\ \beta_{e_i} & \text{robot is outside the ellipse} \end{cases} \tag{2.9}$$

where $\beta_{e_i}$ is the beta function for the robot with respect to the ellipse around the $i^{th}$ obstacle. The obstacle is located at one focus of the ellipse defined in Eq. (2.7). Let this position be $q_{o_i}$. The obstacle is expected to move along the major axis in the direction of motion to arrive at its predicted position $q'_{o_i}$ at a future time instant $t'$.

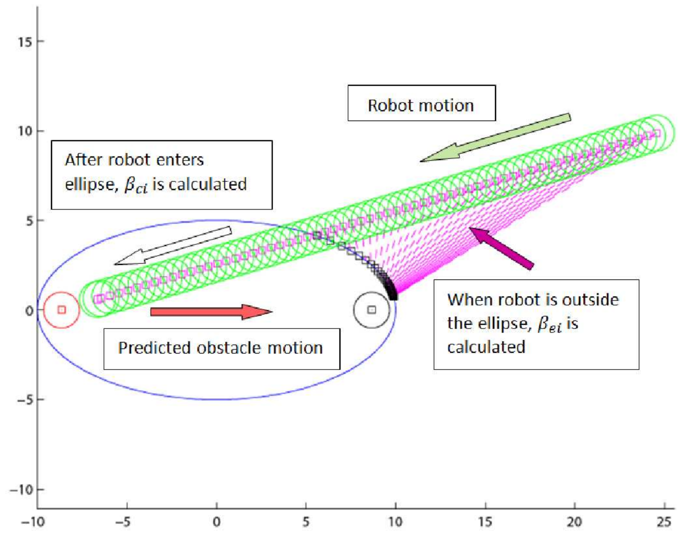

Figure 2.6: A sample robot approach to obstacle ellipse.

Overlapping green circles indicate a sample approach path of the robot. The obstacle position (red circle) is projected along the major axis of the ellipse to its predicted position (black circle). When outside the ellipse, the black circle is used for computing obstacle repulsion term. When the robot enters the uncertain elliptical field, the actual position of the obstacle is used to compute obstacle repulsion.

Then $\beta_{e_i}$ is defined as

$$\beta_{e_i}(q) = \left\| q - q'_{o_i} \right\|^2 - (r + d_{e_i})^2 + \delta, \tag{2.10}$$

where $d_{e_i}$ is the distance from the predicted obstacle position $q'_{o_i}$ to the point $q_{re_i}$ where the line joining the robot position $q$ and the predicted position of the obstacle $q'_{o_i}$ intersects the ellipse. Various positions of the robot (indicated by the green intersecting circles) as it approaches the obstacle along a straight line are plotted in Figure 2.6. The left focus of the ellipse (red) is the actual obstacle position, the right focus (black) is the most likely predicted position. Points of intersection with the ellipse are calculated and the point closer to the robot is selected for $\beta_e$ computation.

Note that if we set $\delta = 0$, this formula for $\beta_{e_i}$ guarantees that it goes to zero when the robot touches the outside of the ellipse. The curve described by this formula (with a nonzero $\delta$) can be seen in Figure 2.7. We will see later how to define $\delta$.

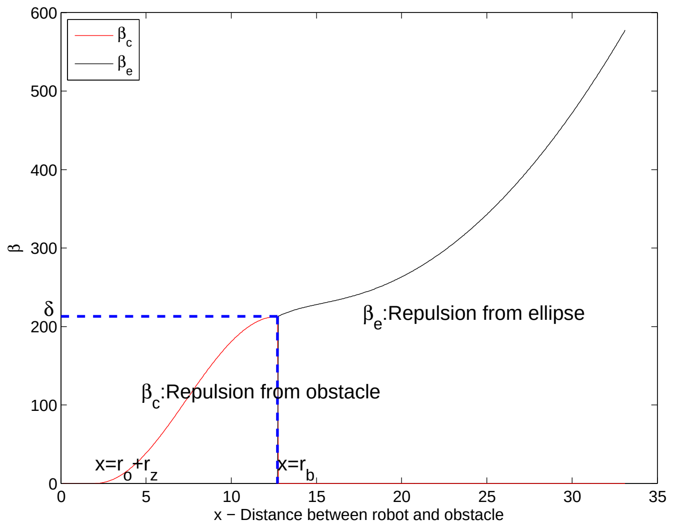

Figure 2.7: Repulsion term v. robot distance from obstacle ellipse.

The requirement for the overall beta $\beta_i$ is that it should be defined up to the point of contact with the obstacle. To satisfy this, the constant $\delta$ allows $\beta_{e_i}$ to reduce to a non-zero minimum at the point where the robot touches the ellipse. This constant is also the value of $\beta_{c_i}$ at the point where the robot touches the ellipse. As the robot continues to move into the ellipse toward the target, $\beta_{c_i}$ reduces to zero as desired. The $\beta_{c_i}$ curve should be continuous with respect to the $\beta_{e_i}$ curve to make the resultant beta differentiable throughout its domain. This curve is plotted in Figure 2.7.

The requirements of the function $\beta_{c_i}$ are:

- The function should reach its maximum value at the boundary of the ellipse, i.e., when $\left\| q - q'_{o_i} \right\| = (r + d_{e_i})$.
- The function should reach its minimum value of zero when the robot and the obstacle touch, i.e., when $\| q - q_{o_i} \| = (r + r_{o_i})$.
- The maximum value of the function should be given by the $\beta_{c_i}$ value when the robot touches the ellipse along a straight line approach to the obstacle. Let this point be $q_{re_i}$. This gives $\delta$ a constant value relative to the line of approach $\delta = \| q_{re_i} - q_{o_i} \|^2 + (r + r_{o_i})^2$. This constant value is added to the ellipse beta when the robot is outside the ellipse, and accounts for the movement of the robot inside the elliptical predictive field.
- Additionally, the addition of delta to $\beta_{e_i}$ ensures that the obstacle beta constraint, i.e., beta goes to zero only when the robot and obstacle physically touch, is satisfied even with the addition of the ellipse to the formulation.

This is accomplished by using a mirror image of the bump function [86], since the highest point on the curve needs to be further away from the x axis.

Given the above constraints, let the following terms be defined:

$$\begin{aligned} r_b &= \| q_{re_i} - q_{o_i} \| - (r_{o_i} + r) \\ h_c &= r_{o_i} + r \\ \delta &= \| q_{re_i} - q_{o_i} \|^2 - (r + r_{o_i})^2 , \end{aligned}$$

where:

- $r_b$ - range of the bump function, or the $x$ coordinate where it attains its maximum
- $h_c$ - zero point of the bump function relative to distance of the robot from obstacle
- $\delta$ - maximum value of the bump function, added to the ellipse beta

An additional point has to be made about $q_{re_i}$. Outside the ellipse, the point of intersection of the robot and the ellipse, of the two possible points of intersection, is the one closer to the robot. To calculate the bump function value inside the ellipse, the definition of the point of intersection needs a slight change. As the robot moves closer and closer to the obstacle, it is possible that the point of intersection on the other side of the obstacle is the nearer point of intersection of the robot path with the ellipse. Retaining the 'nearest intersection point' definition will then change $\delta$ for the bump function and the desired shape of the $\beta$ curve will be lost. To ensure this does not happen, the unit vector from the obstacle to the robot, $\bar{n}_{re_i}$, is used. The point of intersection is then defined as the one which is along the vector $\bar{n}_{re_i}$.

The bump function is then defined as:

$$\beta_{c_i}(x) = \begin{cases} 1 & r_b \leq x \\ 0 & 0 \leq x < h_c \\ \frac{\delta}{2}\left[1 - cos\left(\pi\frac{x-h_c}{r_b-h_c}\right)\right] & h_c \leq x < r_b \end{cases} \tag{2.11}$$

The bump function then gets the following values. At $x = h_c$, the obstacle and robot touch and $\beta_{c_i}$ goes to zero. At $x = r_b$, the elliptical predictive field and the robot touch and $\beta_{c_i}$ gets its maximum value of $\delta$. Beyond $r_b$, the maximum value of the

$\beta_{c_i}$ term, $\delta$, adds to the $\beta_{e_i}$ term which begins to dominate the overall $\beta$ function. Therefore the value of $\beta_{e_i}$ approaches $\delta$ instead of 0 as the robot moves towards the ellipse.

With these definitions for $\beta_{c_i}$ and $\beta_{e_i}$, the overall definition of $\beta_i$ (2.9) is consistent with the requirements of the repulsion function. In the next section, the qualitative effect of this redefinition of the repulsive term on robot navigation can be seen.

### 2.2.4 Effect of new repulsion function on robot path

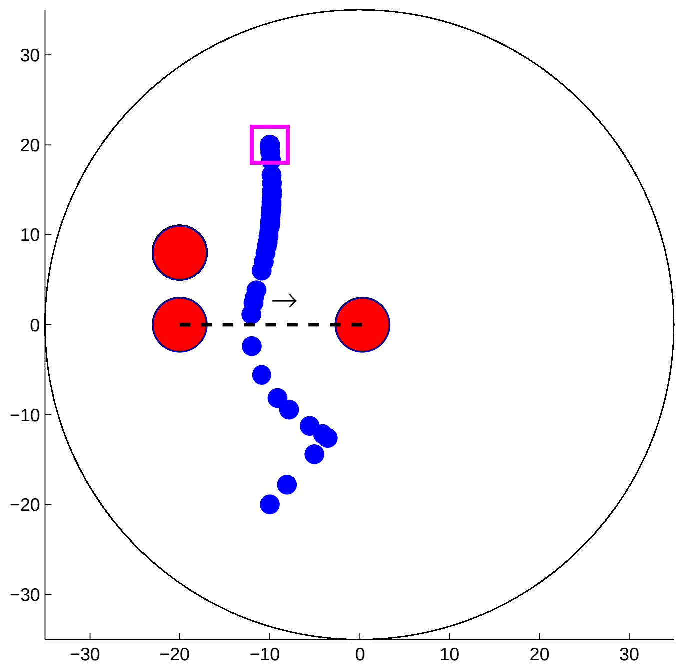

Figure 2.8: The path of the robot without predictive information.

The robot path, indicated by blue circles, approaches the obstacle path, indicated by a black dotted line, in the absence of predictive field information. The moving obstacle moves left to right, from the left end of the black dotted line, to the right, and its start and end positions are both shown by red circles. A stationary obstacle, shown by a red circle, sits at $(-20, 8)$ throughout the simulation.

MATLAB Simulink (Mathworks Inc., Natick, MA) was used to simulate the proposed change to the repulsion function and to qualitatively compare it against previous results from Chen et al. ([72, 84, 85]). Such a comparison is easily possible because the predictive field reduces to the obstacle's circular envelope when motion information is not used, and Eq. (2.10) reduces to Eq. (2.4). The hypothesis to be tested is: using predictive fields makes it possible for the robot to converge to the target following more effectively than using the original navigation function formulation from Rimon and Koditschek. This also implies that the robot is pushed away from the predicted path of the obstacle, thus driving it to goal using a less dangerous

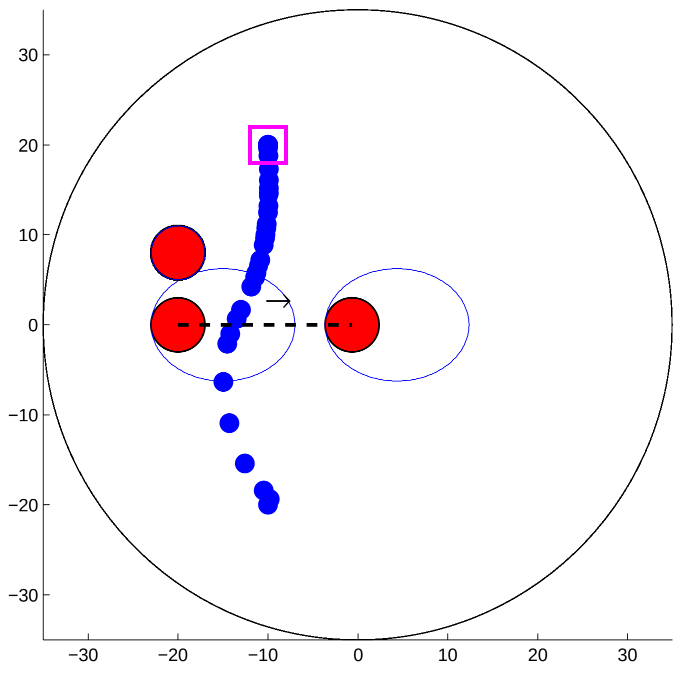

Figure 2.9: The path of the robot with predictive information.

The setup of this figure is exactly the same as Figure 2.8. The robot path, indicated by blue circles, moves away from the obstacle path, indicated by a black dotted line, when predictive field information is used. Elliptical field of the moving obstacle is indicated by the blue envelope around the red circle representing it.

route. This notion of ‘danger’ of collision with obstacles has also been explored in the context of potential fields path planning [82, 81, 80].

Results are demonstrated using two hypothetical scenarios:

1. An obstacle initially obstructs the straight line path from robot to goal, but it begins to move out of the way as the simulation progresses.

2. An obstacle is initially at a distance from the straight line trajectory from robot to goal, but it moves to obstruct the path as the simulation progresses.

Both cases are tested with and without the predictive predictive field surrounding the obstacle. The setup of the workspace is described as follows:

- Robot has a radius of $r = 1$ and is initially located at $(-10, -20)$.

- The workspace envelope bump function comes into effect at a distance $r_s = 5$.
- Goal is located at $(-10, 20)$.
- Stationary obstacle with radius $r_{o1} = 3$ is located at $(-20, 8)$. The stationary nature of the obstacle causes the predictive predictive field around it to shrink to a circle with the same radius as the obstacle.
- The workspace is centered at $(0, 0)$ with a radius of $r_{o0} = 35$.
- The predictive field of the moving obstacle of radius $r_{o2} = 3$ is described by an ellipse with parameter $a = 8$ in both cases.
- Gains from Eq. (2.1) and Eq. (2.6) are set at $\kappa = 4.5$ and $K = 1.2$ respectively. They remain unchanged for the given setup; however, they might need to be tuned on changing the number of obstacles in the workspace.

In Scenario 1, the obstacle starts at $(-20, 0)$ and travels 20 units in the workspace at a constant velocity. The sense of its motion is such that it is moving out of the way of the robot's path to goal. Without the use of a predictive field, it can be seen that, in Fig. 2.8, the robot tries to move around the obstacle. This causes it to move toward the path of the obstacle and forces a correction in its path approximately midway through its trajectory. However, when the predictive field is added, the path planner is able to sense that the more optimal path to goal would actually be behind the obstacle, as seen in Fig. 2.9. The trajectory traced as a result is much more intuitive than the first case.

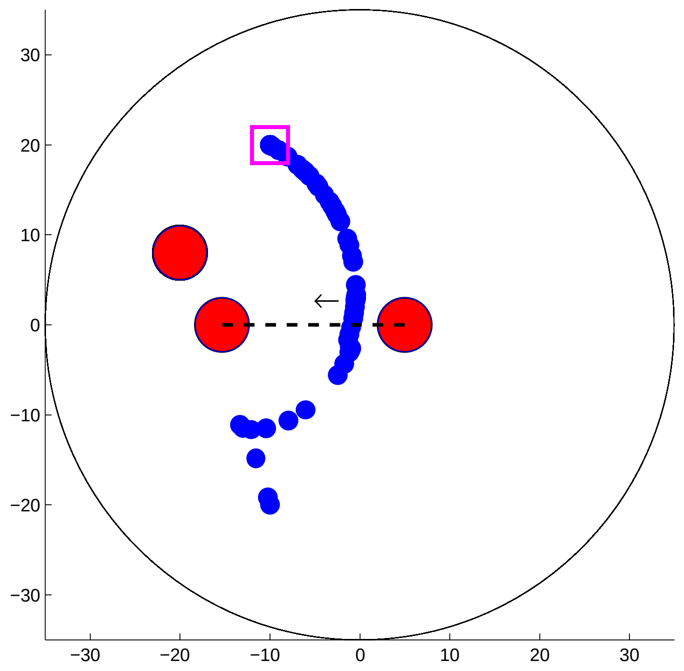

Figure 2.10: The path of the robot without predictive information.

The robot path, indicated by blue circles, approaches the obstacle path, indicated by a black dotted line, in the absence of predictive field information. The moving obstacle moves right to left, moving in the way of the straight line path of the robot to goal. Its start and end positions are both shown by red circles and direction of motion by the little black arrow. A stationary obstacle, shown by a red circle, sits at $(-20, 8)$ throughout the simulation.

A similar improvement is observed in Scenario 2, when the obstacle starts out of the way of the robot's path to goal. Once again, it moves 20 units with a constant velocity, but this time it moves from right to left. Its motion is such that, relative to the robot, the robot's straight line path to goal is obstructed. It is seen that the robot, when guided by current information alone (Fig. 2.10, initially travels toward the obstacle, until the repulsion from the obstacle forces a change in its trajectory. This course correction is averted using predictive fields (in Fig. 2.11), where the robot's path is always such that it seeks to avoid the path of the obstacle.

Results from multiple trials corroborated the hypothesis that the robot was able to successfully converge to the goal while moving along a less dangerous trajec-

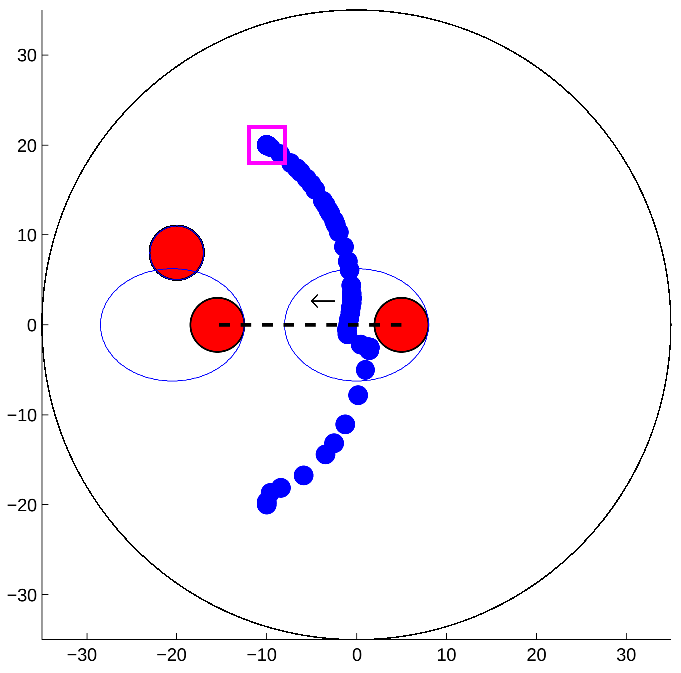

Figure 2.11: The path of the robot with predictive information.

The setup of this figure is exactly the same as Figure 2.10. The robot path, indicated by blue circles, moves away from the obstacle path, indicated by a black dotted line, in the presence of predictive field information. The elliptical obstacle envelope is indicated by a blue ellipse around the obstacle position.

tory to goal when predictive fields were defined for obstacles in the workspace. A quantitative metric for evaluating the performance of predictive fields is propsed in the next section.

### 2.2.5 Risk score - a metric for predictive fields evaluation

As discussed in the previous section, the advantage of predictive fields is the ability to steer the robot away from a hazardous path, i.e. a path which is on a collision course with an obstacle. For example, in Figure 2.12, see that the robot moves in front of the obstacle in the simulation plot on the left. In the absence of predictive fields, the navigation function path actually takes the robot in front of and around the moving obstacle. The risk in this is evident: should there be

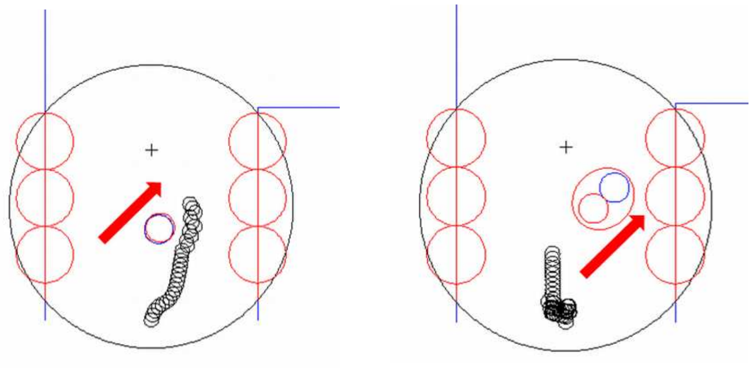

Figure 2.12: Route in absence and presence of predictive fields.

In both images, overlapping black circles are robot positions from the start to the time instant at which this snapshot is taken. The plus sign at the top is the robot goal position inside the workspace envelope marked by a large black circle. Red wall obstacles at the left and right borders of the workspace envelop the red wall lines. Obstacle is indicated by red and blue circles, red being the actual position of the obstacle, and blue its projected position. The large red arrow shows the direction of obstacle motion. Clearly, the presence of the ellipse in the image to the right steers the robot away from a hazardous path en route to goal.

any unexpected change in the velocity of the moving obstacle, the robot may not be able to react quickly enough to avoid a collision. Clearly, in a human-populated environment, this is harmful behavior which poses an unacceptable risk. Contrary to the non-predictive field case, the simulation trial in which the obstacle motion ellipse is used (image on the right of Figure 2.12) shows the robot avoiding the projected obstacle path entirely.

Though repeated trials provide strong empirical evidence for the improved 'low risk' behavior of the predictive fields path planner, a quantitative metric is desired to support such observations. A simple metric called the 'risk score' is proposed. This is proposed to be a measure of the risk posed by the planned path for a particular scenario. The risk score is meant to be a comparative benchmark. Comparing this score for a single trial should indicate whether the predictive fields or standard navigation function path planner steered the robot along a path of less danger in terms of obstacle motion.

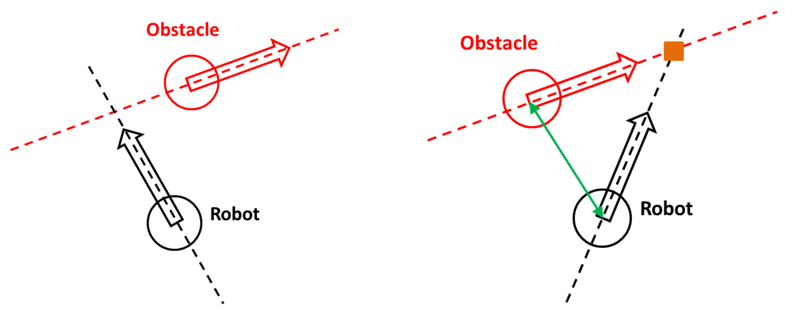

Figure 2.13: Calculation basis for the risk score.

When the obstacle (red circle and arrow) is moving away from the robot (black circle and arrow), there is no 'hazard' in the relative motion. When the paths are projected to intersect, as shown in the image to the right using an orange marker, the hazard score for this instant is inversely proportional to the distance between the robot and the obstacle, indicated using a green arrow.

The risk score is calculated using the following specifications. For any given instant in a trial, the risk score should be:

- Zero, when robot and obstacle are moving in non-converging directions.
- Low, when robot and obstacle are converging but are separated by a large distance.
- High, when robot and obstacle are converging but are separated by a small distance.

The case for a zero risk score is represented by the image on the left in Figure 2.13. The direction vectors of the robot and obstacle are such that the lines represented by these vectors intersect away from the direction of motion of the obstacle. A similar 'zero risk score' case exists when the lines intersect away from the robot's direction of motion. Thus, if the $i^{th}$ frame satisfies either condition, the risk score for this frame is given by $h_i = 0$.

The case for a non-zero score is represented by the image on the right in Figure 2.13. The vector lines intersect at a point along the motion directions of both the obstacle and the robot. If the robot and obstacle are separated by a distance $d_i^{ro}$, then the hazard score for this frame is given by

$$h_i = m \cdot \frac{1}{d_i^{ro}}, \tag{2.12}$$

where $m$ is an arbitrary positive scaling factor. Using the reciprocal of the distance satisfies the second and third specifications for the risk score. The total risk score for a trial is given by $H = \sum_i h_i$, i.e. the sum of individual hazard scores over all frames.

The performance of the risk metric is tabulated in Table 2.1. Six representative scenarios with one moving obstacle each were chosen. The image in the second column of the table shows the scenario for which data is being tabulated in the succeeding columns. In each scenario, the robot starts at the bottom of the workspace and approaches a goal position at the top. The start and end point are the same for each scenario. The arbitrary scaling factor from Eqn. 2.12 is chosen to be $m = 100$. Total time taken for each simulation for each case (ellipse/non-ellipse) is also given in the table. It can be seen that in most cases, the use of the ellipse reduces the time taken to converge to goal, although there isn't a marked difference in the time taken, and there are exceptions such as Scenario 3.

| No. | Scenario | No ellipse risk score | Time (sec) | Ellipse risk score | Time (sec) |
|---|---|---|---|---|---|
| 1 | 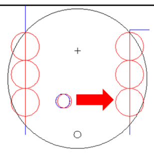 | 210.73 | 17.50 | 63.94 | 13.30 |
| 2 | 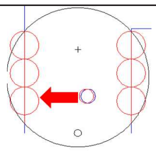 | 66.55 | 14.00 | 0 | 12.25 |
| 3 | 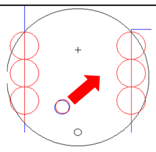 | 819.74 | 14.00 | 248.35 | 20.65 |
| 4 | 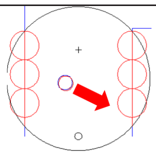 | 115.00 | 24.15 | 96.02 | 18.90 |
| 5 | 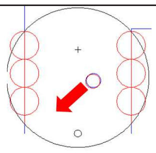 | 139.1 | 24.50 | 72.14 | 23.80 |
| 6 | 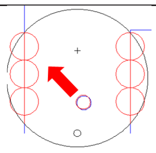 | 103.45 | 20.30 | 70.38 | 14.70 |

Table 2.1: Risk score for different scenarios.

Six representative scenarios of robot and obstacle motion. The score, in each scenario, is lower for the ellipse case than the non-ellipse case. In all except one scenario, the robot, shown by the small black circle at the bottom of the workspace, converges to goal, shown by the plus sign, faster when the ellipse is used.

As can be seen in Table 2.1, the ellipse case outperforms the no-ellipse case in each scenario. Risk scores are lower for each ellipse case compared to the non-ellipse case. This substantiates the hypothesis that a quantitative risk metric reflects the qualitative observation that predictive fields are better suited for use with moving obstacles.

Results shown here are for a single moving obstacle. For multiple obstacles, scores relative to each obstacle can be combined for each instant in the trial and the total risk score is calculated as the sum of all such scores.

## 2.3 Development of directional control input

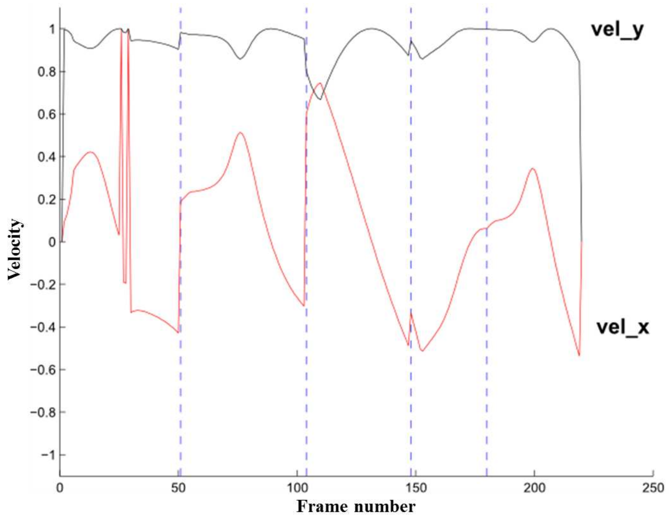

Figure 2.14: Individual components of the unit velocity vector.

Using the directional control input, both $x$ velocity and $y$ velocity inputs, shown using red and black lines respectively, are always between $-1$ and 1. Their values from a trial are shown in the figure.

The controller introduced here differs from previous navigation function controllers [61, 72]. These controllers required the use of an arbitrarily high scale factor

$K_s$ in Eq. 2.6) to drive the robot to goal. The resultant system was found to be extremely gain-sensitive and it was difficult to empirically estimate the scaling required for the robot to be successfully driven to goal for a particular configuration. Thus, a modification is made to the control input, driving the robot using the direction of the navigation gradient rather than the gradient itself. The control input to drive the robot to $q^*$ is:

$$\dot{q} = u. \tag{2.13}$$

where $u$ is modified to be

$$u = -K \frac{\left(\frac{\partial \varphi}{\partial q}\right)^T}{\left\| \frac{\partial \varphi}{\partial q} \right\| + \epsilon}$$

$K \in \mathbb{R}^{2\times 2}$ is a matrix of positive gain values and $\epsilon$ is a small positive constant. Components of the unit control input vector are seen in Figure 2.14. A similar, normalized control input was also used by Filippidis and Kyriakopoulos [77], citing the high value of the navigation gain $k$ as a motivating factor.

### 2.3.1 Stability Analysis

Consider a Lyapunov candidate function, same as the one used by Chen et al. [72],

$$V(q) = \varphi(q). \tag{2.14}$$

First differentiating (2.14) with respect to time and then substituting the right hand side of the control equation yields

$$\begin{aligned} \dot{V} &= \tfrac{\partial \varphi}{\partial q} \cdot \dot{q} \\ &= -\tfrac{\partial \varphi}{\partial q} \cdot K \cdot \frac{\left(\frac{\partial \varphi}{\partial q}\right)^T}{\left\| \frac{\partial \varphi}{\partial q} \right\| + \epsilon} \\ &= -f(t) \end{aligned}$$

where $f(t)$ denotes a non-negative function as follows

$$\begin{aligned} f(t) &= \begin{bmatrix} \frac{\partial\varphi}{\partial x} & \frac{\partial\varphi}{\partial y} \end{bmatrix} \begin{bmatrix} K_x & 0 \\ 0 & K_y \end{bmatrix} \begin{bmatrix} \frac{\partial\varphi/\partial x}{\|\frac{\partial\varphi}{\partial q}\|+\epsilon} \\ \frac{\partial\varphi/\partial y}{\|\frac{\partial\varphi}{\partial q}\|+\epsilon} \end{bmatrix} \\ &= \frac{1}{\|\frac{\partial\varphi}{\partial q}\|+\epsilon} K_x \left(\frac{\partial\varphi}{\partial x}\right)^2 + \frac{1}{\|\frac{\partial\varphi}{\partial q}\|+\epsilon} K_y \left(\frac{\partial\varphi}{\partial y}\right)^2 \end{aligned}$$

Each of the terms in $f(t)$ is positive. So it can be concluded that

$$\dot{V} \leq 0. \tag{2.15}$$

Therefore $V(q)$ is non-increasing. To establish convergence, the corollary of Barbalat's Lemma is invoked from [87] (Lemma 4.3) which states that:

- If $V(t)$ is a non-negative function of time on $[0, \infty)$,
- If $\dot{V}(t) \leq -f(t)$, $f(t)$ being non-negative,
- If $\dot{f}(t) \in L_\infty$

then

$$\lim_{t\to\infty} f(t) = 0. \tag{2.16}$$

It is clear that the first condition is satisfied by the basic requirement of the navigation function as a mapping onto $[0, 1]$, and the second by the proof for $f(t)$ being non-negative. For the third, consider that the navigation function is analytic on the free configuration space, which establishes that $\frac{\partial\varphi}{\partial q}, \frac{\partial^2\varphi}{\partial q^2} \in L_\infty$. Thus $\dot{f}(t) \in L_\infty$ is satisfied, and the lemma can be applied.

From the lemma and from the equation for $f(t)$, $\left\|\frac{\partial\varphi}{\partial q}\right\| \to \infty$ as $t \to 0$. The properties of the navigation function imply that $\frac{\partial\varphi}{\partial q} \to 0$ only at the goal configuration $q^*$.

Hence it is proven that

$$q(t) \to q^* \tag{2.17}$$

within a specific workspace.

The control input described in this section uses the gradient of the navigation function. The gradient vector is normalized to unit magnitude, but its $x$ and $y$ components vary according to the direction of the gradient. This unit-length directional vector is multiplied by the gain $K$ to create a constant magnitude, velocity control, input to the robot. The control input described here thus solves the problem of high velocity inputs while demonstrably resulting in convergence to goal.

## 2.4 Development of workspace generation method

For practical use of predictive fields, two limitations of the original navigation function method have yet to be addressed:

- Navigation functions only work in circular or star worlds.
- Navigation functions are incompatible with moving goal positions.

These two points are addressed in this section. For our proposed method of workspace generation, the following reasonable assumptions are made:

- The robot's sensing range is limited,
- The sensor (e.g. Microsoft Kinect) gathers all information necessary to implement a predictive fields path planner, and
- The person to be followed is generally within the sensing range of the robot.

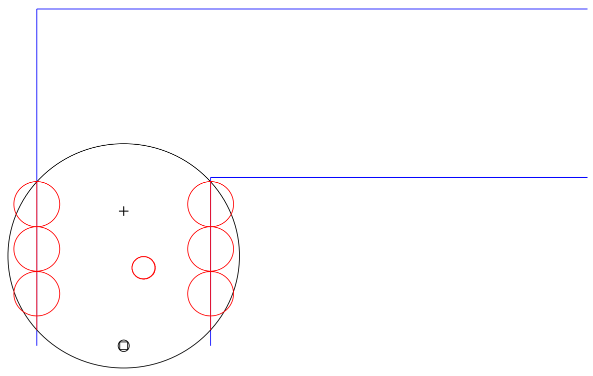

Figure 2.15: Generation of workspace compatible with navigation functions.

A long, L-shaped hallway is divided into multiple workspaces. Each workspace envelope is shown by the large black circle. Wall lines, in red, are encapsulated using larger circular, red wall obstacles. The lone internal obstacle in this example is shown using a small red circle. The robot, shown using a small black circle, starts from the bottom of the workspace and converges to the goal for that workspace, shown using the plus sign.

### 2.4.1 Workspace representation

Each of the two geometries required for navigation functions, i.e. truly circular world or start transformed world, is prohibitive for different reasons. Practical indoor workspaces do not resemble circular worlds, and finding a mapping from a practical workspace (star-world) to a circular world is non-trivial. These constraints compel exploring a third option, in which a practical workspace is represented as a circular world without the complications of a star world transformation. A simplified representation of a practical workspace makes it possible to use predictive fields in real-world scenarios.

The work by Tanner et al. [73] includes a 'union of ellipsoids' approach, which is one such attempt at simplified representation. In their work, the non-spherical robot and obstacles are represented as a combination of smaller ellipsoids, following which the entire system of ellipsoids is transformed to point obstacles on which the Rimon-Koditschek formulation is designed to operate. The basis of the idea, i.e.

decomposing an object as a union of circular envelopes where necessary, is used here, without the subsequent deformative transformations to point bodies.

To begin this representation, the workspace envelope for the navigation function is defined using the limited sensing range of the robot. The area of the hallway visible to the robot is enveloped by a circular workspace. Segments of the wall which intersect this sensing envelope are computed. The wall is an obstacle the robot needs to avoid, hence it is represented as a union of non-overlapping circular obstacles generated using wall segments from the previous step. The robot and each of the stationary and moving obstacles are also encompassed by circular envelopes, thus defining non-wall obstacles for the generated workspace. With this, the workspace has been defined such that it is fully compatible with the requirements of navigation functions. All the components of the workspace, inclusing the workspace itself, are encompassed by circular envelopes. The generated workspace is shown in Fig. 2.15.

### 2.4.2 Waypoints for moving goal tracking

The setup described previously will work well for a single generated workspace. But to extend it over the duration of the person following task, it is necessary to address the navigation function requirement that goal position is not allowed to move inside a workspace. This constraint renders navigation functions, in their original form, unusable for person following applications, where the goal is generally moving. Thus, it is necessary to come up with a description of workspaces which reconciles this contradiction between the requirements of the motivating application and those of navigation functions.

To achieve this, the sensing and path planning modules of the system are decoupled in a specific manner. Since person following is the motivating application

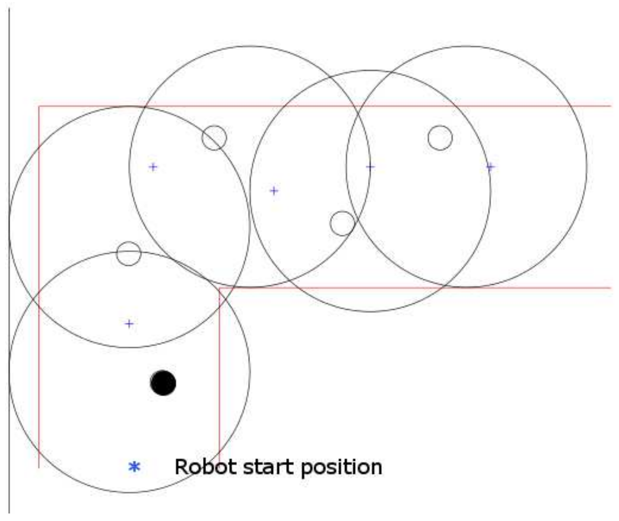

Figure 2.16: Generation of leader waypoints as the robot follows the leader.

The entire L-shaped hallway is represented as an union of of circular workspace envelopes (large black circles). The observed leader trajectory is marked by a number of waypoints (plus signs), each of which is the goal position for its workspace. Waypoint generation allows a moving goal (leader) to be tracked across the hallway using the path planner. Small black circles show obstacles contained within each generated workspace. Note that one obstacle may be common to multiple workspaces.

for this path planner, the 'moving goal' is called the 'leader'. During initialization, the first observed position of the leader is set to be the goal position for the first workspace. This is the first waypoint for the trial.

It is assumed that the sensing module keeps track of the leader even when the leader moves out of the current path planning workspace. The setup is visualized as follows. As the robot moves to the goal position in the $i^{th}$ workspace, its sensing module tracks the leader. On converging to the $i^{th}$ goal, the sensing algorithm has identified the $i + 1^{th}$ goal position. Each workspace contains obstacles which become part of the predictive fields formulation for that workspace. This process continues until the person stops or the robot is commanded to stop following the leader. A sample setup, generated waypoints, and obstacles for each workspace are seen in Figure 2.16. Workspaces are generated so that the predictive fields solution to each workspace is that of robot convergence to a static goal position, shown as a "+" in the figure. Moving obstacles are represented as solid circles.

This completes the description of workspaces such that the robot can follow a person without violating any of the constraints of navigation functions, and without requiring geometric transformations for arbitrarily shaped hallways. Simulation results which demonstrate such a system at work are given in the next section.

### 2.4.3 Simulation results from workspace generation

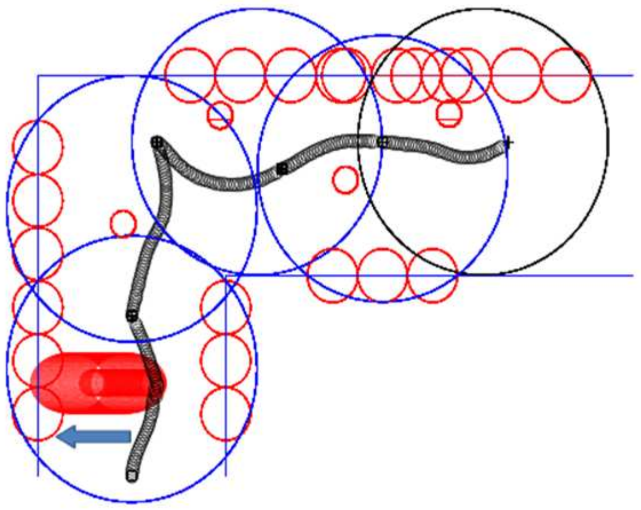

Figure 2.17: Multiple workspaces with predictive fields.

Overlapping black circles show the trajectory of the robot across multiple workspaces, each represented by large blue circles. In the first workspace, the robot avoids a moving obstacle whose path is indicated using overlapping red elliptical envelopes. The blue arrow in this workspace shows the direction of robot motion.

MATLAB Simulink (Mathworks Inc., Natick, MA) was used for simulating the multiple workspace method with waypoint generation. A L-shaped hallway was created to demonstrate the utility of this method. For the simulation, waypoints were generated by arbitrary selection using mouse clicks inside the L-shaped hallway figure. Initial position of the robot was selected using a mouse click; beyond that, the end position of the robot in the current workspace became its start position in the next workspace. Interior obstacles were also manually positioned in the hallway, and their direction of motion was input by the user. Moving obstacles, marked with solid circles in Fig. 2.16, and stationary obstacles, marked with empty circles, were positioned in the workspace. For interior obstacles, motion prediction had to be simulated using variable sized ellipses, the variable size being another user input. The workspace generation method described previously would then automatically determine the wall segments intersecting with the robot's sensing range for a given workspace and generate wall obstacles for a given workspace. It needs to be emphasized that the process of manual selection and labeling was necessary only in the absence of real-world sensing data. A sensing system will render a completely autonomous moving goal system for indoor environments.

Decomposing a hallway into $n$ workspaces worked as expected. This process was designed so that the task was the same as solving $n$ independent navigation function problems. Obstacles were correctly assigned to the individual workspaces by the algorithm, and the robot converged to its goal position in every single workspace, using the velocity control inputs as seen in Fig. 2.14.

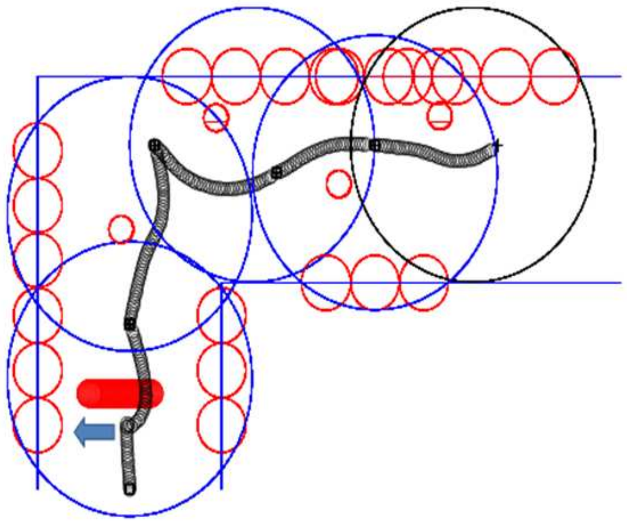

Figure 2.18: Multiple workspaces without predictive fields.

When elliptical fields are not used in the setup identical to Figure 2.17, the robot moves along a hazardous path before it avoids the obstacle. This can be seen in the first workspace, with the overlapping red circles representing the obstacle and the blue arrow indicating its direction of motion.

Fig. 2.17 and Fig. 2.18 illustrate the effect of predictive fields on the path planned for the robot. In the absence of an elliptical field (Fig. 2.18) the robot moves towards the path of the obstacle before the navigation function guides it away from it. This increases the chances of a collision in uncertain environments, and of moving along a path which is less optimal temporally or spatially. In contrast, the elliptical field provides a path in which the robot moves away from the projected obstacle path much earlier, as seen in Fig. 2.17.

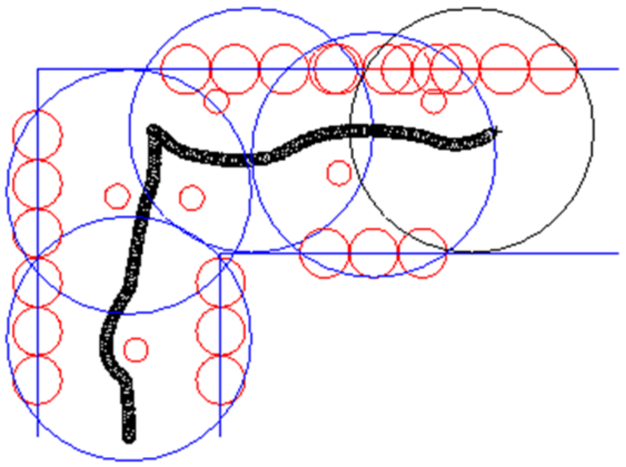

Figure 2.19: Multiple workspaces with stationary obstacles.

When obstacles in multiple workspaces are stationary, the predictive path planning problem reduces to navigation function path planning. The setup shown here is similar to Figures 2.17 and 2.18 but for the positions of stationary obstacles.

It can be seen that, for stationary obstacles, the elliptical field is absent and the predictive formulation reduces to that seen in the classical navigation function systems [72, 61]. An example of this can be seen in Fig. 2.19.

The use of a direction based controller allows for a very standard gain value to be used in the setup. The navigation function only has a single gain $k$ which needs to be tuned; however, this gain is critical to the working of navigation function based path planners. We found that a gain value between $k = 10$ and $k = 15$ in Eq. 2.1 was adaptable to a wide variety of scenarios in our simulated indoor hallway environment. The system scale factor $K_s$, typically a very large gain, was completely eliminated by our choice of controller.

The predictive path planner has thus been developed theoretically, and its performance has been demonstrated in simulated environments. In the next chapter, an experimental setup for mobile robot navigation using the predictive fields path planner is detailed and its results provided.

# Chapter 3

# Experimental verification of predictive fields path planning

Despite mathematical guarantees of convergence and a global minimum at the goal, navigation functions have been limited in their direct applicability to experimental systems. The two principal obstacles in the way have been, (a) the requirement that practical workspace be represented as star world formulations, and (b) the impracticable, high or low magnitude velocity input generated on using the navigation gradient to drive the robot to goal. In the previous chapter, theoretical modifications which make it possible for the predictive fields path planner to be used experimentally have been presented. Here, a step by step explanation for an experimental setup is provided, accompanied by results which demonstrate that predictive fields path planning meets theoretical expectations and replicates simulation results.

The predictive fields path planner reduces to the classical navigation function path planner when the obstacles are stationary. Since the representation of the workspace has been altered to make it more amenable to experiment, this experimental verification of the navigation function path planner may be one of the first such demonstrations of the practicability of navigation functions for path planning.

This chapter begins with an experimental outline and implementation issues and their resolution are discussed in subsequent sections.

## 3.1 Outline of the experiment

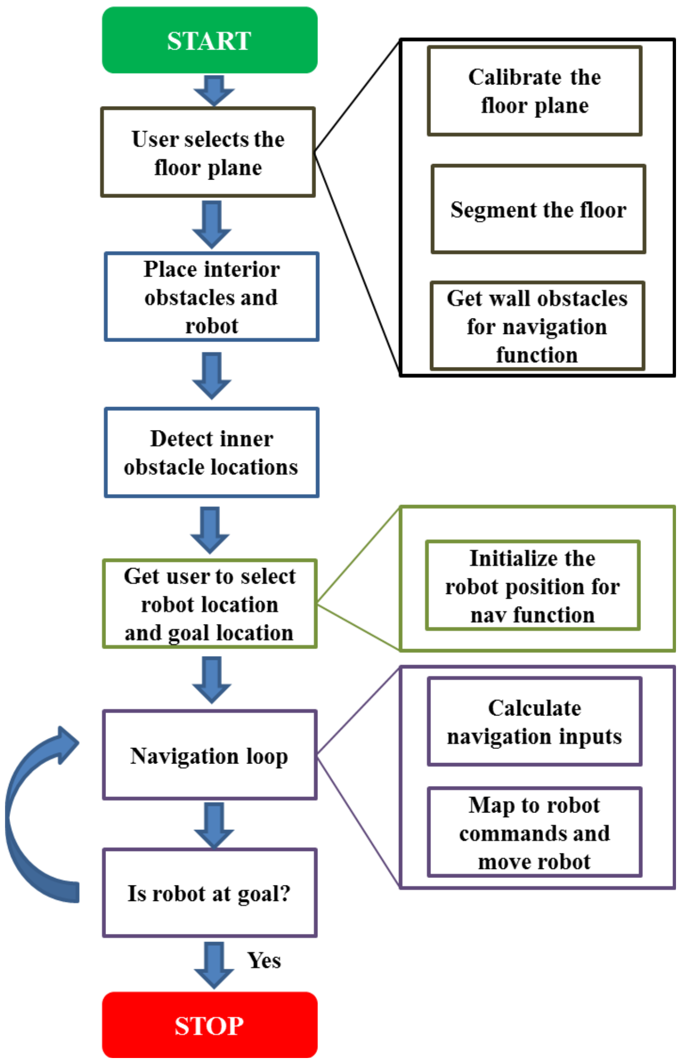
START
User selects the floor plane
Calibrate the floor plane
Segment the floor
Get wall obstacles for navigation function
Place interior obstacles and robot
Detect inner obstacle locations
Get user to select robot location and goal location
Initialize the robot position for nav function
Navigation loop
Calculate navigation inputs
Map to robot commands and move robot
Is robot at goal?
Yes
STOP

Figure 3.1: Procedure for predictive path planning experiment.

The hardware setup for experimental verfication of the path planner is as follows. The Kinect RGB-D sensor is mounted about 2.7 meters above the ground, looking down at the floor, which constitutes the robot workspace. An iRobot Roomba is used as the robot and control commands are issued using its remote control. Switches on the remote control are activated and deactivated using transistor driven relays. The remote control is connected to the path planning implementation on the laptop via a LabJack U3 USB data acquisition device. The Brookstone Rover, controlled by a mobile app, is programmed to travel along a predefined path as the moving obstacle in the experiment.

The software setup for the above hardware configuration is as follows. A Microsoft Visual Studio 10 Solution is created to interface with all the elements of the system. LabJack software libraries provide access to high-level, C/C++ functions to control the ports on the device. Blepo, an open source computer vision library, provides an interface to the Kinect by integrating a number of Microsoft Kinect SDK function calls. Finally, MATLAB provides a COM interface to all of its functions, which is set up in the Visual Studio environment. This interface makes it possible to compute navigation inputs to the robot using MATLAB's symbolic partial differentiation functions.

During the rest of this chapter, references will be made to two types of obstacles: wall obstacles and interior obstacles. This distinction is necessitated by the nature of the experimental setup. Experimental trials consist of optional calibration steps where objects such as the robot and stationary and moving obstacles, have been removed. Walls in the environment are, however, a constant and non-removable feature. 'Internal obstacles' is thus a reference to all obstacles in the workspace which are not wall obstacles. Hence the need for terminology to create a distinction between the two types of obstacles.

The experimental procedure is outlined in Figure 3.1. A trial broadly consists of the following phases:

- Workspace initialization, to identify the floor plane (workspace) and walls.
- Robot and obstacle initialization, to identify starting positions of the robot and other obstaces in the workspace.
- Automated navigation, in which the path planner issues motion commands to the robot for it to avoid obstacles and converge to goal.

A trial begins without the robot and internal obstacles in a workspace. Depth based segmentation is used to identify the robot and obstacles in this workspace. For this type of segmentation to be used, the floor plane equation needs to be estimated. Thus, the first step in any trial is to provide the user the option of estimating the floor plane by selecting an area in the empty workspace. Alternately, since the camera is mounted at a fixed position, calibration may be performed during the first trial and its results used for subsequent trials. After the floor plane is estimated, in a workspace free of internal obstacles and the robot, all points lying outside the floor plane are considered to belong to wall obstacles. Hence, wall obstacles in the workspace are determined.

Next, the robot and internal obstacles are moved into the field of view of the overhead camera. Using depth-based segmentation and image processing operations, candidate robot and obstacle positions are displayed on the user interface. This gives the user an opportunity to select the robot location and goal position. After the wall obstacles and robot position is eliminated from consideration, all remaining obstacles are labeled by the algorithm as being internal obstacles. As per the requirements of navigation function path planning, all obstacles and the robot are enveloped by circles.

From this point forward, the path planner dictates the motion of the robot. A commercially available robot, the Brookstone Rover, is used as the moving obstacle. It's path during the trial is preprogrammed using the Brookstone Rover app for the iOS. An elliptical envelope is constructed around the moving obstacle using principles outlined in the previous chapter. Color based image processing is used to estimate the heading of the robot and correct its orientation to the desired heading calculated by the navigation function. Thus, the 'Navigation Loop' component of the experimental flowchart in Figure 3.1 guides the robot to goal autonomously. Navigation inputs are calculated using MATLAB's symbolic differentiation functions.

In the next section, the interface through which navigation inputs are communicated to the robot is discussed. In sections subsequent to it, the implementation algorithms to successfully complete an experimental trial are outlined.

## 3.2 Controlling the robot

Control commands are issued to the robot based on navigation function inputs. The iRobot Roomba Create is used in this experiment. The possibility of using the Create's programmable serial interface to download the navgiation algorithm to it was considered. The problem with this option is that only the sensors onboard the Roomba can be used for the motion planner. This condition is prohibitive for the predictive fields experiment, since RGB-D cues are being used to provide workspace information to the path planning module. The alternative to downloading a program to the Roomba is then to interface with the robot remotely and issue commands from the program running on the user's laptop.

Such a remote interface is created by using a commercially available Roomba Remote Control to control the robot. The Roomba remote control provides access

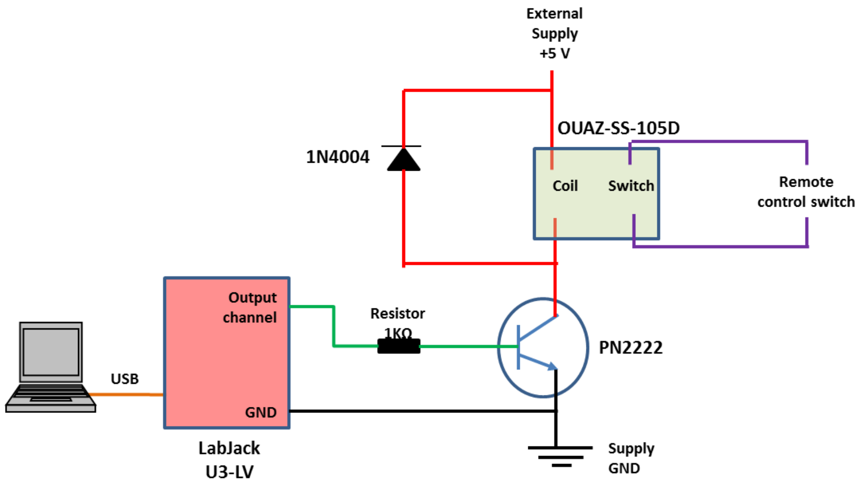

Figure 3.2: Schematic of Roomba remote control interface

The iRobot Roomba is controlled using its remote control, whose switches are activated using OUAZ-SS-105D relays. The relays are controlled by LabJack U3-LV DAC Channels, whose output is boosted using a PN2222 transistor operating in saturation mode. A C++ program interfaces with the LabJack device.

to three mutually exclusive motion commands: rotate clockwise, rotate counter-clockwise, translate forward. These motion commands are compatible with the path planning paradigm for predictive fields. In predictive fields path planning, the robot is provided unit velocity inputs, which means that at any given instant, the robot command is its desired motion direction. Hence, using the Roomba remote control, the robot can be controlled to respond to a navigation input by rotating to its desired orientation, then translating along that direction until the next motion command is received.

The software requirement is to activate and deactivate the remote control switches for these three motion commands using the same C++ program which runs the rest of the experiment. This interface is achieved by using the schematic in Figure 3.2, which shows the interface to one of the three remote control switches, the other two being interfaced in a manner identical to this. The OUAZ-SS-105D relay is used to activate and deactivate the switches. This relay is switched on and off by setting up a PN 2222 NPN transistor to work as a switch. The switching (base) input to this switch is provided by commands from the LabJack U3-LV data acquisition device. The U3 has two DAC channels to interface with two of the three remote control inputs. One of the Digital I/O ports is programmed to output the switching signal to the third remote control input. LabJack U3 has software examples to show how it can be controlled by a Visual Studio 6.0 program. With minimal modifications, the same setup was used for the Visual Studio 10 Solution which ran this experiment.

## 3.3 Workspace and wall obstacle representation

Workspace and wall obstacle representation comprises of the following components:

- Identification of the plane of the workspace
- Identification of wall obstacles using segmentation

Establishing the workspace plane is useful for the idenfication of the robot and internal obstacles. Further, knowing the extent of the workspace is required for identification of the workspace envelope, which contributes to one of the repulsive terms in the navigation function. Walls are static obstacles which are also represented in the navigation function using repulsive terms. Moreover, they are also immovable objects in the workspace. Hence, they need to be identified, segmented, and represented at the same time as the plane of the workspace. Once the workspace and wall positions have been deduced, the robot and internal obstacles are introduced into the workspace. The knowledge of the floor plane equation is used to segment these objects from the background of the workspace plane using depth. The details of this initialization process are explained in this section.

### 3.3.1 Floor plane estimation

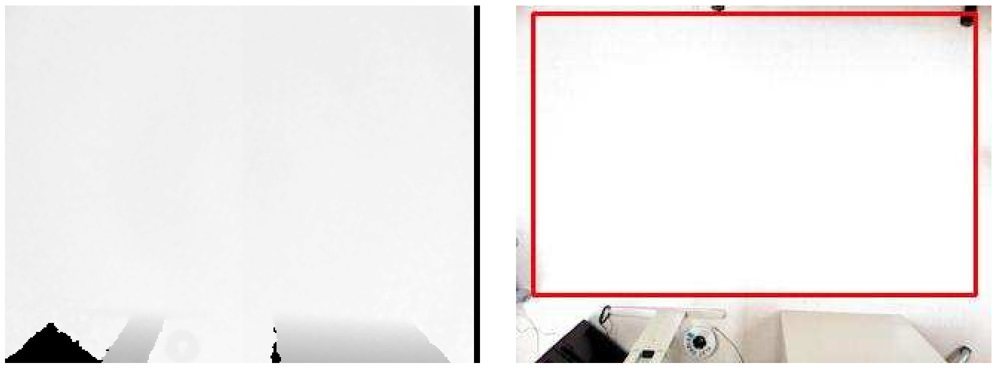
(a) Floor area is selected by the user. (b) Corresponding area in the color image.

Figure 3.3: Selection of points for estimation of floor plane equation.

To estimate the floor plane equation, the user selects a rectangular area in the depth image. Its corresponding region in the color image is shown using a red rectangle. All points inside the area are used in formulating the least squares solution to the floor plane equation.

The Kinect RGB-D sensor gives access to depth data, which in turn can be converted to a 3D coordinate system using the camera calibration matrix specific to this sensor. Assuming that the workspace is planar, the equation of the plane can be estimated using a set of labeled floor points. Any point in the depth image not satisfying the floor plane equation can thus be labeled as a point on a potential obstacle. This labeling serves as the initial step towards detection of the robot and other obstacles.

Floor plane estimation begins with a workspace without either the robot or one of the interior obstacles in the field of view. The estimation step allows the user to select an area in the color or depth image, as seen in Figure 3.3. All points in this area are considered for floor plane estimation. The floor plane can be represented by the equation

$$z = ax + by + c \tag{3.1}$$

where the triplet $(x, y, z)$ represents 3D coordinates of a point (in meters), and $a$,$b$,$c$ are floor plane parameters. Floor plane parameters are estimated using a least squares formulation [88],

$$Af = B \tag{3.2}$$

where

$$A = \begin{bmatrix} \sum_{i=1}^{N} x_i^2 & \sum_{i=1}^{N} x_i \cdot y_i & \sum_{i=1}^{N} x_i \\ \sum_{i=1}^{N} x_i \cdot y_i & \sum_{i=1}^{N} y_i^2 & \sum_{i=1}^{N} y_i \\ \sum_{i=1}^{N} x_i & \sum_{i=1}^{N} y_i & N \end{bmatrix}$$

$$B = \begin{bmatrix} \sum_{i=1}^{N} x_i \cdot z_i \\ \sum_{i=1}^{N} y_i \cdot z_i \\ \sum_{i=1}^{N} z_i \end{bmatrix}$$

In the above formulation, $N$ points are used for the least squares fit, $\begin{bmatrix} x_i & y_i & z_i \end{bmatrix}$ being the 3D coordinates of each point. The solution of the least squares equation is the vector $f$, the elements of which are the desired coefficients of the floor plane equation, i.e.

$$f = \begin{bmatrix} a \\ b \\ c \end{bmatrix}$$

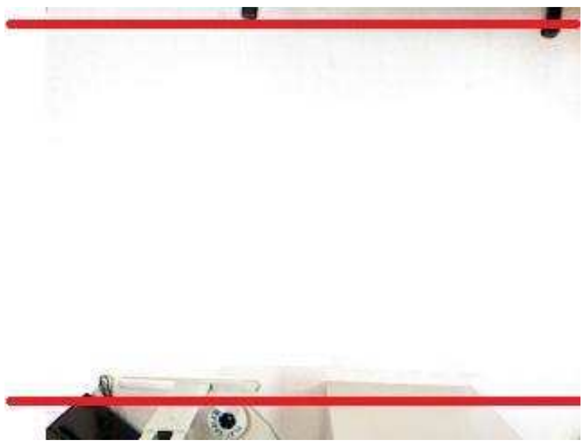

Figure 3.4: Labeling wall obstacle lines.

For a fixed setup, wall obstacles are defined using lines labeled by the user. The user selects two points in the color image, and the $y$ coordinates of these points are used to create horizontal red lines spanning the image. Evenly spaced wall obstacles are created given these user-defined lines.

## 3.3.2 Labeling wall obstacles

Identifying the position of walls in the workspace is another initialization procedure. Since wall locations are assumed to be fixed for the experimental setup, this is a single time labeling process which need not be repeated for each trial. The user is asked to label two points $[x_{top}, y_{top}]$ and $[x_{bottom}, y_{bottom}]$ in the depth image, to approximate the $y$ coordinates of the wall lines at the top and bottom of the image respectively. The lines $y = y_{top}$ and $y = y_{bottom}$, shown in Figure 3.4, are then used to set up wall obstacles. In keeping with the requirements of the navigation function setup, these line segments are divided into non-overlapping circular wall obstacles.

## 3.3.3 Depth based segmentation

Depth based segmentation, during initialization and over the course of the trial, serves as the input to the tracking algorithm for the positions of internal obstacles, and the robot. Wall obstacle locations, as determined by the user labeling in

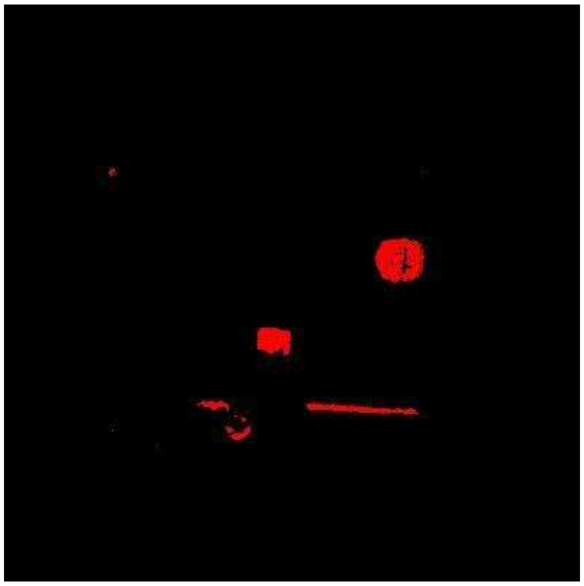

Figure 3.5: Occupancy map generated after floor segmentation

Each pixel in the depth image is colored red or black to indicate whether it is a floor plane pixel or not. A red pixel indicates that the pixel is 'occupied', i.e. it does not belong to the floor plane. Later steps in the algorithm decide whether this pixel belongs to an obstacle, robot, or the walls of the workspace.

the previous section, are ignored during the depth based segmentation step.

The floor plane, as determined using the above process, is considered to be the 'background' for depth based segmentation. The 'foreground', then, is the set of all points which do not lie on the floor plane. An empirically observed threshold is chosen to separate foreground points in the depth image from the background. The value of this threshold is sensitive to the positioning of the camera.

Consider a point $i$ in the depth image with pixel coordinates $\left(x_i^d, y_i^d\right)$ and corresponding 3D coordinates $(x_i, y_i, z_i)$. Using equation 3.1, let the estimated $z$ value of this point be $z_i^{est}$. Let the floor segmentation threshold be $\epsilon_{floor}$. Then, the point is labeled as a floor point if it satisfies the condition,

$$\left|z_i^{est} - z_i\right| < \epsilon_{floor} \tag{3.3}$$

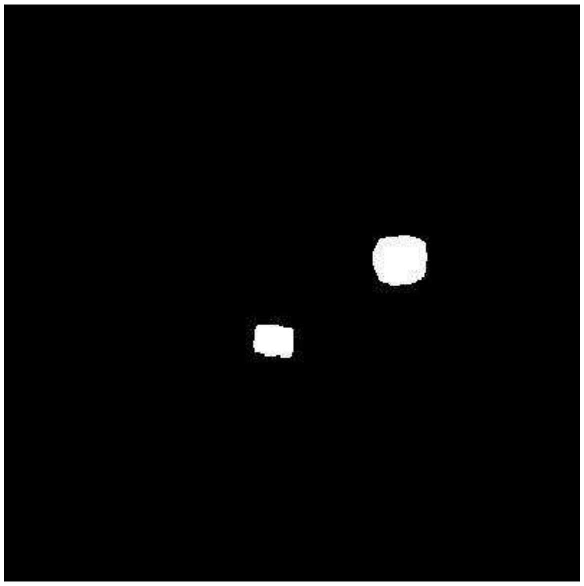

Figure 3.6: Morphological processing of occupancy image

The raw data from Figure 3.5 is processed to generate this binary image which is used to detect robot and inner obstacle positions. Wall pixels are discarded, and the remaining pixels are operated upon by morphological operators. This gives foreground regions (white blobs) which can be processed as robot or internal obstacle candidates.

For an overhead camera view, it was found that a threshold of $\epsilon_{floor} = 0.07$ was required to discriminate between the floor plane and other elements of the workspace.

The outcome of this segmentation process is an occupancy map as seen in Figure 3.5, where the red pixels are non-floor points. Since the floor segmentation threshold is chosen empirically, some noisy foreground pixels are likely to appear in an occupancy map. To filter out the noise and retain genuine foreground areas, morphological operations such as erosion and dilation are applied to the occupancy map. The outcome of morphology, as seen in Figure 3.6 is a clean binary image in which most of the noise has been removed.

## 3.4 Robot and internal obstacle tracking

After wall obstacles have been identified and the floor has been segmented, the positions of the robot and internal obstacles need to be updated over time. Initial positions of these objects is set using user input. After initialization, the trial enters the fully autonomous Navigation Loop phase as shown in Figure 3.1, and 'tracking by detection' is used to match detections to determine the current position of these objects. In addition to tracking, robot heading needs to be estimated for each iteration of the trial. This is done using color segmentation. Each step of the tracking process is explained in this section.

### 3.4.1 Tracker initialization

Morphological processing (Figure 3.6) results in blobs which are processed further using connected components. Areas which are too small or too large (determined by expected size of robot and obstacles in the occupancy image) are filtered out. Areas which belong to wall obstacles have already been filtered out during pre-processing before morphology.

Thus, the remaining connected regions are either internal obstacles or the robot. The center and bounding box of each region provides enough information to encapsulate them using circles, as required by navigation functions. User input is now required to establish which of these candidates is the robot. The selected robot position in the occupancy map in frame 0 is $[x_0^{robot}, y_0^{robot}]$. This is represented by a white circle around the object, as seen in Figure 3.7. Every other object is now classified as an internal obstacle. The $i_{th}$ internal obstacle at frame 0 is represented using occupancy map coordinates $[x_0^i, y_0^i]$. A blue circle in Figure 3.7 denotes internal obstacles.

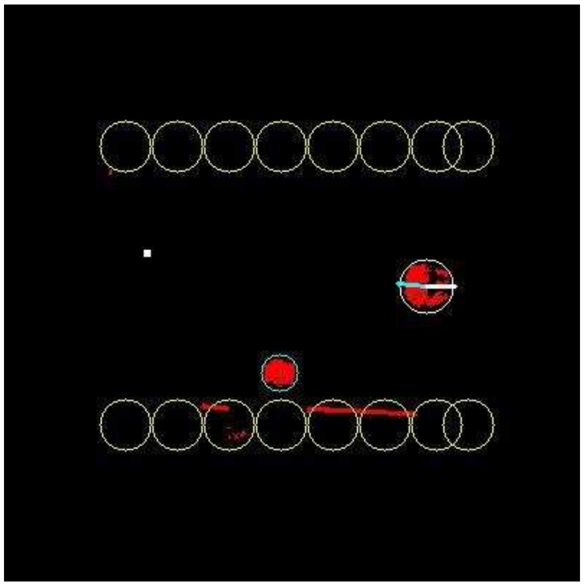

Figure 3.7: Initialization of the internal object tracker

Adjacent circles at the top and bottom of the image are wall obstacles. The robot is at the right, enveloped by a white circle. The white line inside the circle indicates the desired robot orientation, the blue line indicates its observed orientation. Desired heading defaults to 0°, but a navigation input is calculated before the robot reacts to this value. The small blue circle around a red blob at the center is the detected inner obstacle. The robot moves to the goal position, indicated by a white square near the left extreme of the workspace.

To complete the intialization of the tracker, and the path planning experiment in general, a goal position is selected by the user inside the occupancy map. This can be seen as a white square near the left end of the workspace in Figure 3.7.

### 3.4.2 Robot and obstacle tracking

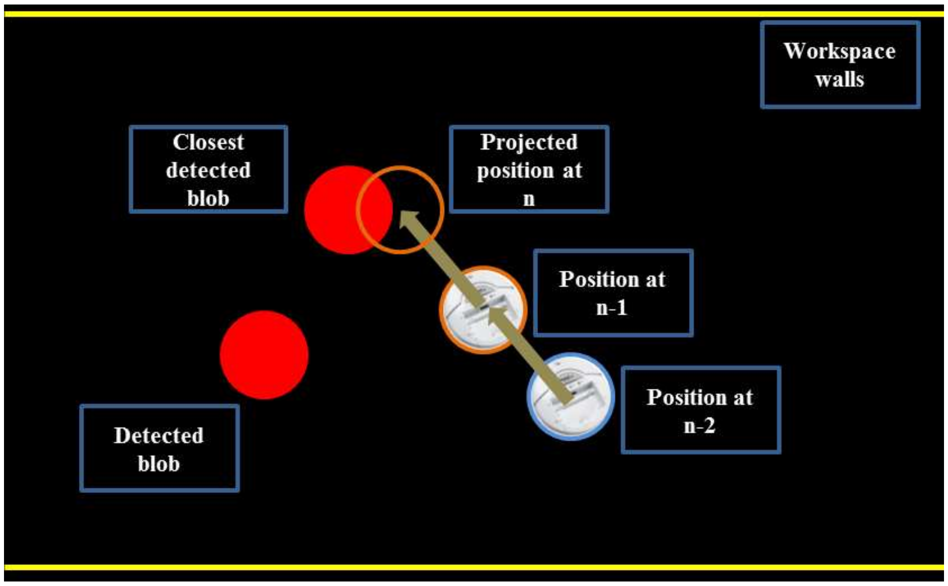

Figure 3.8: Prediction of object position and matching to detected blob

Internal object detections, using depth based segmentation (Section 3.3.3), are matched to get the tracker output. Figure 3.8 is a representation of the object tracking process. The first step in matching detections is predicting the current positions of objects based on their motion history. A simple, linear prediction model is used to predict object locations for the current iteration $n$, although more sophisticated algorithms such as Kalman filters may conceivably be used for the same purpose. For an object located at $[x_{n-1}, y_{n-1}]$ during iteration $n-1$ and at $[x_{n-2}, y_{n-2}]$ during iteration $n-2$, the predicted position $[\bar{x}_{n+1}, \bar{y}_n]$ during the current iteration $n$ is given by

$$\begin{aligned}
\Delta_x &= x_{n-1} - x_{n-2} \\
\Delta_y &= y_{n-1} - y_{n-2} \\
\bar{x}_{n+1} &= x_{n-1} + \Delta_x \\
\bar{y}_{n+1} &= y_{n-1} + \Delta_y
\end{aligned}$$

Each detected internal object is projected to an expected current position in this manner. These expected positions are then matched to blob detections from depth segmentation, and each object gets assigned the blob closest to its predicted position. The value of computing expected positions for the robot and each internal obstacles is in disambiguating blobs which are close to each other. Such a situation is commonly observed when the robot is moving past an obstacle.

### 3.4.3 Robot heading estimation

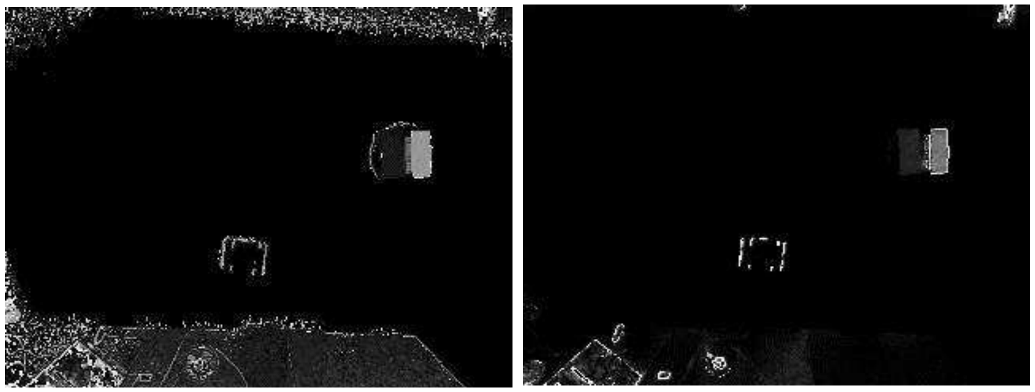

Figure 3.9: Calibration of hue and saturation values to identify markers

Front and back marker Hue-Saturation values are calibrated using user input. The user marks one point each on the front and back markers in the hue image (left) and saturation image (right).

The robot is issued directional navigation commands in the form of heading inputs in degrees. Following a navigation command, the robot heading is corrected to the desired heading, and the robot translates along this heading until the next navigation command is available. Correcting robot orientation requires accurate feedback, which makes heading estimation an important module in the path planning implementation.

The position of the robot and a bounding box for it in terms of occupancy

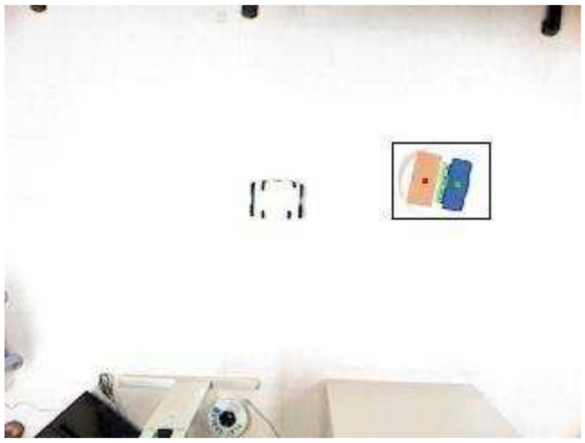

Figure 3.10: Output of heading estimation

Given the hue-saturation calibration from Figure 3.9, robot heading can be detected. The red dot on the front (orange) pad indicates the estimated center of the front marker, and the green dot on the back (blue) pad indicates the estimated center of the back marker.

map coordinates is available after tracking. To distinguish the front and back of the robot, colored markers are placed on the top of the robot. Marker color values are calibrated in terms of Hue and Saturation from the HSV colorspace. Conversion from RGB to HSV provides access to a color space in which the illumination variant component (Value) is separated and hence color detection is more robust to effects such as shadows. For a fixed, indoor setup, front and back marker calibration needs to be done just a single time. It is done by allowing the user to click somewhere on the front and back marker in the hue and saturation images, as seen in Figure 3.9. A tolerance around the values at the selected image pixels creates a minimum and maximum threshold for hue ($[H_{min}^{front}, H_{max}^{front}]$ and $[H_{min}^{back}, H_{max}^{back}]$ ) and saturation ($[S_{min}^{front}, S_{max}^{front}]$ and $[S_{min}^{back}, S_{max}^{back}]$). The range of values for hue and saturation is $[0 \ldots 1]$.

During a trial, positions of these markers are estimated by identifying color image pixels satisfying calibrated color values for the front and back marker. Search for these matching color pixels is restricted to the robot bounding box. Thus, for a point with pixel coordinates $[x_i, y_i]$, with hue and sat values $H_{[x_i,y_i]}$ and $S_{[x_i,y_i]}$ respectively, if

$$\begin{aligned} H_{min}^{front} &< H_{[x_i,y_i]} < H_{max}^{front}, \text{ and} \\ S_{min}^{front} &< S_{[x_i,y_i]} < S_{max}^{front} \end{aligned}$$

then it belongs to the front marker, and if

$$\begin{aligned} H_{min}^{back} &< H_{[x_i,y_i]} < H_{max}^{back}, \text{ and} \\ S_{min}^{back} &< S_{[x_i,y_i]} < S_{max}^{back} \end{aligned}$$

then it belongs to the back marker.

The centroids of the front and back markers are calculated, and the orientation of the line connecting them gives the heading of the robot for the current iteration. An example of this estimation output is seen in Figure 3.10. The red marker in the figure shows the estimated location of centroid of the front marker. The green marker is the estimated location of the centroid of the back marker.

When obstacles are being tracked, the predictive fields algorithm dictates that their motion be represented using ellipses as explained in Section 2.2. Ellipse generation for obstacles during run-time is explained in the next section.

### 3.4.4 Obstacle ellipse generation

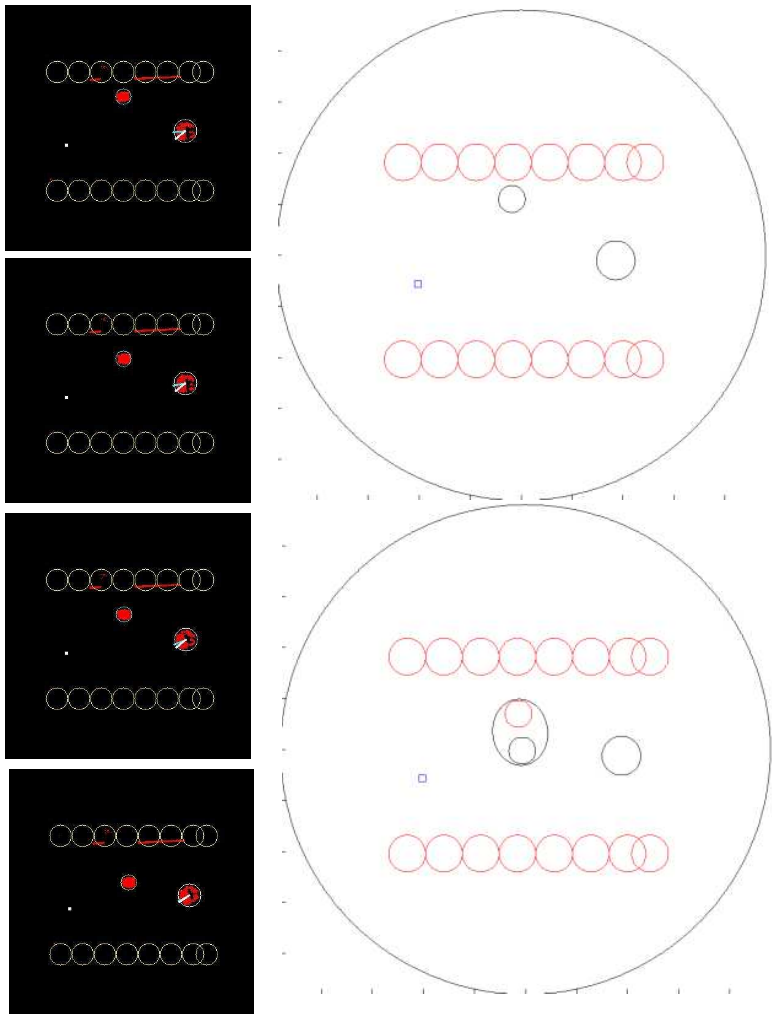

Figure 3.11: Generation of obstacle ellipse

The four images on the left show different frames leading to ellipse generation. The characteristic features of each image are explained in Figure 3.7. The obstacle, at the center of each image and enveloped by a blue circle, moves downward. As more information about the obstacle motion becomes available, its ellipse can be generated. The generated ellipse can be seen in the two MATLAB plots to the right. The red circle shows the actual position of the obstacle, and the black circle shows its projected position inside the elliptical envelope. When not enough information about obstacle motion is available, the red and black circles overlap, as seen in the top image.

The path planner proposed in the previous chapter can be tested experimentally only after obstacle motion is represented in the form of an elliptical field. Obstacle ellipses are generated based on the knowledge of the direction vector of the obstacle. For a proof of concept experiment, the following assumptions are made for ellipse generation:

- The obstacle moves along a straight line.
- The obstacle moves with a constant velocity.

This type of obstacle motion can then be encapsulated using an ellipse at a fixed orientation and of a fixed size. These assumptions can be easily relaxed for a implementation of a practical system which uses predictive fields path planning.

The orientation vector for an obstacle is generated after observing its positional variation over a few iterations of the trial. If the obstacle has displaced sufficiently from its initial position, it is considered to be a moving obstacle and an ellipse is generated for it. Figure 3.11 shows this process. Occupancy maps on the left of the figure show tracked positions of the robot and internal obstacles over a few iterations at the beginning of the trial. The figures to the right are the representation of this data in a form required by navigation functions, i.e. the entire workspace and objects in it are assigned circular envelopes. As the position of the obstacle changes over a few iterations of the trial, there is enough displacement to label it a 'moving obstacle' and assign an ellipse to it. The first frame at the top left of the figure is the beginning of the trial, the last frame at the bottom left is the iteration where obstacle ellipse is generated. The top right and bottom right representations correspond to these two iterations.

For the experiment, the moving obstacle was a Brookstone Rover robot. This robot can be controlled by a mobile phone app and one of the possible control modes is to record and replay a sequence of motions. This mode allowed the moving obstacle to move along a predefined linear trajectory during the trial.

The setup for an experiment is thus completed, and results from the trials are highlighted in the next section.

## 3.5 Results

The experimental trials described here were carried out in a fixed workspace, hence obviating the need for repeated calibrations. As seen in the following sections, results corroborated the findings of simulated data regarding the efficacy of predictive fields path planner in dynamic environments.

### 3.5.1 Parameter settings and test configurations

The system was calibrated once and the same settings were used for all trials. Floor plane parameters from Eq. (3.1) were: $a = 0.02$, $b = 0.04$, and $c = 2.39$, with a floor plane segmentation threshold from Eq. (3.3) of $\epsilon_{floor} = 0.07$. Color thresholds for front and back marker detection (in the range $[0 \ldots 1]$ for robot heading estimation were:

$$\begin{aligned} H_{min}^{front} &= 0 \\ H_{max}^{front} &= 0.16 \\ H_{min}^{back} &= 0.5 \\ H_{max}^{back} &= 0.75 \\ S_{min}^{front} &= 0.27 \\ S_{max}^{front} &= 0.47 \\ S_{min}^{back} &= 0.31 \\ S_{max}^{back} &= 0.54 \end{aligned}$$

There are two tuning paramters for the path planner. Of these, the most important is the value of the navigation gain $k$. Based on data from simulations, the tuned

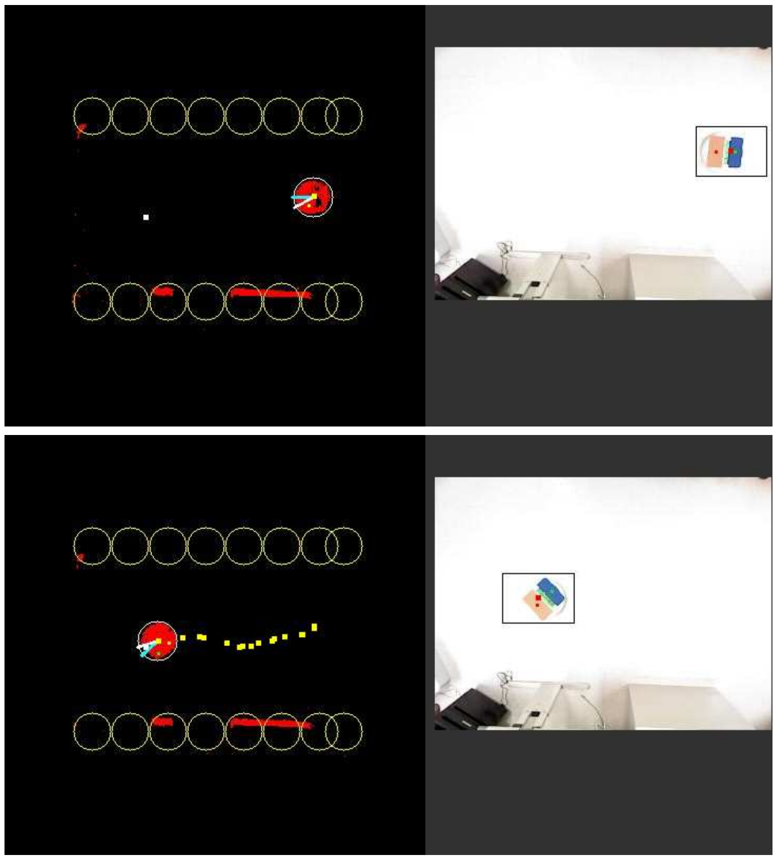

Figure 3.12: Convergence to goal with no obstacles

Robot navigation to goal with no internal obstacles, as seen using workspace image to the left and color image to the right. The workspace image at the top shows initial position of the system. The bottom image shows the final position of the system, with the trail of yellow dots showing various intermediate positions occupied by the robot on its way to goal.

value of this gain was $k = 15$. The 3D values observed by the Kinect (in mm) were scaled to approximately the range used for simulating the path planner. This scaling resulted in the simulation $k$ value of 15 working perfectly for all experimental trials.

Because of the procedure of the experiment, it was found that the translational resolution of robot motion was not adequate for the robot to converge exactly to goal. In early trials, this led to the robot moving around its desired goal position. This being a limitation of the robot used, an arbitrary stopping distance of $5cm$ was introduced in the algorithm. This meant that the trial would be terminated as soon as the distance between the robot and the goal position decreased below the stopping distance.

To demonstrate the completeness of the path planning experimental setup, results from different configurations, in an increasing order of complexity, are presented in this section. The test configurations are as follows:

- Convergence to goal with no internal obstacle
- Convergence to goal with a single internal obstacle
- Convergence to goal with two internal obstacles
- Two examples of convergence to goal with a moving obstacle, no elliptical fields
- Two examples of convergence to goal with a moving obstacle using elliptical fields

Results are presented as a collage of two images: the color image from the Kinect with the robot bounding box and front and back marker centroids overlaid, and occupancy map with the robot and obstacles encapsulated with circular envelopes. In all cases, the goal position is marked using a white square. Manual labeling on every $n^{th}$ iteration is used to show the robot path over the trial. This path is shown as a sequence of yellow squares. In the occupancy map, the robot has two additional lines overlaid on it. The white line shows the desired orientation of the robot, whereas the blue line shows the estimated orientation of the robot. Rotation commands are issued to correct this error before translating the robot.

The first case presented is the most basic: robot converging to the goal in the absence of internal obstacles. Wall obstacles are considered permanent to the workspace and hence, as discussed earlier, a distinction is made between them and removable obstacles, which are labeled as being internal obstacles. Figure 3.12 shows the navigation output with zero internal obstacles. Workspace radius, denoted in the path planner configuration as $r_{o0}$ is set to an arbitrary value large enough to encompass the entire field of view of the Kinect. As seen in the figure, robot converges to goal following nearly a straight line path, as may be expected for such a test case.

### 3.5.2 Stationary obstacles

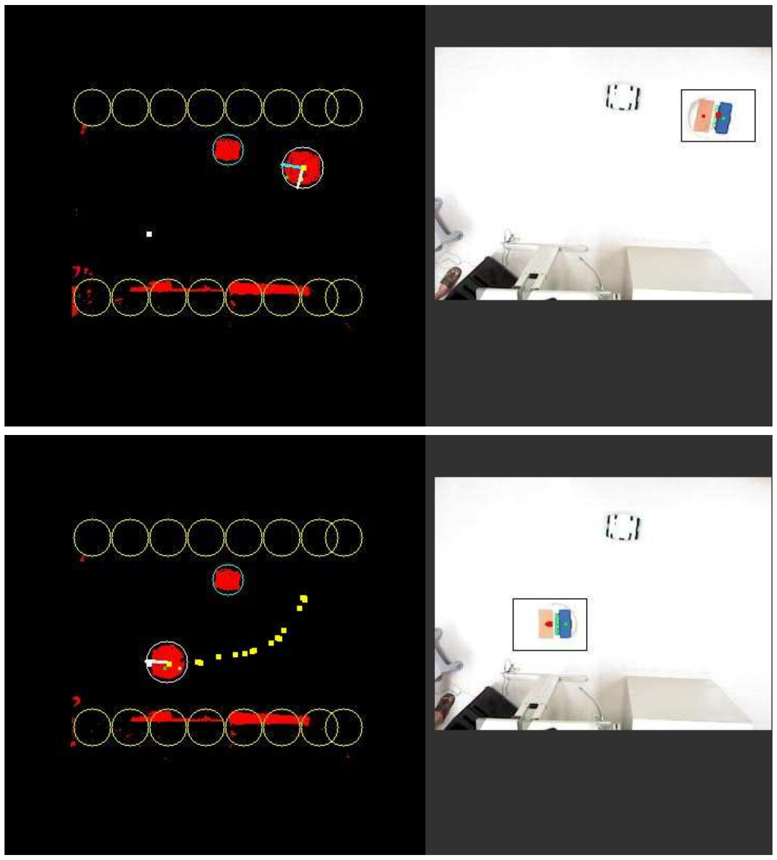

Figure 3.13: Convergence to goal with a single stationary obstacle

Robot navigation to goal with one internal obstacle, as seen using workspace image to the left and color image to the right. The robot navigates from its original position, shown using a white circle with white and blue heading lines in the top image, to its goal position in the bottom image, with its path indicated using yellow dots. The obstacle, shown using a blue circle, stays in the same position throughout the trial.

Figure 3.13 shows the convergence to goal with a single stationary obstacle in the workspace. The robot starts close to both the stationary obstacle and the walls, but it guided away from both by the path planner to converge to a goal position on the other side of the workspace. The stationary obstacle is encompassed by a blue circle.

Figure 3.14 shows the convergence to goal with two stationary obstacles. The

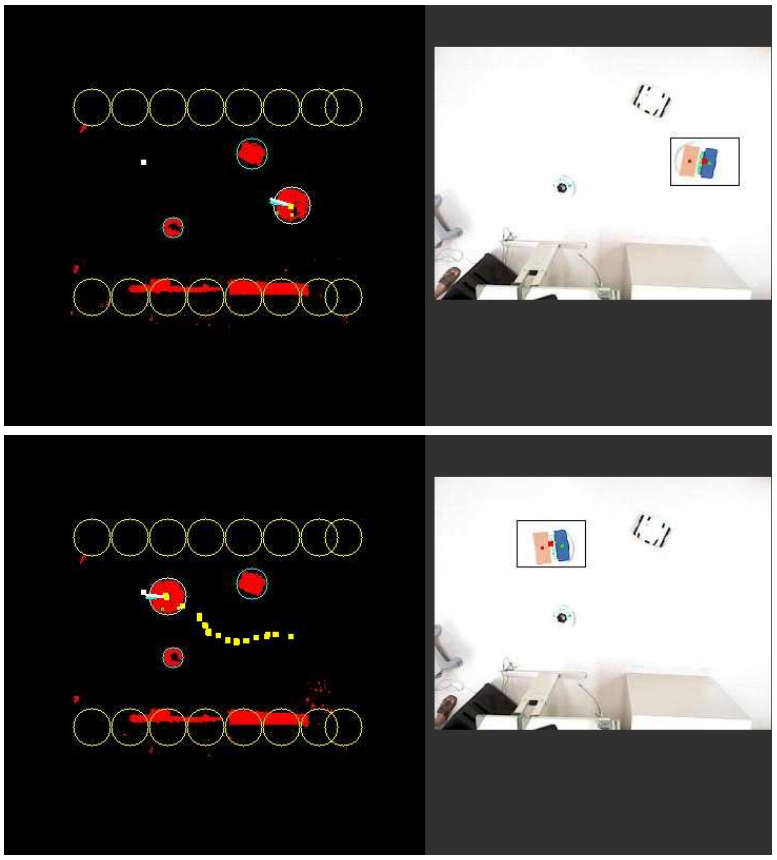

Figure 3.14: Convergence to goal with a two stationary obstacles

Robot navigation to goal with two internal obstacles, as seen using workspace image to the left and color image to the right. The robot navigates from its original position to its goal position in the bottom image, with its path indicated using yellow dots. Both obstacles, shown using blue circles, stay in the same position throughout the trial and are successfully avoided by the robot.

occupancy figure on the left of this collage shows some artifacts in the form of red dots lying outside any of the obstacles. This is a good example of the combination of depth segmentation and morphology working to filter out the ‘noisy’ obstacle detections by enforcing a minimum area restriction for a non-floor detection to be classified as an obstacle. The robot converges to goal by following the path planning solution which guides it between the obstacles while avoiding collisions.

With stationary obstacles in the workspace, predictive fields path planning reduces to the standard form of the navigation function path planner. Hence, all test cases with stationary obstacles are also examples of the classical navigation function path planner at work.

### 3.5.3 Moving obstacles

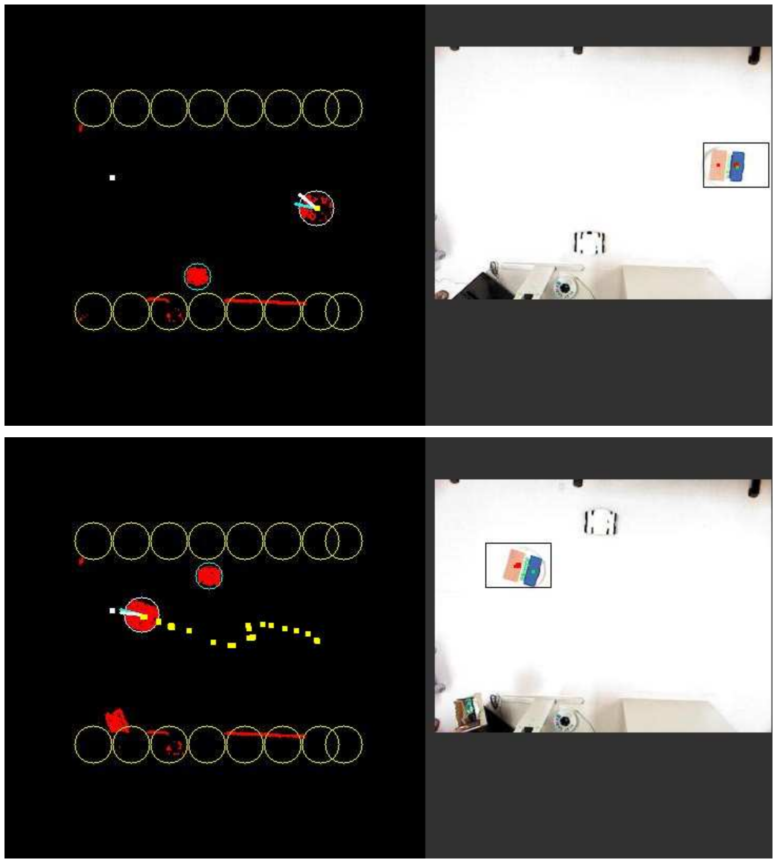

Figure 3.15: Example 1 of convergence to goal with moving obstacle, no ellipse.

Robot navigation to goal with one moving obstacle, as seen using workspace image to the left and color image to the right. The characteristic features of each image are explained in Figure 3.7. The obstacle, shown using a blue circle, moves from the bottom of the workspace to the top. The robot path, in the absence of obstacle motion prediction, takes it close to the path of the obstacle before it pulls away to get to the goal, as evidenced by the trail of yellow dots with a noticeable 'dip' in the middle.

Predictive fields are used to represent the motion of an obstacle by drawing an ellipse around the obstacle and by projecting its position along the major axis of this directional ellipse. In conventional navigation function path planning, there is no such provision for incorporating obstacle motion into the path planning framework. For the experiment, a few iterations of obstacle motion data are used before an

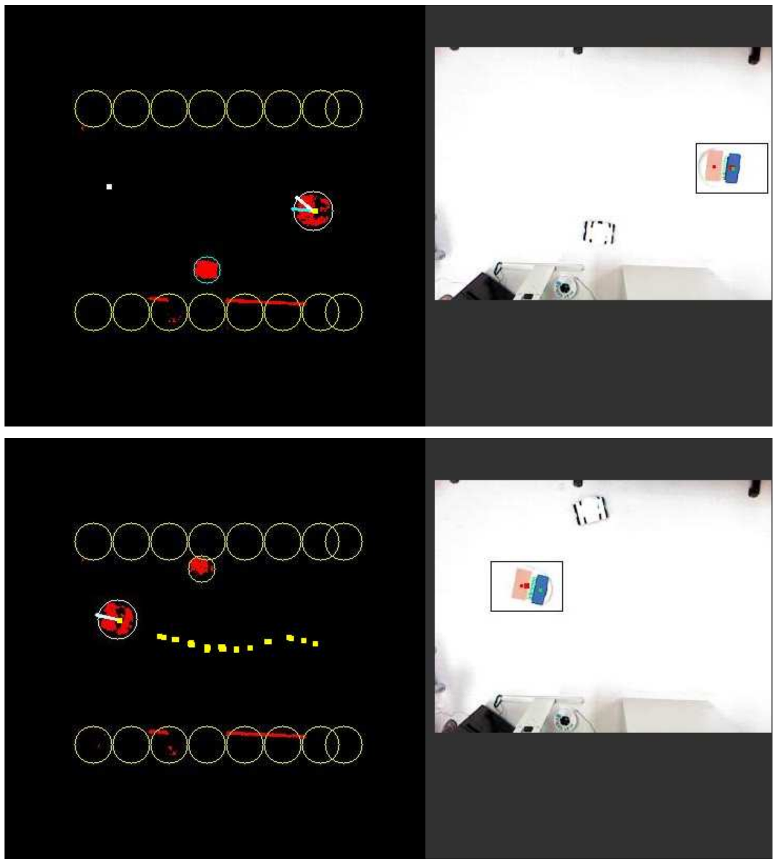

Figure 3.16: Example 1 of convergence to goal with moving obstacle with ellipse.

Robot navigation to goal with one moving obstacle with predictive fields. The setup here is exactly the same as Figure 3.15. Given obstacle motion prediction, the robot preempts obstacle motion and steers clear of its path to move smoothly to goal, as evidenced by the trail of yellow dots indicating its path.

ellipse is generated. The practical reason for this is that there is some variation in floor segmentation results for each depth image. The variation is a result of slight variation in depth readings from the Kinect sensor. This results in a 'wobble' around the true position even for stationary obstacles. To prevent stationary obstacles from being assigned predictive ellipses, a few frames of observation are allowed to pass before ellipse generation.

Figure 3.15 shows the effect of not capturing the motion of the obstacle in the path planning algorithm. The robot navigation input is calculated based on the

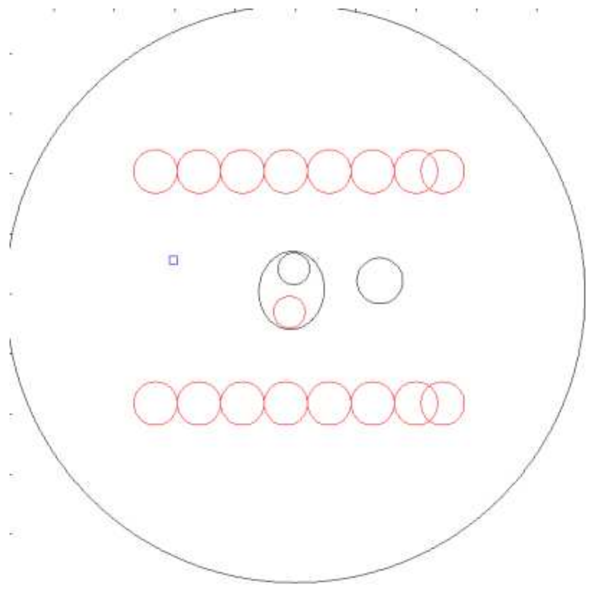

Figure 3.17: Example 1 with ellipse generated around obstacle.

Workspace information from the C++ program is communicated to MATLAB's COM server, and the obstacle position and ellipse are visualized using a MATLAB plot. The robot is at the right of the image and is shown using a black circle. The moving obstacle is at the center of the image, with its actual position shown using a red circle and predicted position using a black circle. The enveloping ellipse is that generated by the predictive fields path planner. The robot converges to the goal, marked with a blue square, in the presence of internal obstacle and wall obstacles, marked using red circles. The biggest black circle represents the workspace boundary.

current obstacle position, which takes it close to the obstacle before a rerouting is required to push it away and back towards the goal. This is contrasted with the ellipse being used for the obstacle, in which case the trajectory to goal is much smoother and the robot continues along approxiamtely a straight line path with the confidence that the obstacle is moving out of its path. As described earlier, the obstacle ellipse is created after a few frames of observation. In the figure, this is denoted by a change in the color of the moving obstacle's circular envelope. Before ellipse generation, the envelope is blue, and after an ellipse has been generated, the envelope color changes to yellow.

The generated elliptical envelope can be seen in Figure 3.17. In the figure, actual position of the obstacle is represented by a red circle, whereas its predicted position is represented using a black circle. The black circle is the position for which the repulsive term for navigation is calculated when predictive fields are used. Without the use of predictive fields, the red circle is used for calculating this term.

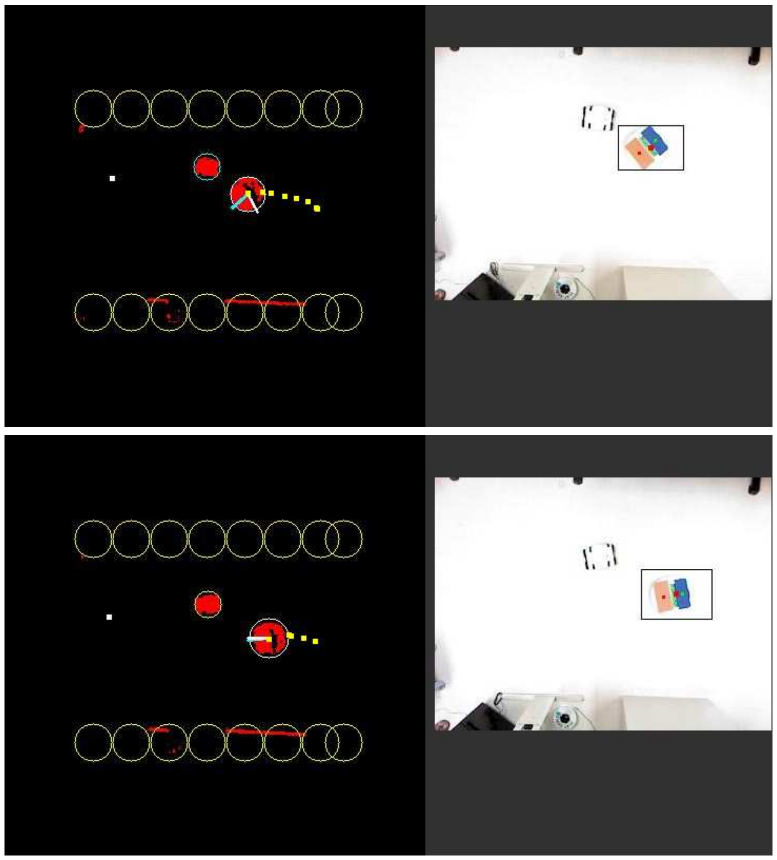

Figure 3.18: Example 1: Comparing robot positions with and without use of ellipse

When elliptical information is not used, the robot is at a greater risk of moving close to collision with the obstacle. The top image shows an hazardous robot position without the use of elliptical information. The robot path, shown using a trail of yellow dots, comes very close to the obstacle, enveloped by a blue circle. A big heading correction, shown by the white 'desired heading' line is needed to steer the robot away from harm. As opposed to this, the use of elliptical fields in the lower image keeps the robot away from the obstacle's projected position.

Not only does the use of elliptical fields make for more efficient navigation, but also pushes the robot close to colliding with the obstacle. This situation is avoided using the elliptical position field shown in Figure 3.16. The effect of the robot being pushed too close to the obstacle can be seen in Figure 3.18. It can be seen that, at approximately the same position of the obstacle, the robot guided by predictive fields (bottom image in the collage) is comfortably away from the obstacle when compared

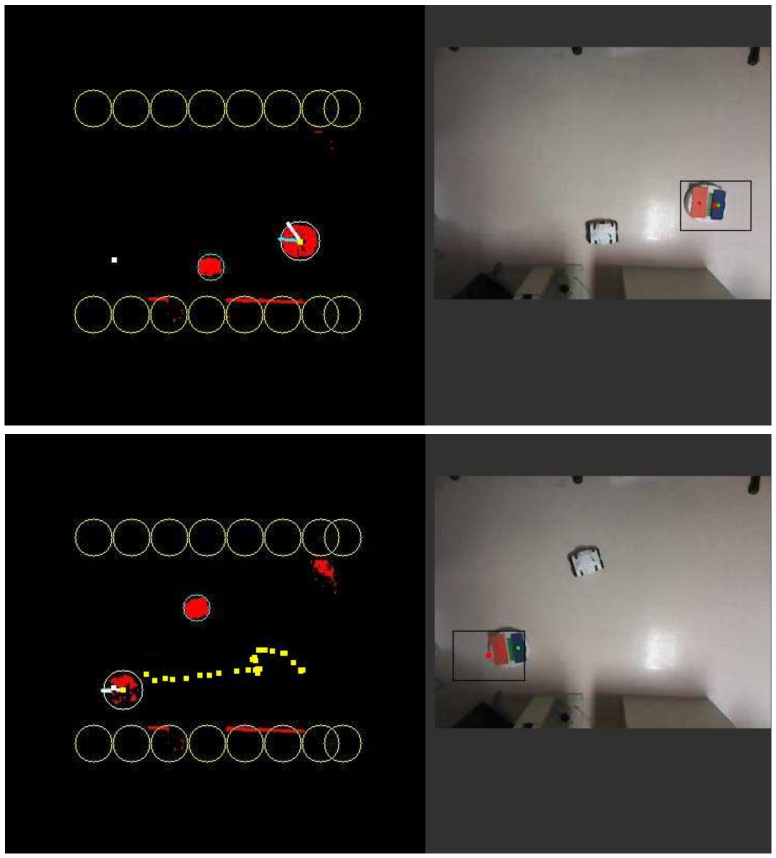
Figure 3.19: Example 2 of convergence to goal with moving obstacle, no ellipse.

Without obstacle ellipses, the robot moves towards the obstacle's path, as seen in the lower image. Even the initial motion input, shown by the white line inside the white robot circle, takes the robot towards the obstacle, which is moving from the bottom of the workspace to the top. The trail of yellow dots shows the complete robot path in the absence of elliptical information.

to the trial without the use of the ellipse (top image in the collage).

Another example of robot navigation with and without the ellipse can be seen in Figures 3.19 and 3.20. A pronounced reorientation of the trajectory is seen in Figure 3.19, which is the trial where predictive fields are not used. In Figure 3.20, the robot converges to goal making use of obstacle motion information. Figure 3.21 shows the generated ellipse for this trial.

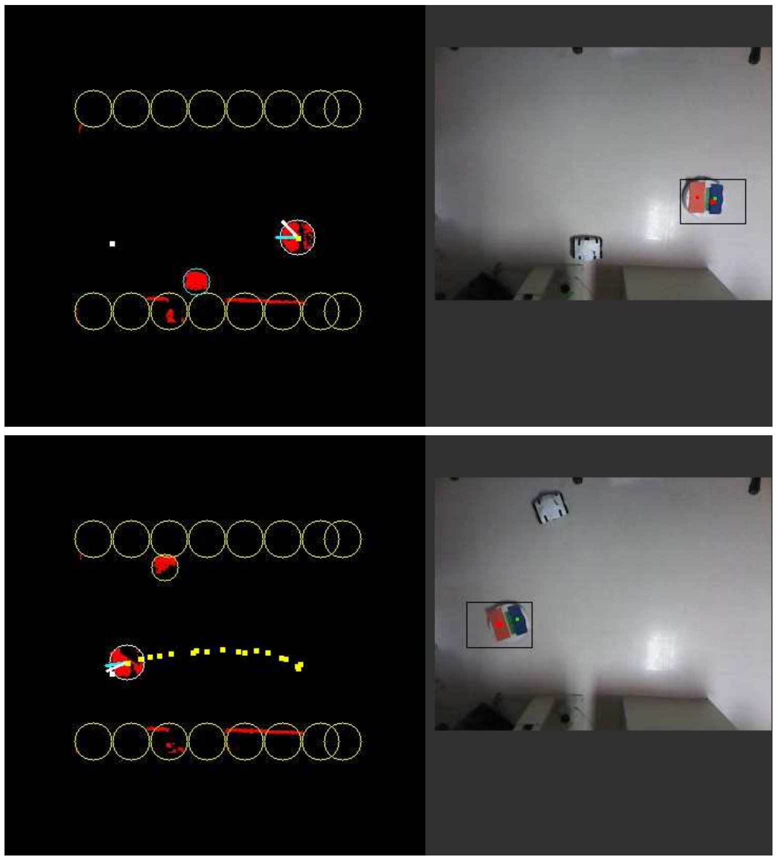

Figure 3.20: Example 2 of convergence to goal with moving obstacle with ellipse. When obstacle ellipses are used, the robot smoothly avoids the obstacle's path, as seen in the lower image. The goal position for this trial is indicated by the white dot at the left of the image, and the robot converges to goal as expected. The trail of yellow dots shows the complete robot path when elliptical information is used.

These results showcase predictive fields at work. Moreover, the normalized velocity controller proposed in the previous chapter makes it possible, through this work, to demonstrate one of the first experimental examples of classical navigation function path planning with stationary obstacles. These path planning principles lay the groundwork for the navigation component of the person following system described in the next chapter.

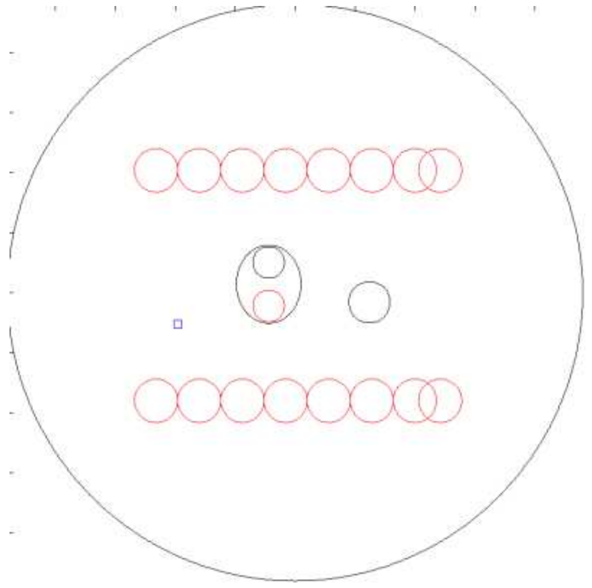

Figure 3.21: Example 2 with ellipse generated around obstacle.

Workspace information visualized using a MATLAB plot, similar to Figure 3.17.

# Chapter 4

# Person following in indoor environments

The person following system, which is the motivating application for the development of the path planner, is described in detail in this chapter. The scope of the person follower is restricted to common indoor environments such as hallways. Such a restriction may be imposed without making substantial compromises on the applicability of this person following system. For example, warehouse robots, medical robot assistants, and museum guide robots are all service robots which are expected to function in such environments.

In the initial sections of this chapter, the broad problem of ‘person following’ is discussed in greater detail. The robotic follower is supposed to interact with and serve a human leader in some capacity. Hence, human involvement is at the center of a person following system, and a leader-centric classification system is proposed. To be able to follow a leader around a practical environment, the follower should avoid confusion between its leader and other people in the scene. To address this requirement, a descriptor based leader identification method is proposed and its results demonstrated.

A robotic follower should be able to find its way to the leader in order to overcome occlusions, and it should be able to avoid obstacles in its path. Both these capabilities can only be built into the robotic system when the robot can localize itself in the environment. This person follower application assumes that the leader is within a reasonable proximity to the robot, and a comprehensive SLAM system is not required for such a task. A local map generation technique using 3D data from depth maps is proposed.

With the ability to localize itself being provided by the mapping subsystem, the actual task of navigation and obstacle avoidance is demonstrated using the predictive path planning method developed in previous chapters.

A Pioneer P3-AT mobile robot, with a software interface provided by Aria libraries, is used for the system prototype. A tripod mounted Kinect is used as the forward-looking RGB-D sensor for the robot.

## 4.1 A classification system for person following

### 4.1.1 System requirements for person followers

The functions of person following robots were first clearly outlined in the work of Yoshimi et al. [16]. Specifically, they identified that the person following robot should:

- Initialize to the leader
- Follow the leader at his/her pace
- Avoid obstacles

- Resume contact with the leader after occlusions

These tasks capture the system requirements of a person follower quite concisely. Subsequent work on person following, for example [41, 19, 34, 20], either consciously or otherwise has tended to design the system based on these person following objectives. The systemic implementation described in this chapter fits in neatly with these objectives.

These tasks are robot-specific requirements, i.e. an outline of what the robot is supposed to do when following a person. It is equally important to consider the role of the person leading the robot in such an application. In service robotics, the person is interested in having a robotic companion follow him or her around and there is no intention of putting the robot off the trail of the leader. However, a populated indoor environment poses unique challenges to the success of such an human-robot interaction. There are many situations where the leader, despite fully intending to stay within sight of the follower robot, is likely to be outside the direct line of sight of the robot's sensor.

This raises a subtle yet relevant question in terms of human robot interaction - how much is the leader required to cooperate with the robot and comply with the various limitations of the robotic follower? In future studies, it will be desirable to establish a metric for the quality of robotic followers. It is proposed that a categorization of robotic person followers based on the degree of cooperation expected from the leader will be a useful parameter for such a metric. The robotic person follower could be assigned a 'level' of sophistication based on the degree of cooperation expected from its leader. Each level can still accommodate a complex range of challenges for the robotic system, e.g. mapping, tracking, depth estimation.

Thus, this classification system for robotic person followers is relative to the level of cooperation expected from the leader. This traverses the spectrum from 'fully cooperative leader' at one end to 'independent leader' at the other.

### 4.1.2 Level 1 - Fully cooperative leader

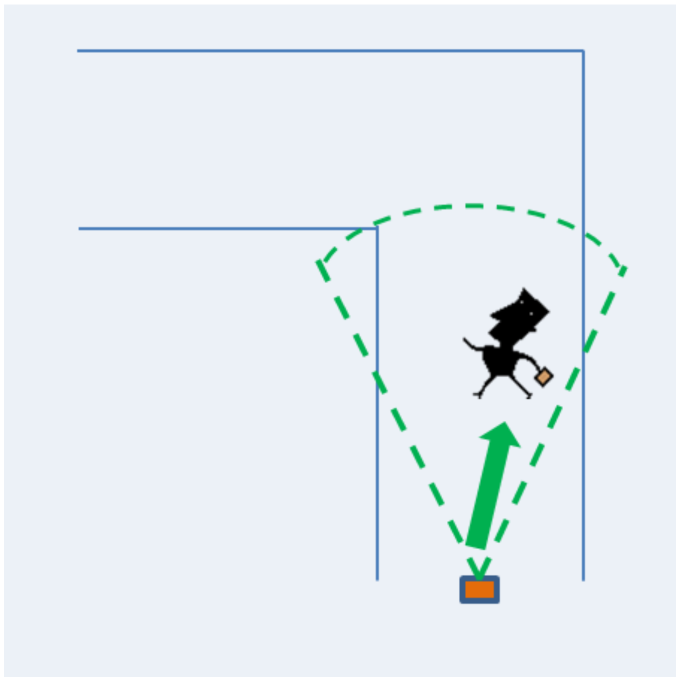

Figure 4.1: Level 1 person follower

The leader stays within the sensor range of the robot in the indoor hallway. The robot is shown using an orange rectangle and its sensing range using the dotted green sector. The leader guides the robot 'exactly', causing it to orient and move itself using the current leader position as reference. This is indicated using the green arrow.

The leader is 'fully cooperative' with the follower robot at all times. 'Fully cooperative' behavior implies that:

- The leader is aware of the physical limitations of the robot, e.g. maximum speed, sensor range, physical dimensions.
- The leader creates a path for the robot to follow exactly.

- The leader stays within sensor range of the robot.
- The leader stays detectable to the robot.
- The leader ensures that he/she is never occluded from view of the robot sensor, i.e. there are no obstacles between the leader and the robot.

This scenario is illustrated in Figure 4.1. The robot, at any given time during a trial run, turns to orient itself with the leader and translates to a desired distance relative to the leader. The leader is expected to fully guide the robot at all times and ensure that his/her path is capable of being emulated by the robotic follower. Moreover, the 'no occlusion' conditions require the leader to maintain a direct line of sight to the robot at all times.

Though this scenario is not practical for a person following service robot, it has been effectively used to test algorithms such as stereo-based depth estimation and segmentation, and human-robot interaction paradigms. An interesting feature tracking and stereo based Level-1 person follower was demonstrated by Chen [17]. Brookshire [34] used a combination of HOG features [37] and particle filtering to follow a person outdoors over a large distance and through challenges such as inclement weather. Kirby [2] introduced an interactive following paradigm where the robot used voice to communicate with the leader when the leader went out of sensor range.

### 4.1.3 Level 2 - Partially cooperative leader

The leader cooperates with the follower, but may occasionally be occluded by the environment. The straight line to the leader may also be hindered by low height stationary obstacles. Hence the term 'partially cooperative' leader. During Level-2 following:

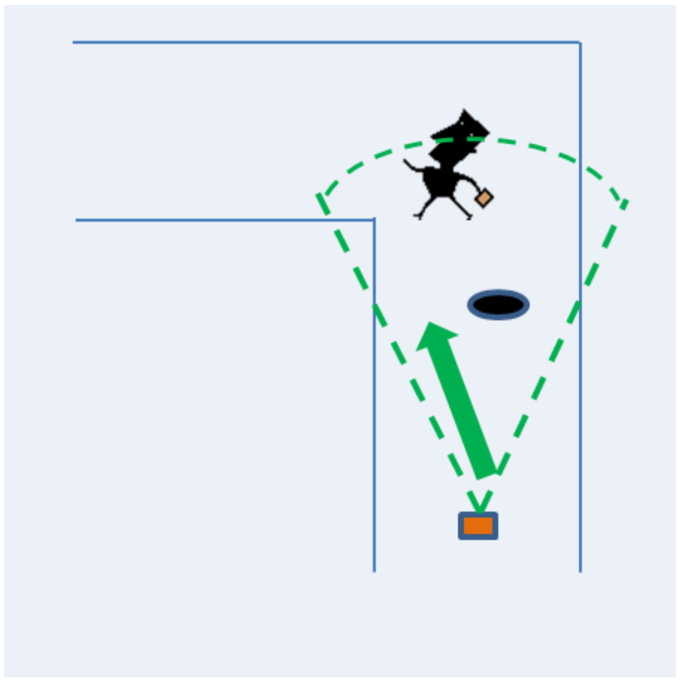

Figure 4.2: Level 2 person follower

The robot, shown using the orange box, follows the leader around stationary obstacles, such as the one shown using a black circle, by planning a path around them. If the leader strays out of sensor area, marked by green dotted lines, then the robot goes to the last observed leader position.

- The leader is aware of the physical limitations of the robot, e.g. maximum speed, sensor range, physical dimensions.
- The leader expects the robot to plan a path around stationary or environmental occlusions.
- The leader waits for the robot to overcome environmental occlusions.
- The leader ensures that stationary obstacles between him/her and the robot lie below robot eye level.
- The leader ensures that no other occlusions, e.g. other people, obstacles, come between the robot and leader.

This scenario is illustrated in Figure 4.2. Environmental occlusions are especially relevant in indoor environments such as hallways. It is very difficult for the leader to stay within sensor range and line of sight of the robot in such environments, even when there are no floor obstacles or other people in the scene. Rudimentary path planning is needed for such a situation, but it may be simplified to the extent that the robot merely needs to go to the last observed location of the leader. Once it is there, the leader is waiting for it, and cooperative behavior resumes. The last observed leader location is represented by a black ellipse in Figure 4.2. However, for the robot to confirm its location, a local map of some kind is required, to act as feedback for the robot.

The robot is expected to plan its path around low height obstacles, in which the view of the leader is never occluded from the robot. Typically, potential function based planning has been used for such situations. Yoshimi [16] demonstrates obstacle avoidance but assumes the leader is in sight of the robot during this behavior. The robot communicates with the leader on losing direct line of sight. Doisy [41] imposes a similar requirement of visibility while demonstrating obstacle avoidance.

Hence, Level 2 differs from Level 1 at the system level on two counts:

- Rudimentary path planning is required.
- Local map generation may be required.

### 4.1.4 Level 3 - Patient leader

The leader does not specifically try to account for robot limitations, occlusions, or to avoid static or moving obstacles, but waits for the robot to recover from such events. Hence the term ‘patient leader’. During Level-3 following:

- The leader expects the robot to create its own path to follow him/her.

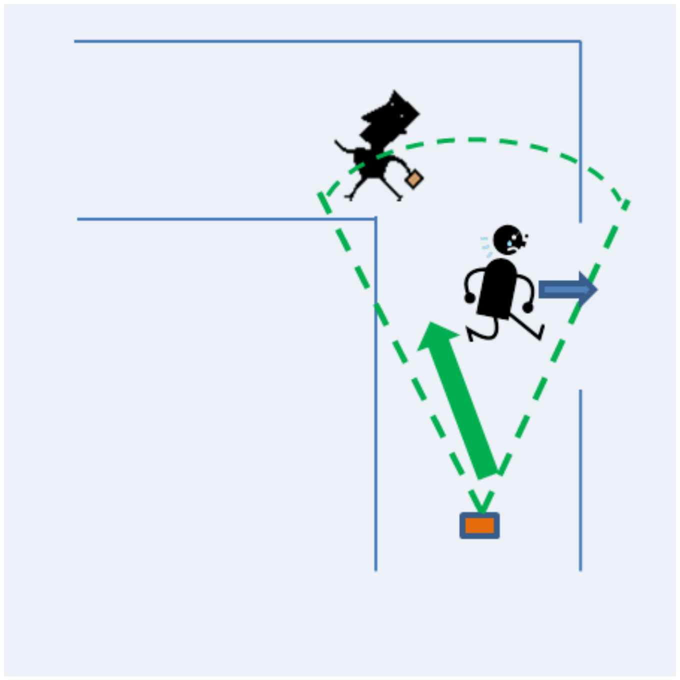

Figure 4.3: Level 3 person follower

The robot uses leader identification algorithms to recover from leader occlusions in the presence of stationary and moving obstacles. Moving obstacles are represented using the cartoon with the blue direction arrow. Leader may stray out of sensor area and expects the robot to plan a path to recover from all types of occlusions.

- The leader makes no effort to stay within sensor range.
- The leader makes no effort to avoid occlusions, e.g. other people.
- The leader waits for the robot to overcome occlusions.

The first expectation, i.e. the robot should create its own path, opens up this level to full path planning solutions. The sensing system is now challenged to detect obstacles in its field of view so that this information can be fed to the path planner for the robot to be issued motion commands. Path planning would generally require a robust local map in which the robot could be localized. In addition to this, the potential presence of other people in the scene creates a requirement for the leader to be unambiguously identified by the person follower. Leader identification is also necessary to recover after the occlusions between the leader and the robot have been removed. The system, though, has the liberty of taking a reasonable period of time to achieve these goals, since the leader is obliged to wait for the robot to handle these events before resuming his/her primary task.

The work in this chapter also falls in the category of Level 3 following. Our system complies fully with the 'patient leader' setup. Miura and Satake [19, 20], in separate papers, show the use of an EKF based tracking algorithm for tracking a leader through occlusions.

Level 3 differs from Level 2 at the system level in the following ways:

- Tracking leader through occlusions or leader identification methods are required.
- Full path planning may be required to handle a dynamic environment where obstacles are moving.

### 4.1.5 Level 4 - Independent leader

The leader does not wait for the robot to overcome occlusions, and assumes that the robot can catch up with him/her. Hence ther tem 'independent leader'. During Level 4 following:

- The leader expects the robot to create its own path to follow him/her.
- The leader makes no effort to stay within sensor range.
- The leader makes no effort to avoid occlusions, e.g. other people.
- The leader does not wait for the robot to overcome occlusion events.
- The leader expects the robot to communicate distress if lost.

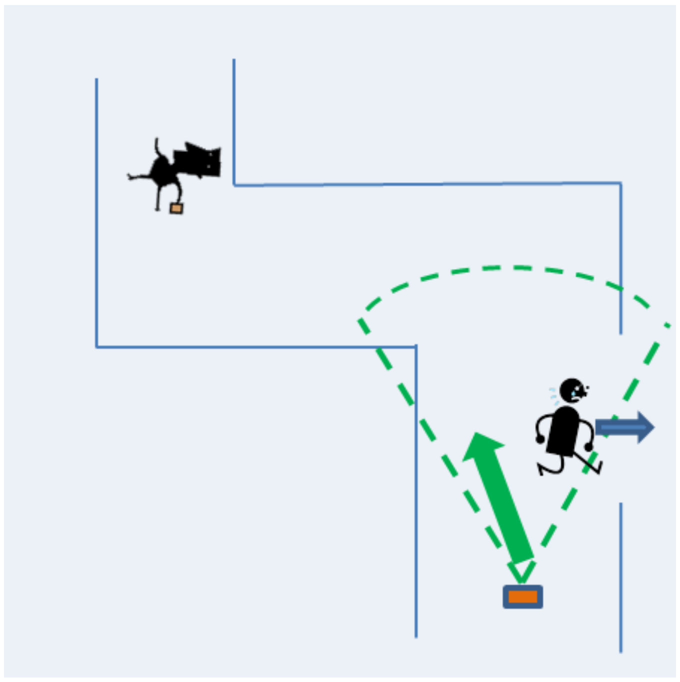

Figure 4.4: Level 4 person follower

The robot uses a complete map of its indoor environment to recover its independent leader, since the leader is not expected to wait for the robot. Leader identification algorithms are used to plan safe paths around stationary and moving obstacles. Moving obstacles are represented using the cartoon with the blue direction arrow. Robot is required to establish some form of direct communication with the leader to recover from a complete loss of the person's track.

The expectations from Level 4 following are that the robot is physically capable of keeping pace with its leader. Failing this, the robot should be capable of exploring the area (using a preloaded or online map) in search of the leader. Failing even this, the robot should be able to communicate its 'lost' status to the leader and be able to recover on receiving instructions or leader location in some form. Except for the 'lost' status, this setup does not assign any responsibility to the human leader in a person following situation.

In terms of robots serving in practical environments, such a system is least intrusive to its environment and allows the leader to perform his/her tasks freely without having to continuously check whether the robot has kept pace. A Level 4 system has currently not been completely realized. Gross [11] and Weinrich [36, 35] et al. demonstrate an interesting system for socially assistive robots to help the elderly but do not discuss its ability to plan paths in a dynamic environment with moving obstacles. Kirby [2] proposes interaction with the human when the robot is lost, but the condition for being 'lost' is limited to the leader moving out of sensor range. This is severely limiting for indoor navigation, as discussed earlier.

Level 4 differs from Level 3 at the system level in the following ways:

- A complete mapping solution is required.
- Sophisticated human-robot interaction is required to recover from distress situations.

In summary, the proposed classification system describes person following in terms of the expectations from the leader. Such a classification system allows roboticists working within each level to focus on useful subsystems such as mapping and estimation, while freeing them from the expectation of presenting a complete system. At the same time, it allows the human working with the robot to know exactly when active 'leadership' is required for the interaction to be fruitful. Presumably, commercial versions of service robots could supply information about the robot capabilities in terms of the leader using a system similar to the one proposed here.

With this in mind, the remaining sections of this chapter focus on the development and implementation of techniques for the proposed Level 3 follower.

## 4.2 Leader tracking using color descriptors

An important module for a Level-3 person following robot is its ability to track the leader through occlusions. The solution proposed here combines the strengths of the Microsoft Kinect skeletal tracker with a color descriptor generated using a combination of two colorspaces: HSI and L*a*b* (CIE 1976). The former provides a temporal tracking output based on depth data from the Kinect RGB-D sensor. The latter is used when the temporal track of a skeleton has been lost, i.e. the person has been occluded. The Kinect skeletal tracker's features are explained in the Section 4.2.1, followed by an explanation of the appearance based descriptor which makes it possible to track the leader through short and long term occlusions. Results for this subsystem are provided at the end of this section.

### 4.2.1 Kinect skeletal tracking

Following the commercial release of the Microsoft Kinect [89], Microsoft released a SDK [90] to allow programmers and researchers to interface with this RGB-D sensor. Function calls from the Kinect SDK have since been integrated into the computer vision library Blepo, which has been used for this software implementation of the person follower. The Kinect SDK contains an implementation of the skeletal tracker. This algorithm, first proposed in [31], uses depth information to predict the position of 3D body parts. The skeletal tracker has the ability to keep track of up to six people (skeletons) in the field of view of the Kinect camera.

A skeleton is defined by the algorithm as a configuration consisting of 20 joints and 19 bones. The joints and bones which comprise the Kinect skeleton are shown in Figure 4.5. Information about the skeletons is stored in a data structure. Relevant information stored per skeleton is as follows:

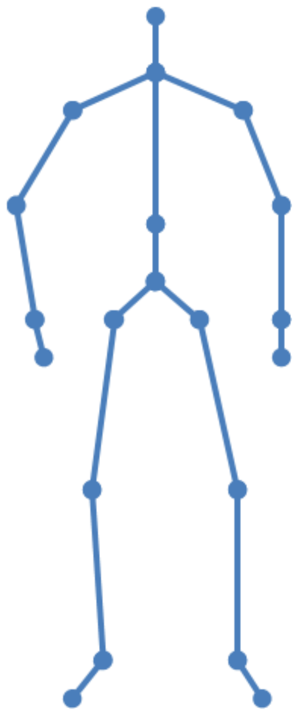

Figure 4.5: Skeletal representation in the Kinect SDK

Dots indicate the positions of joints on the Kinect skeleton. Lines connecting joints are the bones. Up to 19 bones and 20 joints can be tracked.

- Tracking status of the skeleton
- Mean position of the skeleton (3D was well as image coordinates)
- Tracking status of the joint (tracked/ inferred/ not tracked)
- Position of a specific joint (3D as well as image coordinates)

The Kinect skeletal tracker works as follows: depth and 3D information is used to identify up to 6 persons in the field of view at any given time. The tracker maintains the identity of a person as long as there is no occlusion. In the absence of occlusion, the skeletal ID assigned to a person remains unchanged. However, if a person is occluded and reappears, then this registers in the tracker algorithm as a ‘new’ skeleton, i.e. the person’s identity is not maintained. This behavior motivates creating a person identification framework which builds upon the reliable non-occlusion tracking of the Kinect SDK skeletal tracker and adds descriptor-based identification for tracking through occlusions.

The various skeletal variables listed above are used in creating a descriptor representation of the leader and other people in the field of view of the sensor. The descriptors help tell the leader and other people apart and the robot can then follow a leader through various types of occlusions.

### 4.2.2 Descriptor generation

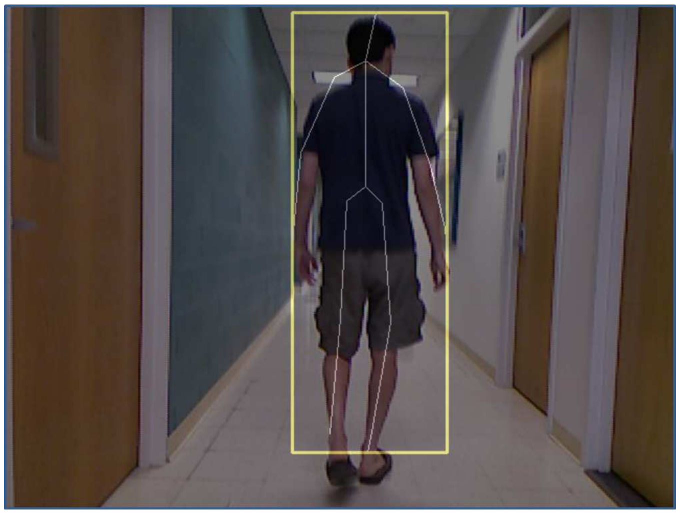

Figure 4.6: Skeletal outline overlaid on RGB image

Though the Kinect skeletal tracker has been used in applications such as performance evaluation [91] and gesture recognition [92, 93], its output has not been used to build a person identification system. Such a system, which helps the robot recover from leader occlusion, is proposed. The central idea is to take information about the locations of joints and use this information to identify bone positions and lengths. Then, color information from image patches along the central line of each bone is collected into a descriptor. The Kinect tracker identifies the location of 20 joints, hence 19 bones can be identified. Four color values are calculated per bone, to yield a descriptor of $19 \times 4 = 76$ elements. Descriptors are matched using Euclidean distance and an empirically observed threshold is used to classify the observed descriptor as leader or otherwise.

The color information extracted per bone are the chromaticity components of the HSI and CIE L*a*b* color space. Both color spaces separate the color component from luminosity or brightness, which makes them more robust to lighting changes such as variance in indoor illumination and shadows.

HSI (Hue-Saturation-Intensity) is a cylindrical color space, whose conversion from RGB is specified in [94] as:

$$\begin{aligned} H &= \cos^{-1}\frac{0.5\cdot(R-G)+(R-B)}{\sqrt{(R-G)^2+(R-B)(G-B)}} \\ S &= 1-\left(\frac{3}{R+G+B}\right)\cdot\min(R,G,B) \\ I &= \frac{R+G+B}{3} \end{aligned}$$

In HSI, 'I' is the intensity component which is discarded when the person-specific descriptor is being formulated.

The CIE L*a*b* (also known as CIE 1976) color space derives from the CIE XYZ (CIE 1931) color space and was designed to mimic the response of the human eye to color. L* is the luminosity component, which is discarded when the descriptor is formed. Conversion from RGB to L*a*b* is a two step process, comprising of conversion from RGB to XYZ and from XYZ to LAB. Formulae for the two conversions are given here [95]. RGB is first converted to XYZ using [96]:

$$\begin{aligned}
X &= 0.4124 \cdot R + 0.3576 \cdot G + 0.1805 \cdot B \\
Y &= 0.2126 \cdot R + 0.7152 \cdot G + 0.0722 \cdot B \\
Z &= 0.0193 \cdot R + 0.1192 \cdot G + 0.9505 \cdot B
\end{aligned}$$

XYZ values are then converted to L*a*b* values using

$$\begin{aligned}
L^* &= \begin{cases} 116 \cdot (Y/Y_n)^{\frac{1}{3}} - 16 & \text{for}(Y/Y_n) > 0.008856 \\ 903.3 \cdot (Y/Y_n) & \text{otherwise} \end{cases} \\
a^* &= 500 \cdot (f(X/X_n) - f(Y/Y_n)) \\
b^* &= 200 \cdot (f(Y/Y_n) - f(Z/Z_n))
\end{aligned}$$

where

$$f(t) = \begin{cases} t^{\frac{1}{3}} & \text{for } t > 0.08856 \\ 7.787 \cdot t + 16/116 & \text{otherwise} \end{cases}$$

and where $X_n = Y_n = Z_n = \frac{1}{3}$ is the tristimulus point (white) of the XYZ color space.

To extract HSI and L*a*b* components to form a skeletal descriptor, the end points of a bone in the RGB image are considered. If the corresponding depth values for these points lie within an acceptable range of the average depth of the person (returned by the skeletal tracker), then the color extraction step is carried out; otherwise, color values for that bone are all set to $-1$. The latter is used to indicate that the tracked bone position may lie outside the actual outline of the person. In Figure 4.6, an example of well and poorly detected bone positions is seen. The observed misalignment clearly motivates this filtering step.

For bones which have been tracked well, image patches which align with the orientations of these bones are extracted. An example of this is shown in Figure 4.7.

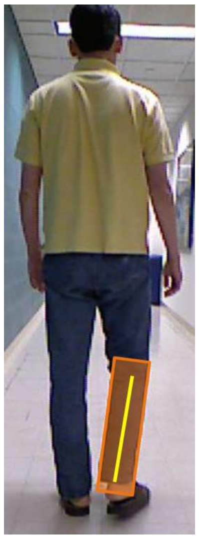

Figure 4.7: Bone patch extracted from the skeletal outline.

Yellow line indicates the detected bone. The orange box around it is the bone area. This rectangle is rotated such that its length aligns with the bone orientation. RGB data is converted to HSI and L*a*b* to create a 4 element descriptor for the bone. Descriptors for each of the 19 bones are collated to form the 76 element person descriptor.

For each such image patch, the medians of Hue, Saturation, a*, and b* are computed, normalized, and scaled to the range $0 \ldots 255$. These four values are the contributions of the bone to the skeletal descriptor. Therefore, the descriptor for the $n^{th}$ skeleton is a 76 element vector,

$$D_n = [\ H_1 \quad S_1 \quad a_1^* \quad b_1^* \quad \ldots \quad H_{19} \quad S_{19} \quad a_{19}^* \quad b_{19}^*\ ]$$

.

### 4.2.3 Tracking leader for an unoccluded case

During initialization, the leader descriptor $D^0_{leader}$ is generated. For each subsequent frame, descriptors are generated for each skeleton tracked by the Kinect skeletal tracker. For the $i^{th}$ skeleton in the $j^{th}$ frame, let the skeleton be represented by $D_i^j$.

Each skeleton's descriptor is compared to the leader descriptor using the Euclidean distance to yield the comparison score,

$$S_{i,leader}^{j} = \left\| D_{leader}^{0} - D_{i}^{j} \right\| . \tag{4.1}$$

Since Euclidean distance is being used, lower scores indicate a closer match with the leader descriptor. The threshold for a skeleton to be considered a match to the leader is set at an empirically chosen value of $S_{max}$. Any score above $S_{max}$ is automatically eliminated from the list of leader candidates for that particular frame.

The Kinect skeletal tracker updates the skeleton's position and other properties during each frame. Thus, from the time a leader is initialized up to the time he/she is occluded, the Kinect skeletal tracker should be expected to return a reliable track of the person and, potentially, descriptor matching should not be needed. However, during experimental trials, sporadic frames were observed where a skeleton was being 'tracked' to a position which corresponded to a door or some other non-person feature in the environment. In such a situation, the person following system is expected to recognize a glitch in the tracker and respond accordingly. For this reason, the tracked leader skeleton's descriptor is checked for its matching score using Eq. 4.1 during each frame. Thus, the descriptor matching technique is used during an unoccluded trial to interpret a failure in the skeletal tracker.

The temporal continuity maintained by the Kinect skeletal tracker is also useful when another person wearing clothes similar to the leader walks past the leader. Since the algorithm checks only for the match score between the initial leader descriptor and the current descriptor corresponding to the leader skeleton, another person wearing the same clothes does not throw the system off course *as long as there is no occlusion.*

### 4.2.4 Detecting occlusions and leader reappearance

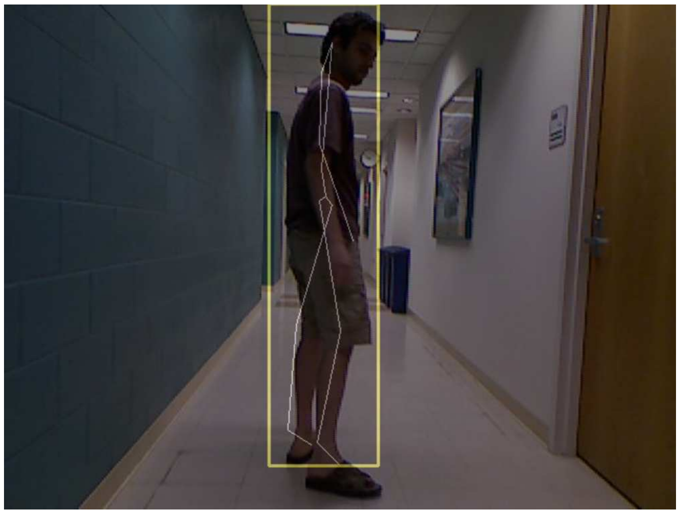

Figure 4.8: Example of self-occlusion

When the person turns, skeletal information is overlaid poorly, and descriptor is adversely affected by this misalignment. Thus, turning or 'self-occlusion' needs to be avoided by the descriptor matching algorithm.

The descriptor matching algorithm is most useful in leader reidentification after the occlusion has been removed, i.e. when the leader reappears. As explained in Section 4.2.1, the Kinect skeletal tracker cannot reestablish leader identity when a leader has reappeared after an occluding event. Occluding events can be categorized as follows:

- Self-occlusion: Leader turns while fully in view of the Kinect
- Sensor occlusion: Leader moves out of of the field of view of the Kinect
- Obstacle or person occlusion: Other people or objects in the field of view occlude the leader

Of these items, the first, i.e. self-occlusion, is a special event based on the descriptor generation method. The Kinect skeletal tracker maintains track of the leader when the leader is turning. However, as explained in the previous section, sporadic tracking errors by the Kinect SDK are being avoided by comparing the current leader descriptor $D^j_{leader}$ to the initialized leader descriptor $D^0_{leader}$. As seen in Figure 4.8, however, the pose of the skeleton is often poorly estimated when the leader is turning. Hence, the extracted bone patches are poorly aligned with the actual positions of bones. This can lead to a very poor match score between $D^j_{leader}$ and $D^0_{leader}$. It is necessary to prevent this score from leading to the inference that the leader is either lost or occluded by another person.

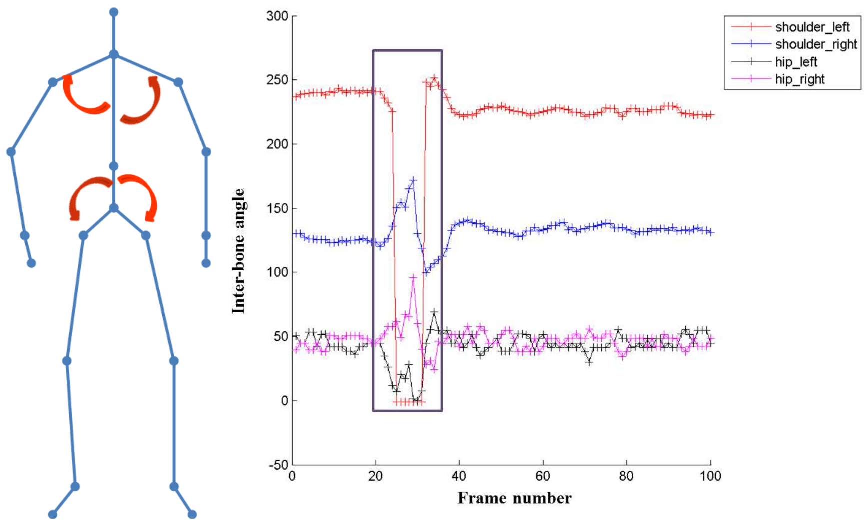

Figure 4.9: Using bone angles to infer self-occlusion.

As a person turns, the four bone angles indicated using red arrows in the left image, show sharp deviations from their normal values, as highlighted by the purple box in the right image. Thus, initializing bone angles and comparing them against a deviation threshold allows the system to infer self-occlusion.

To remedy this, self-occlusion is inferred and the descriptor matching is 'turned off' until self-occlusion has terminated, i.e. leader no longer has a profile view as seen from the Kinect. It was found that four angles between bones, indicated in Figure 4.9 were good indicators for detecting when the leader was turning. The graph to the right in the figure shows the variation in these angles for a trial where the leader turned once. The purple box shows the frames where the leader turned 180°. These frames clearly coincide with the widest variation in bone angle values. This type of trend was consistently observed during trials, and the indicated bone angles are computed and checked for being within bounds during each frame to help the system overcome leader self-occlusion.

The other two types of occlusion, sensor and person occlusion, are dealt with using a common descriptor-based mechanism. They are inferred when the skeletal tracker registers the initialized leader skeleton ID as being 'not tracked'. When this event occurs, the algorithm begins to compare all tracked person descriptors with the original leader descriptor $D^0_{leader}$. This process continues over multiple frames until the one of the descriptors satisfies the threshold $S_{max}$. At this point, the occlusion is inferred to have been removed. The skeletal ID of the closely matching descriptor is assigned as the new leader ID, and the reference leader descriptor is updated to $D^0_{leader} = D^n_{leader}$, where the current frame number is $n$.

It may be argued that temporal tracks of the leader could also be used to achieve recovery through occlusions. This approach is tenable and has been used in [19, 20]. But the problem with such approaches, despite their reliance on sophisticated motion models, is that they are not guaranteed to succeed over long term occlusions. This is especially true for tracking a person, since there may be arbitrary direction and position changes during the period of the occlusion. Using an appearance based method such as descriptors frees the algorithm from having to generate a reliable and robust filtering output.

Having motivated and explained the descriptor algorithm, its performance is evaluated in the next section.

### 4.2.5 Performance of the tracking algorithm

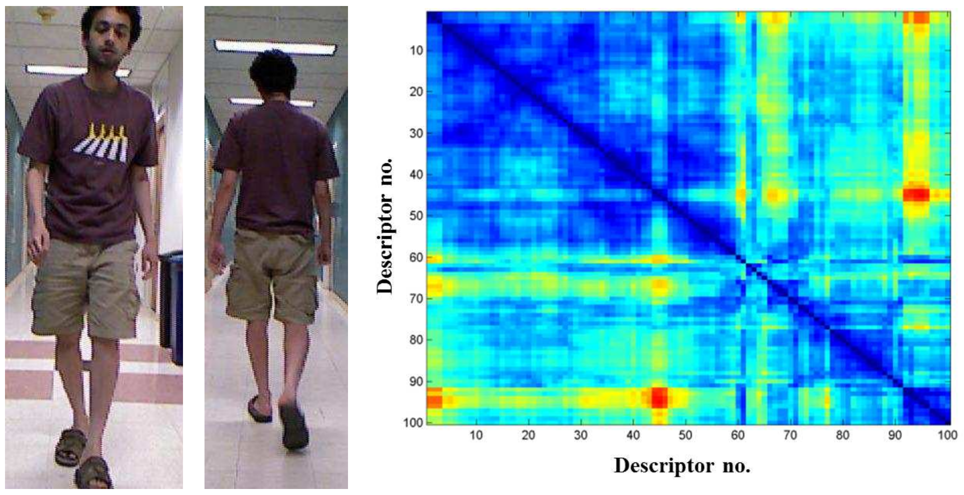

Figure 4.10: Comparison of descriptors from same trial

Descriptors from the same person over 100 frames of a trial are compared. Each cell of the $100 \times 100$ grid shows the comparison score using a color code, in which blue areas are favorable comparisons and red areas are poor comparisons. As expected, descriptors from the same person match each other well, except for orange-red bands in the image, which is where the person is turning.

The appearance based leader identification algorithm explained in the previous section may be declared a success if:

- Comparing the initialized leader descriptor $D^0_{leader}$ with the leader descriptor $D^j_{leader}$ in the $j^{th}$ frame returns a low Euclidean distance.
- Comparing $D^0_{leader}$ with a non-leader descriptors $D^j_i$ returns higher Euclidean distances.

In Figure 4.10, a comparison of leader descriptors from the same trial can be seen. The two images on the left side of this figure are the initial frame and an intermediate frame respectively. The 'heat map' on the right shows the Euclidean distance, scaled from blue regions being the best score and red regions being the worst. The reddish areas are frames where the leader was turning; as explained in the previous section, no occlusion inference is made during these frames. The horizontal and vertical axes are both frame numbers from the trial.

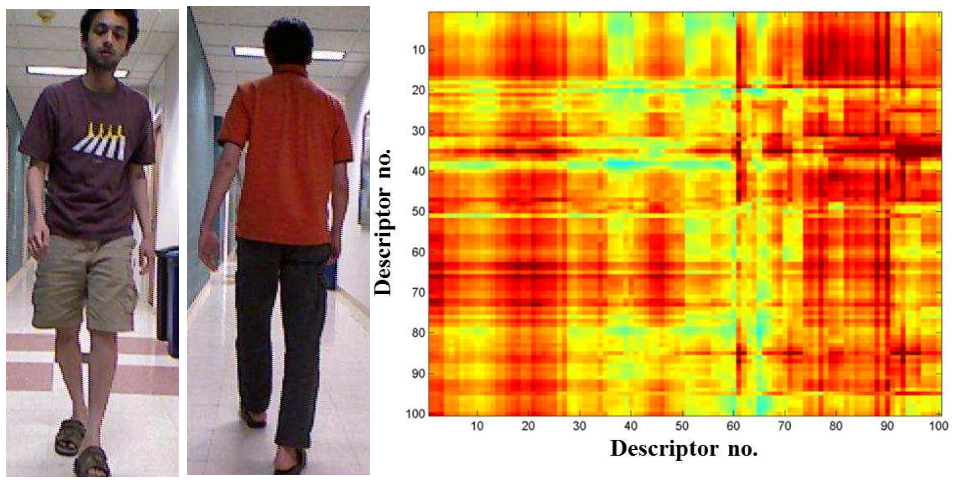

Figure 4.11: Comparison of descriptors from different trials

Descriptors from two different trials, using 100 frames each, are compared. Each cell of the 100 × 100 grid shows the comparison score, in which blue areas are favorable comparisons and red areas are poor comparisons. As expected, descriptors two trials match each other poorly, since the person is wearing different clothes in each.

The heat map helps visualize the performance of the descriptor generation and matching method when dissimilar descriptors are being compared. See Figure 4.11, in which the heat map is scaled to the same limits as Figure 4.10. In this dataset, leader descriptors generated during one trial were compared to leader descriptors from a different trial. As can be seen in the images on the left of the figure, the clothing worn by the leader in these trials is different. The heat map on the right shows that the descriptors are dissimilar, evidenced by the red regions on the map.

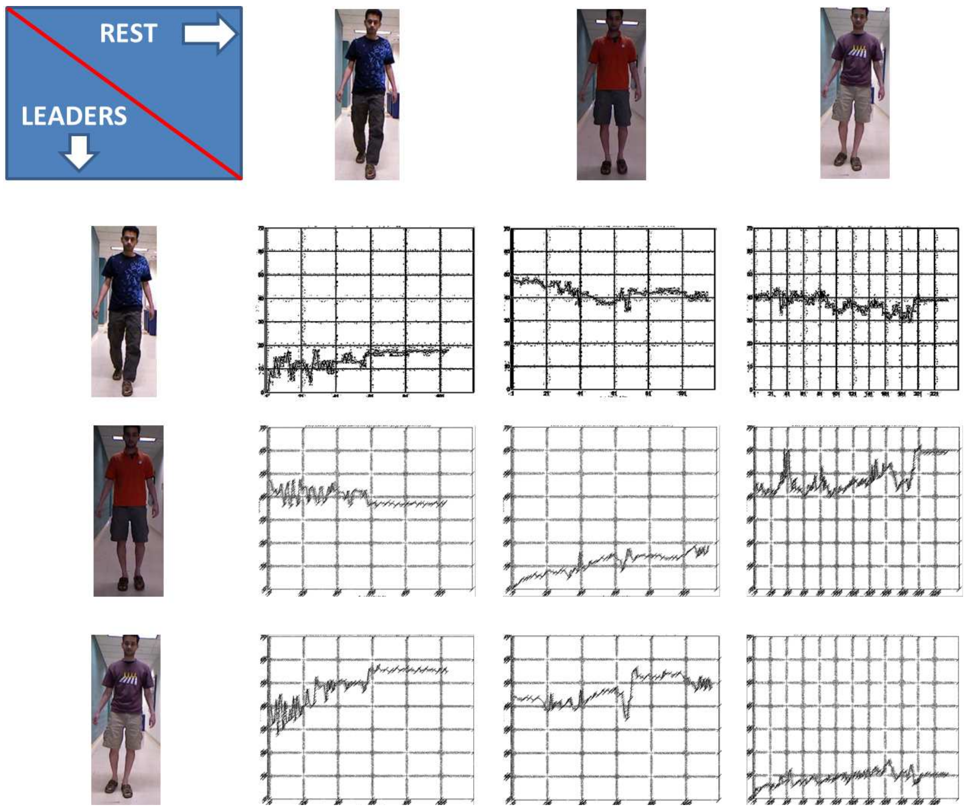

Figure 4.12: Tabulated results from leader-non leader comparisons

In each cell, the row image is the leader, against which all test descriptors of the trial corresponding to the column image are compared. The $x$ axis is frame number and $y$ axis is comparison score. Lower the score, better the match between the leader and the test descriptor. As expected, test descriptors from the same trial as the leader (graphs along the diagonal) show low comparison scores. Off-diagonal graphs show higher comparison scores since the color of clothes being worn by the person has changed.

In Figure 4.12, a tabulated form of results similar to Figures 4.10 and 4.11. The image to the left of every row of the table in the figure is leader for that trial. So, the table can be interpreted as follows:

- Cell $(x, y)$ shows the initial leader descriptor from trial $y$ being compared to all descriptors from trial $x$.
- When $x = y$, cell $(x, y)$, shows the initial descriptor from a trial being compared to all descriptors from the same trial.

- Thus, when the leader appearance changes between trials, $x = y$ should result in a graph with low values and $x \neq y$ should result in a graph with high Euclidean distance values.

These trends are clearly visible in the figure. These and other trials motivate an empirical threshold of $S_{max} = 30$ for the match score. To reiterate the significance of this threshold, since the score signifies Euclidean distances, any score above the threshold implies that the descriptor is too far (in the 76-D descriptor space) to be considered a match.

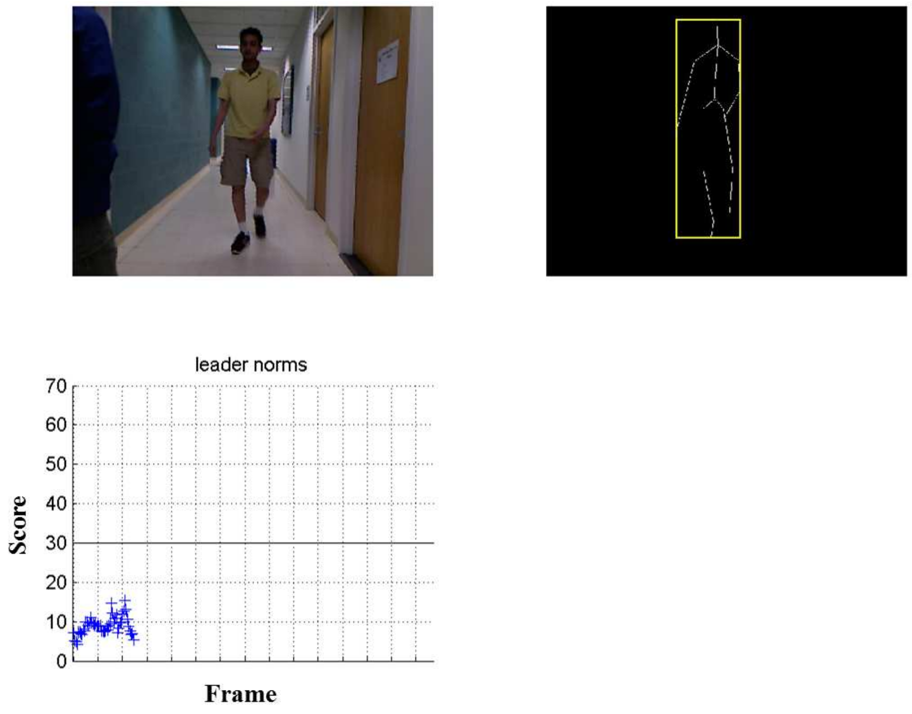

Figure 4.13: Leader tracking before occlusion.

The $y$ axis on the plot to the bottom left shows that the comparison score is low when the leader is being tracked and unoccluded, as shown by the yellow border around the skeleton in the top right image. Blue marks and lines on this plot show the trend of the comparison score.

Figures 4.13, 4.14, and 4.15 demonstrate the ability of the described algorithm to recover from leader occlusion. A typical trial for occlusion recovery begins with

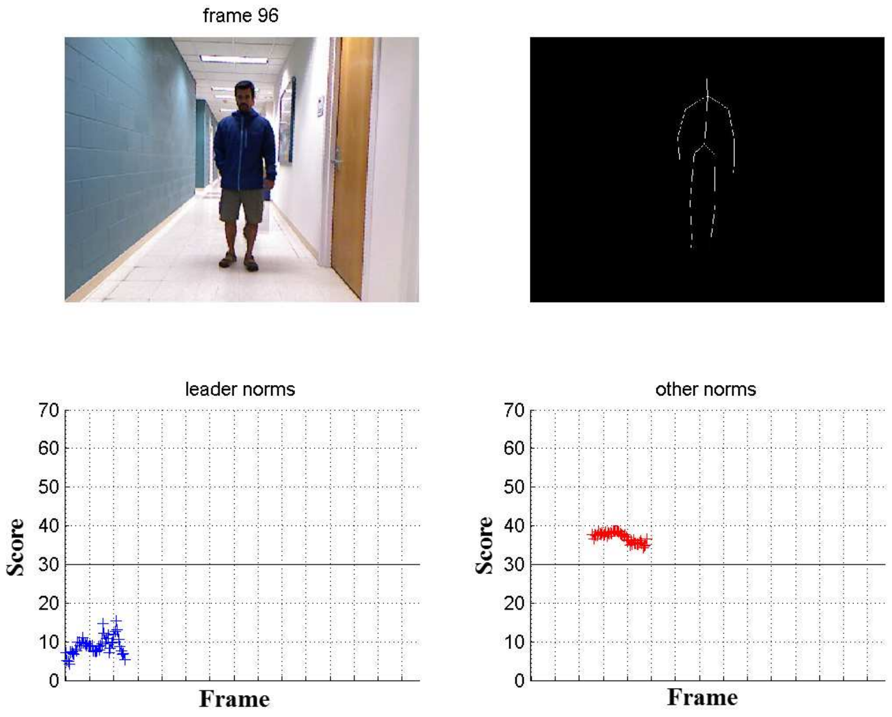

Figure 4.14: Detected occlusion.

The $y$ axis on the plot to the bottom right shows that a non-leader skeleton has been detected, as evidenced by the high comparison scores shown by red marks and connecting lines. An occlusion has been detected, as shown by the lack of the yellow 'leader' border around the skeleton in the top right image. Blue marks and lines on the leader plot to the bottom left remain unchanged from Figure 4.13 since the leader is not visible.

the leader being initialized and leader descriptor being generated. The plot at the bottom left of each of the figures shows the comparison score of the current leader descriptor with the initialized leader descriptor. As seen in Figure 4.13, these values are typically well below the threshold of $S_{max} = 30$.

When another person occludes the leader, as seen in Figure 4.13, the Kinect skeletal tracker tags the leader skeleton ID as being 'not tracked'. The algorithm now switches to its leader recovery phase, in which all detected skeletons are compared with the initialized leader descriptor. If the match between a detected skeleton descriptor and the leader descriptor is above the threshold, then the skeleton is rejected as a

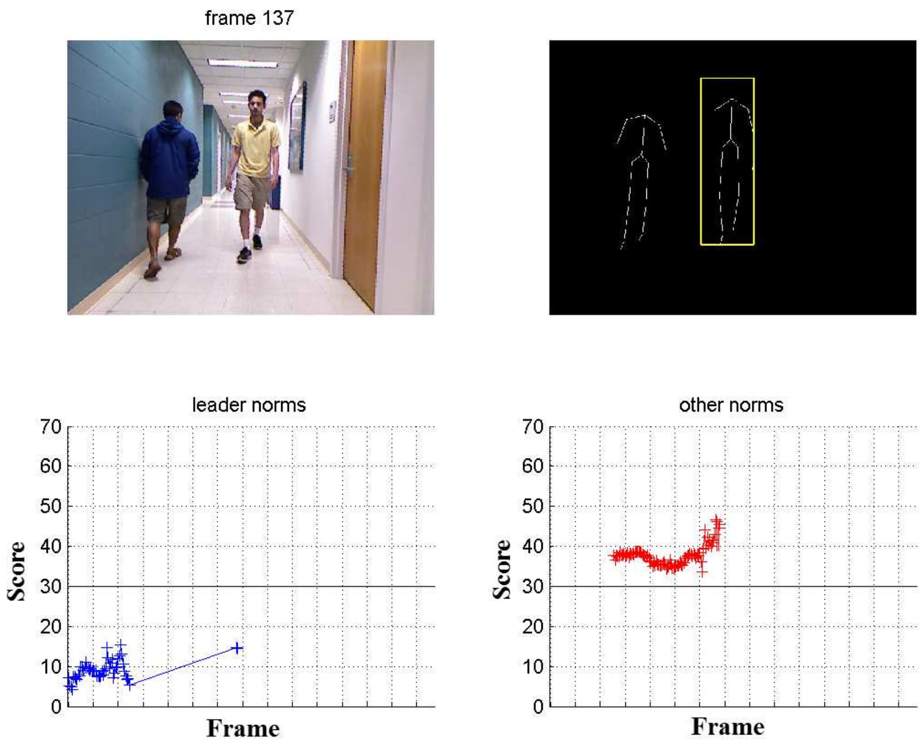

Figure 4.15: Leader recovery after occusion.

The leader is recovered from the occlusion in Figure 4.14, as shown by the reappearance of a blue mark and connecting line on the leader plot on the bottom left. The $y$ axis on the plot to the bottom right shows that the non-leader skeleton consistently returned high comparison scores, as evidenced by red marks and connecting lines.

possible reappearance of the leader after occlusion. Figure 4.14 shows this occlusion detection mechanism at work. The plot at the bottom right of this figure shows comparison scores for inferred non-leader skeletons. It can be seen that the values are consistently above the threshold for a number of frames in which the occluding skeleton is being detected by the skeletal tracker.

Figure 4.15 demonstrates occlusion recovery at work. After a number of frames, the leader reappears in the field of view. During this frame, both the leader and the occluding skeleton are detected. The algorithm compares both skeletal descriptors to the initialized leader descriptor and finds that the reappeared leader's descriptor matches the initial descriptor to well below the threshold. The skeleton which satisfies this condition is then tagged as the reappeared leader for the person follower.

In all figures, the yellow box is indicative of the skeleton which is being detected as the leader. Thus, this data demonstrates the effectiveness of the appearance based descriptor in occlusion detection and recovery.

With this module in place, the next task for the person follower is to map its environment locally, so that robot control and path planning can be implemented when required.

## 4.3 Mapping the indoor environment

The indoor environment presents challenges for the use of conventional mapping cues such as feature tracking and point clouds. In Section 4.3.1, these challenges are discussed in detail. The proposed solution which overcomes such problems is the use of a combination of Manhattan rotations and dead reckoning for translations. To be able to build a map of the local environment using these techniques, it is necessary to generate a representation of the field of view of the Kinect in each frame. Floor segmentation, followed by occupancy map generation, and finally a scan generation step helps represent 3-D data in a manner useful to the RANSAC algorithm, which is at the heart of Manhattan estimation. All these steps are explained and their results demonstrated in this section on mapping.

### 4.3.1 Limitations of conventional odometry techniques

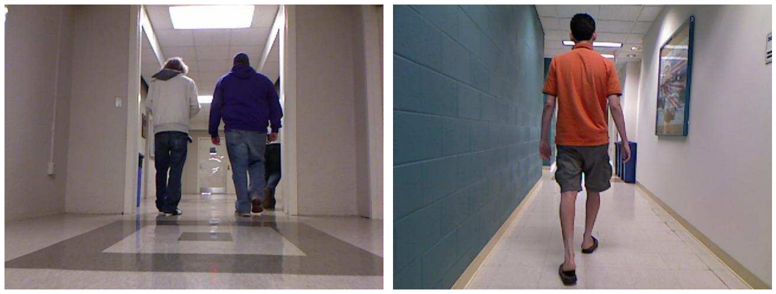

Figure 4.16: Typical hallways for person following.

To map the robot's local workspace, an online mapping technique which works well for indoor environments is required. Visual odometry [53, 54] is one such technique. Visual odometry relies on detecting and tracking features reliably to be able to estimate inter-frame pixel correspondences. Feature tracking techniques such as SIFT [97], SURF [98], joint KLT [99], and BRISK [100] may be used to estimate feature correspondences. The advantage of using a RGB-D sensor is that it is easily possible to get 3-D values from pixel data, since the sensor is calibrated and depth values are known. The 3-D points corresponding to feature pixel values can then be used to estimate the inter-frame transformation between them, using estimation methods such as sparse ICP (Iterative Closest Point) [56] or 3-D least squares [55]. Inter-frame transformations are used, frame-by-frame, to compose a map of the environment.

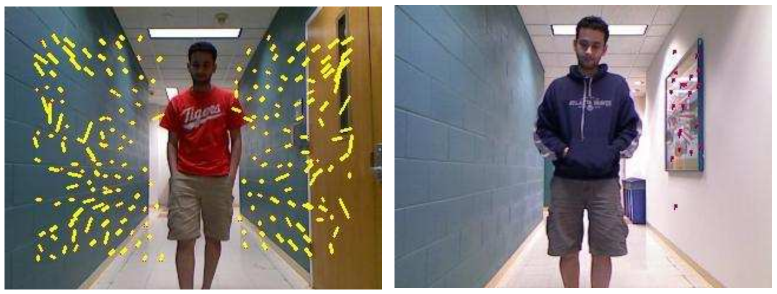

Figure 4.17: Poor results from feature tracking.

The image to the left shows a frame where a number of features have been tracked poorly. The image to the right shows a frame where too few features are detected to make a good inter-frame transformation estimate for map-building.

The major challenge for this technique is that indoor hallways are not typically feature-rich, e.g. Figure 4.16. This frequently results in poor tracking, as seen in Figure 4.17 in the image to the left, or results in an inadequate number of features being estimated, as seen in the image to the right in the same figure. In addition to the quality of tracking, not all visually matched features have corresponding depth values due to the limited sensor range of the Kinect. Thus, visual odometry tends to be unreliable in typical hallways.

An alternative to using visual odometry is the use of techniques which use 2-D or 3-D Euclidean data directly for estimating inter-frame transformations. Perhaps the most popular 3-D estimation techniques is Iterative Closest Point or ICP [56]. ICP operates on 3-D point cloud data, and has been implemented in the versatile

Point Cloud Library (PCL) [101] and the stand-alone library LibICP[102]. Spatial configuration of point clouds can be exploited to find 3-D features in the data, an approach outlined in Fast Point Feature Histograms (FPFH) [103]. Scan matching [57, 58] is a 2-D technique in which the plan view of the floor is generated (usually using range scanners) and two such views are matched using iterative techniques which minimize an error function. The output of all of these depth-based methods is an estimate of rotation and translation between frames.

However, the problem with using depth-based methods is very similar to that in using visual odometry: namely, the absence of depth 'features' which can be be useful in estimating the inter-frame transformation. The limitation is especially severe when it comes to inferring translations, since the robot is moving between two parallel walls and successive scans or 3-D point clouds are very similar to each other in such environments. This makes it very difficult for any algorithm to tell apart genuine, usable variations in the hallway data (such as lintels) from sensor noise, and this exacerbates the quality of the transformation estimate.

See Figure 4.18 for an example of a poor depth-based estimate. The two stacked images to the left in this figure show the raw data being processed by the Diosi's scan matching algorithm [57]. The map to the right shows that the data from these frames has been stitched together with considerable drift.

Although a combination of visual odometry and scan matching provided occasional sequences of frames where the map was of acceptable quality, a recurring observation was that of frames such as the one in Figure 4.18, which would throw the map completely off course. The precautionary measure in map building was to reset the map when large rotations or translations were detected; however, this inconsistency was undesirable since the map was to be ultimately used by the path planner.

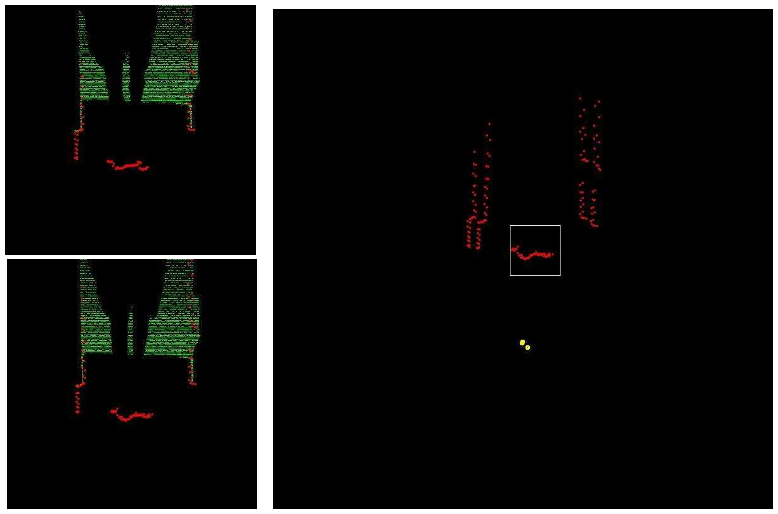
Figure 4.18: Poor results from scan matching.

Top and bottom images on the left are successive scan images. Scan matching correctly estimates rotation, as shown in the map on the right, but translation is incorrectly estimated, as evidenced by a rightward shift in the scan points during map building.

Thus, to cope with these limitations of the above cited techniques, an approach which combined Manhattan assumptions with dead reckoning was developed. The first few steps in this approach is generating a useful representation of sensor data, which is explained next.

### 4.3.2 Generation of occupancy maps

The name 'occupancy maps' refers to a bird's-eye view of the field of view of the Kinect generated using the floor plane equation and current depth data. The concept of occupancy maps was first introduced by Moravec and Elfes [104]. The floor plane is assumed to have been calibrated before a trial using the standard equation

$$z = ax + by + c$$

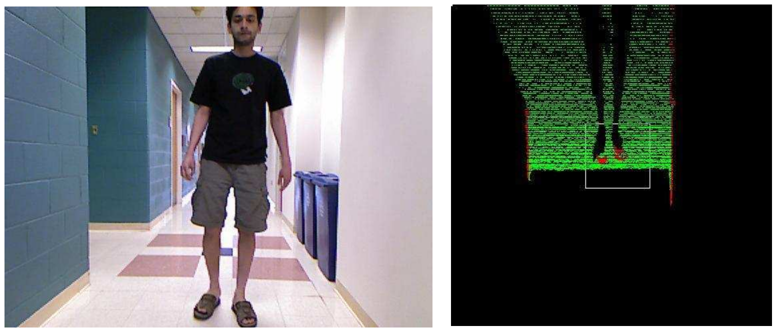

Figure 4.19: Generation of occupancy map from Kinect data

Green areas in the image on the right are floor points. Red areas are non-floor, or 'occupied' points. This deduced overhead view shows the person in the middle of the occupancy image surrounded by a white border. The bounding box ensures that red pixels on the person are not used for estimating wall locations.

where $a$,$b$,$c$ are parameters of the plane. Calibrating the floor plane is a simple, single time procedure detailed in a previous chapter and highlighted using Equations 3.1 and 3.3. The floor plane threshold $\epsilon_{floor}$ is set to a relative tolerant value of 3.5 for our trials, to ensure that none of the floor (unoccupied) pixels are mislabeled.

All of the $320 \times 240$ depth values from the Kinect camera are transformed to 3D coordinates, and tested for a fit to the floor plane equation within the threshold $\epsilon_{floor}$. In Figure 4.19, the image on the right shows the occupancy map generated from the front-facing Kinect image on the left. Green areas belong to the floor plane, and red areas lie outside the floor plane. Clearly, $y_{mm}$ coordinate information for these 3D points is lost in this particular representation. The $x$ axis of the image represents $x_{mm}$ values, whereas the $y$ axis of the image represents $z_{mm}$ values. The occupancy map image is generated such that the robot's position is situated at $\left(\frac{occ_{width}}{2}.occ_{height}\right)$, where $occ$ is the $400 \times 400$ occupancy map image.

Generation of occupancy maps is the first step in mapping. The mapping process is the process of stitching together occupancy images (or a representation thereof) while accounting for the rotation and translation of the robot relative to the reference occupancy image for the map.

### 4.3.3 Scan generation

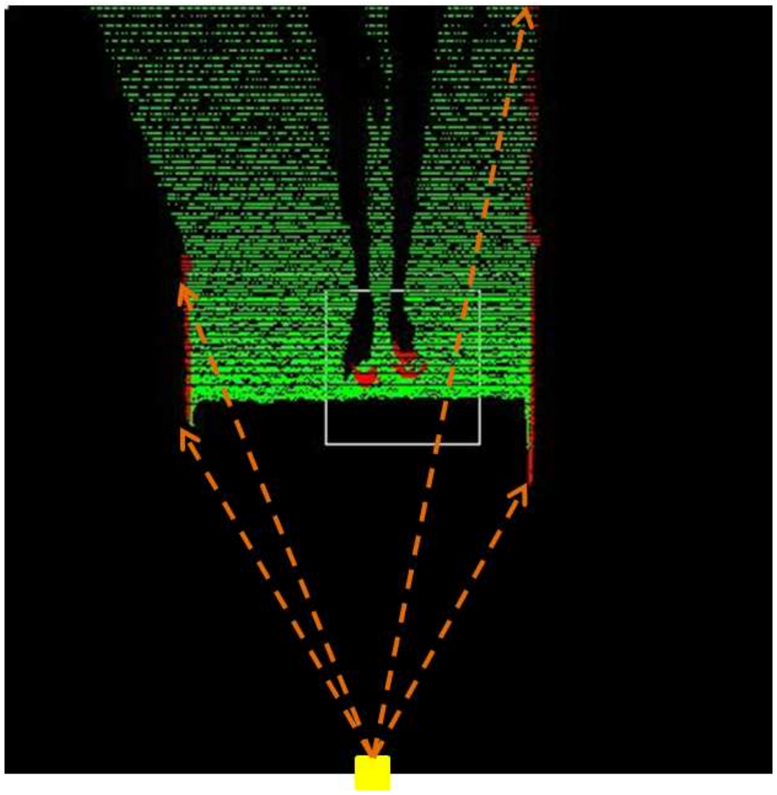

Figure 4.20: Generation of polar scans from occupancy maps

A set of $(r, \theta)$ pairs is generated with respect to the robot position indicated by the yellow square at the bottom of the image. Angle values are evenly spaced in the range $0 \ldots 180$. Dotted orange lines indicate the shortest radial distance to a non-floor point for some of the angle values. The person bounding box, shown using a white rectangle, is excluded from this process.

Estimating Manhattan rotation requires estimating wall lines in an image and computing the rotation of these lines relative to the wall line orientation at the reference map frame. The occupancy image could be used directly for wall line estimation. However, a typical occupancy map, e.g. Figure 4.19, contains a large number of closely clustered points. Line fitting algorithms working with such data may not converge to the best line estimates. With a large number of points in the raw occupancy data, it may take longer for line fitting to converge. Scan generation is an intermediate step which is used to reduce the number of points to be passed on to the line fitting, which is the next step in mapping.

Laser range finders generated scans which were often used for mapping [57] and pose estimation [105]. Inspired by the form of the raw data from laser range scanners, occupancy map data is reduced to a smaller number of points using the $(r, \theta)$ representation. The process is sketched in Figure 4.20. The robot, shown in yellow, is at the bottom-center of the occupancy map. the 180° range relative to this point is scanned with a user-defined resolution (in this case, $res_{scan} = 0.2°$, and the closest occupied (red) pixel along each direction (shown using dotted orange lines) is added to the list of scan points. To avoid the leader and other detected persons being added to such a list, red pixels belonging to skeletal tracks (surrounded by a white box in the image) are ignored during scan generation.

At the end of scan generation, a list of points $(r_i, \theta_i)$, $i = 1 \ldots 180/res_{scan}$, is available for line fitting and subsequently for estimating robot pose relative to the reference pose.

### 4.3.4 RANSAC for multiple lines

Given a set of scan points, line equations which fit the data are desired. The requirement for the line estimation algorithm is that it should be able to find all wall lines in the raw data, which is the set of scan points. This set of wall lines is used in estimating the pose of the robot relative to its pose at the time of map initialization or reset. Each line in the set of lines is estimated using a robust model parameter estimation technique called RANSAC [106].

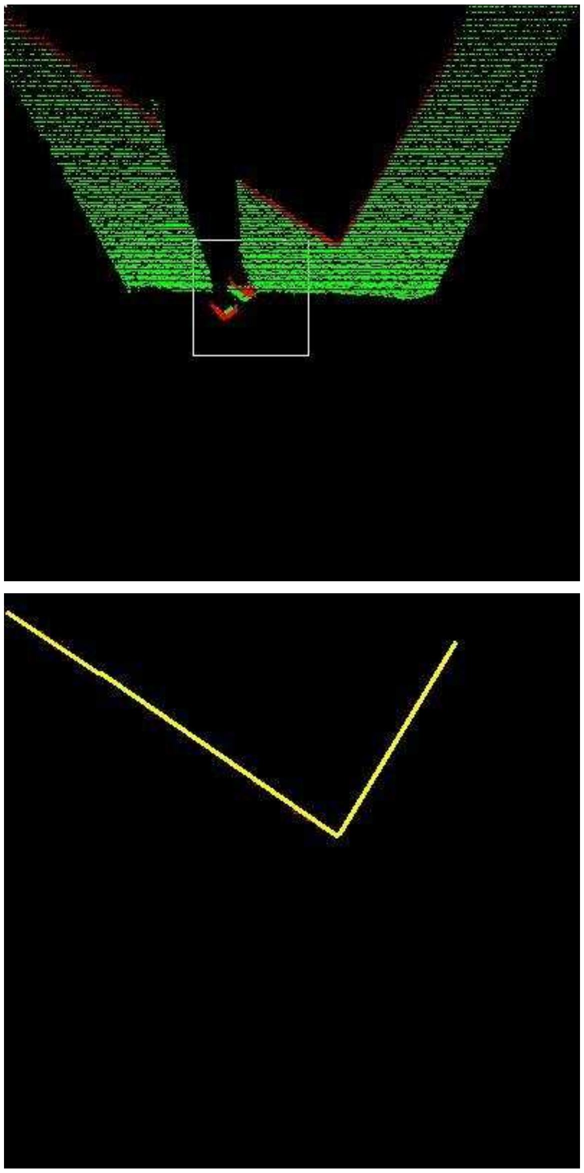
Figure 4.21: Multi-line RANSAC estimates from scan data

The top image shows raw occupancy image data. This is converted to a scan representation and multi-line RANSAC operates on scan data to estimate wall lines, shown in the bottom image using yellow lines.

RANSAC (or Random Sample Consensus) is used to estimate the parameters of a model from data. The advantage of RANSAC is its ability to reject outliers in the data using an iterative model fitting process. The algorithm is initialized using a minimum, random set of points required to estimate the initial model parameter set, which in this case is the slope-intercept pair $(m, c)$ from the standard line equation $y = mx + c$. Following this, other points from the data set which fit the initial model with an acceptable error are added to a set called the consensus set. Least squares line fitting is then used to revise the parameters of the initial line equation. The cumulative reprojection error of the model is then estimated using the revised parameter set.

The above process is repeated an arbitrary number of times, though it is possible to estimate an upper limit on the number of iterations required to find an acceptable parameter set, provided one exists [107]. The seed points used for initial parameter estimation are randomly chosen for each iteration, which gives this algorithm the randomness necessary to improve the chances of finding the a representative parameter set. Parameter sets and cumulative errors from all iterations are stored, and the lowest error set is chosen as being the desired line equation.

A single RANSAC run explained in the preceding paragraphs yields one of the many wall lines which may be available in the raw (scan) data. To get the rest of the lines, it is necessary to run RANSAC multiple times. For each run, the set of available points is pared down to the ones yet to be included in a consensus set. When a sufficiently large fraction of the total number of points has been included in one line or another, the multi-RANSAC loop terminates.

Each of the above constituent parts of multi-line RANSAC is expanded in the rest of this section. Steps (A)-(F) are iteratively carried out until a termination condition is satisfied.

A) **Initialize** the set of scan points $S_i = (r_p, \theta_p), p = 1 \ldots N_i, i = 0$ using the techniques from Section 4.3.3.

B) **Estimate a RANSAC line** using the revised set of scan points $S_i$. Multiple estimates are found from Step (1)-(8) and the best of these is considered to be the RANSAC line for the $i^{th}$ iteration.

1) For the current $j^{th}$ iteration, **initialize the consensus set** to an empty set, $C_j = \phi$.

2) **Randomly select two points** $pt^0_{S_i}$ and $pt^1_{S_i}$ from the set $S_i$. If the points are too close to each other or too far apart, select a different pair of points. This modification to the standard RANSAC implementation is necessary to filter out wall line detections which are either too short or too long. Add the two points to the consensus set $C_j$.

3) **Estimate the initial line parameters** $(m^{init}_j, c^{init}_j)$. If the line is vertical, these parameters come from the model $x = m^{init}_j y + c^{init}_j$. Otherwise, the model to be estimated is $y = m^{init}_j x + c^{init}_j$.

4) **Build the consensus set** using the initial model. For each point $pt^p_{S_i}, p = 1 \ldots N_i$ in the set $S_i$,

- Find the reprojected point $\bar{pt}^p_j$.
- Calculate the reprojection error in pixels, $err^p_j = \left\| \bar{pt}^p_j - pt^p_j \right\|$.
- If the error is below a threshold, $err^p_j < err^{init}_{max}$, add $pt^p_j$ to consensus set $C_j$.

From experimental data, it was found that a strict threshold of $err^{init}_{max} = 5$ pixels worked best for our data.

5) **Check the inlier ratio** for the consensus set $C_j$. Let the consensus set have $M_j$ points. Then the inlier ratio is given by $ratio^{inlier}_j = \frac{M_j}{N_i}$. Based on the inlier ratio, make a decision about continuing or skipping this iteration. If $ratio^{inlier}_j < ratio^{min}_j$, return to Step B(1). Since multiple wall lines might be visible to the sensor, this threshold is set to a rather low value of $ratio^{min}_j = 0.2$, i.e. 20% of points in $N_i$ need to satisfy this line parameter estimate to proceed with the remaining steps.

6) **Test the line consensus model**. Reestimate line parameters after having gathered the consensus set $C_j$ for this iteration. A revised consensus set is initialized and built during this step. Initialize it to an empty set, $C_j^{new} = \phi$. Steps (i) to (iii) are part of the consensus model testing process.

i) **Perform a least squares fit** to estimate line parameters using the consensus set $C_j$. The new line parameters are estimated as $(m_j^{new}, c_j^{new})$.

ii) **Find new consensus set inliers** from the current consensus set $C_j$. This is similar to Step B(3), except that the line parameters used for reprojection have been modified to $(m_j^{new}, c_j^{new})$ using the previous step. Get the sum of reprojection errors as $err_j^{total}$.

iii) **Check new consensus inlier ratio**. It is possible that the number of points in the original and new consensus set are not the same. Let the new consensus set have $Q_j$ points. Then the inlier ratio for the new consensus set is given by $ratio_j^{new_i nlier} = \frac{Q_j}{N_j}$. If this ratio has reduced to less than the line fitting threshold $ratio_i^{min}$, return to Step B(1).

The new consensus model has now been tested and verified. Replace the original consensus set with this set of points, i.e. $C_i = C_i^{new}$. Thus, the consensus set now has $Q_j$ members, the inlier ratio is now $ratio_j = ratio_j^{new}$, and $m_j = m_j^{new}, c_j = c_j^{new}$.

7) **Compare current estimates to the best available estimates**. If the cumulative reprojection error from Step B(6)(ii), $err_j^{total}$, is currently the lowest across iterations, then store the current line parameters as the best available fit. That is: $m_j^{best} = m_j, c_j^{best} = c_j$. Also update the best consensus set to be $C_j^{best} = C_j$.

8) **Check early loop termination condition** for RANSAC. If the inlier ratio $ratio_i$ is greater than a threshold $ratio_j^{max}$, then break out of the current line fitting RANSAC loop. For wall line fitting experiments, if more than 50% of the

points in the set $S_i$ were assigned to a line, $ratio_j^{max} = 0.5$, then the current line was declared a good estimate. If enough iterations have been run, exit the RANSAC loop. The maximum number of iterations for this experiment was $j_{max} = 250$. If neither of the previous stopping conditions is satisfied, return to Step (B)(1).

C) **Get properties of the RANSAC line**. Using the best line estimate from Steps B(1)-B(8), calculate properties of the RANSAC line which will be useful for the rotation estimate:

- Extreme points of the line.
- Length of the line.
- Angle of the line with respect to the image $x$ axis.

D) **Reduce the set of points** available for the next line estimate. Elements of the best consensus set $C_j^{best}$ are removed from the scan points set $S_i$. If the best consensus set contained $M_j^{best}$ points, then the revised scan points set contains $N_i = N_i - M_j^{best}$ elements.

E) **Check scan point termination condition**. The ratio of points currently assigned to one of the lines is given by $ratio_i^{scan} = \frac{N_0 - N_i}{N_0}$. If enough points have been assigned to one of the lines, i.e. $ratio_i^{scan} > ratio_{max}^{scan}$, then terminate multi-line RANSAC. This termination value was set at $ratio_{max}^{scan} = 0.8$, i.e. 80% points have been assigned to one of the lines. If enough iterations have been run, $i_{max} = 100$ in this case, then terminate multi-line RANSAC. If neither of the previous conditions is satisfied, return to Step (B).

The output of multi-line RANSAC is a set of lines which are representative of the wall lines in the hallway. This set, along with additional line properties computed in Step (C) of the above algorithm, facilitates estimating Manhattan rotation as explained in the next section. An example of multi-line RANSAC is seen in Figure 4.21, with the occupancy image at the top and its corresponding wall line estimates at the bottom.

### 4.3.5 Using Manhattan assumption for rotation

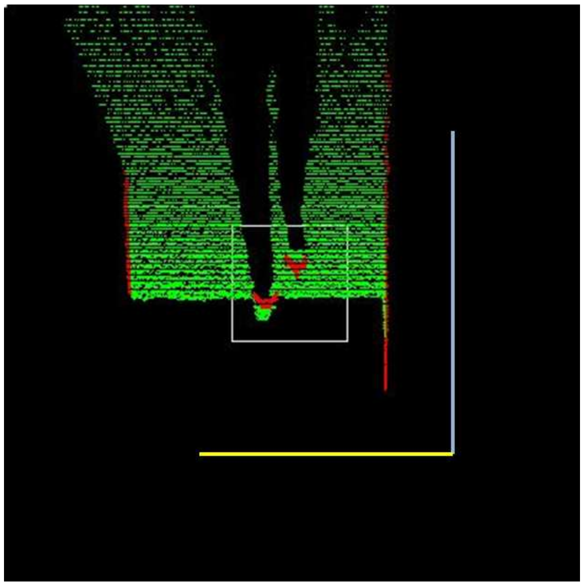

Figure 4.22: Reference bins for Manhattan estimate.

The blue line shows the dominant wall line direction inferred by multi-line RANSAC from occupancy data. The yellow line perpendicular to it is the other 'bin' for Manhattan rotation estimates.

To estimate the rotation of the robot relative to the map origin, the Manhattan assumption is used. The assumption is that planes which are used for mapping an indoor environment, e.g. walls, are mutually orthogonal. Such a map generation method has been proposed by Peasley et al. [59], with Manhattan constraints used in combination with factor graphs to generate occupancy grids of large indoor environments. The Manhattan assumption has also been used in 3D reconstruction [60].

Making this assumption is an effort to find a drift-free rotation estimation method in mapping. An overview of SLAM and standard SLAM techniques was presented in a tutorial by Durrant-Whyte and Bailey [51, 52]. In conventional SLAM techniques, 3D correspondence between frames is used as the basis for estimating inter-frame translation and rotation. Such correspondence can be obtained using 3D point cloud data directly and establishing correspondences between 3D features [103], or combining 2D feature matching (e.g. joint Lucas-Kanade [99]) with depth data from RGB-D sensors, or performing scan matching between the polar scan representations of successive frames [57]. However, these techniques rely on accurate inter-frame rotation estimates to be effective for mapping. One poor set of correspondences can throw the map off completely or introduce a rotational drift which accumulates over time.

An effective way to counter inter-frame drift due to correspondence errors is to take point correspondences completely out of the picture and replace them with another type of feature which is most commonly found in the mapping environment. The presence of wall lines is one such feature for indoor environments. As explained in the previous section, RANSAC provides a set of line estimates for wall lines in any given occupancy image.

To apply the Manhattan assumption, wall lines found in the initialization frame of the map used to get the reference line for rotation. This is done by taking the median of all the line orientations detected in multi-line RANSAC. Since median orientations for subsequent lines belong to planes which are either parallel or perpendicular to the reference orientation, Manhattan rotation is estimated as the difference between any given median orientation and the initial orientation. This process is explained ahead in detail.

Consider Figure 4.22. The blue line is the line detected by RANSAC in the

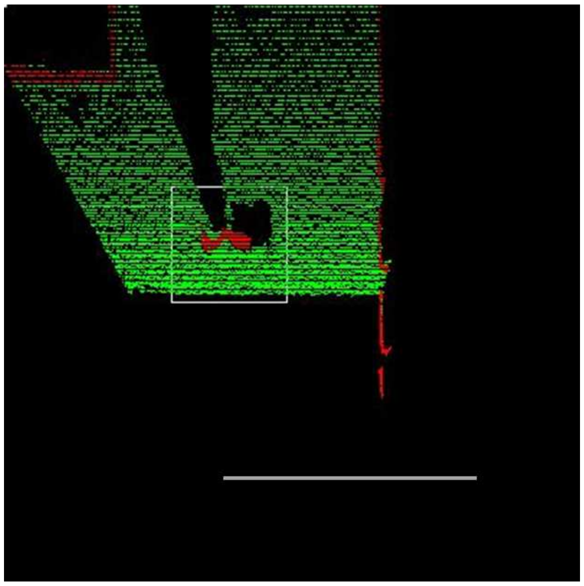

Figure 4.23: Sample mapping frame for Manhattan estimate.

The gray line in this image is the estimated RANSAC line. This is compared with the initialization map RANSAC lines to ultimately give inter-frame and total rotation for mapping.

initialization or reference frame, frame 0. Let $\theta_{a_0}$ be the angle of this line with the horizontal. Another 'bin' is created for the purpose of matching future line detections to this reference line. Let $\theta_{b_0} = \theta_{a_0} + 90^\circ$ be the value of this bin, represented by the yellow line in the figure.

Consider, for example, a subsequent frame $n$ in the mapping trial in Figure 4.23. Let the orientation of the median line with respect to the horizontal be $\theta_n$. Suppose the median RANSAC line (shown in gray in the image) is orthogonal with respect to the reference line from Figure 4.22. This could mean one of two things:

- The robot has rotated nearly $90^\circ$ relative to its initial pose, or
- There is a wall ahead of the robot which is perpendicular to the wall observed in the initial frame.

To disambiguate these conditions, $\theta_0^n$ is always chosen as the minimum of $|\theta_n - \theta_{a_0}|$

and $|\theta_n - \theta_{b_0}|$ . Inter frame rotation is measured as $\theta_{n-1}^{n} = \theta_0^n - \theta_0^{n-1}$. The total rotation of the robot relative to its initial pose, for frame $n$ is then recursively determined as

$$\theta_{n_{total}} = \theta_{n-1_{total}} + \theta_{n-1}^{n} \tag{4.2}$$

. The creation of orthogonal bins thus helps in resolving the ambiguity in Manhattan estimation.

Thus, the process of scan generation, multi-line RANSAC, and Manhattan rotation estimation result in an estimate of the rotation of the robot relative to its initial pose.

### 4.3.6 Approximating translation using dead reckoning

To map data from the current scan to the composite map of the environment, translation estimate relative to the map initialization frame is required. Since the robot is translating in the $(x, z)$ plane, let the two translation estimates be represented by $(x_{n_{total}}, y_{n_{total}})$, where

$$\begin{aligned} x_{n_{total}} &= x_{n-1_{total}} + \Delta x_{n-1}^{n} \\ z_{n_{total}} &= z_{n-1_{total}} + \Delta z_{n-1}^{n} \end{aligned} \tag{4.3}$$

where $\Delta x_{n-1}^{n}$ and $\Delta z_{n-1}^{n}$ are inter-frame translations along $x$ and $z$ axis, respectively.

In the absence of reliable translation estimates from visual odometry and point cloud matching techniques, the motion pattern of the robot is used to estimate inter-frame translations. While following a leader, the robot first aligns itself with the leader by rotating to the observed leader angular offset, and then translates with a fixed velocity along this vector. Translation continues until the next motion command is received based on the leader's new position. This process of stop-rotate-translate is designed to give the mapping system enough information to estimate inter-frame translation.

Let $\Delta t^n_{n-1}$ be the time elapsed since the last translation estimate. From the motion algorithm, we know that the robot has been commanded to translate at a known velocity, represented by $\dot{r}^n_{n-1}$. Then the distance traveled by the robot between frames is given by

$$r^n_{n-1} = \dot{r}^n_{n-1} \cdot \Delta t^n_{n-1} \tag{4.4}$$

To get the total translation of the robot (relative to map origin), the radial translation in Eqn. 4.4 has to be expressed in terms of its Cartesian components. Using Eqn. 4.2, these components can be expressed as follows:

$$\begin{aligned} \Delta x^n_{n-1} &= \cos(\theta_{n_{total}}) \cdot r^n_{n-1} \\ \Delta z^n_{n-1} &= \sin(\theta_{n_{total}}) \cdot r^n_{n-1} \end{aligned}$$

Thus, all the terms in Eqn. 4.3 have been determined and the translation of the current frame relative to the map initialization frame has been calculated. All data required to build and update the map is available.

## 4.3.7 Map building and output

The map is generated as a square image of arbitrary size, with the scale of $1 \text{ pixel } = 10 \text{ mm }$ along each image axis. Thus, a $1600 \times 1600$ image covers a mapping area of $16 \times 16$ meters, which is substantial in terms of its applicability to the person following problem.

The occupancy image generated in Section 4.3.2 has been converted to a scan representation using the method in Section 4.3.3. The coordinates of each of these scan points are transformed to global coordinates. Let the scan point for frame $i$

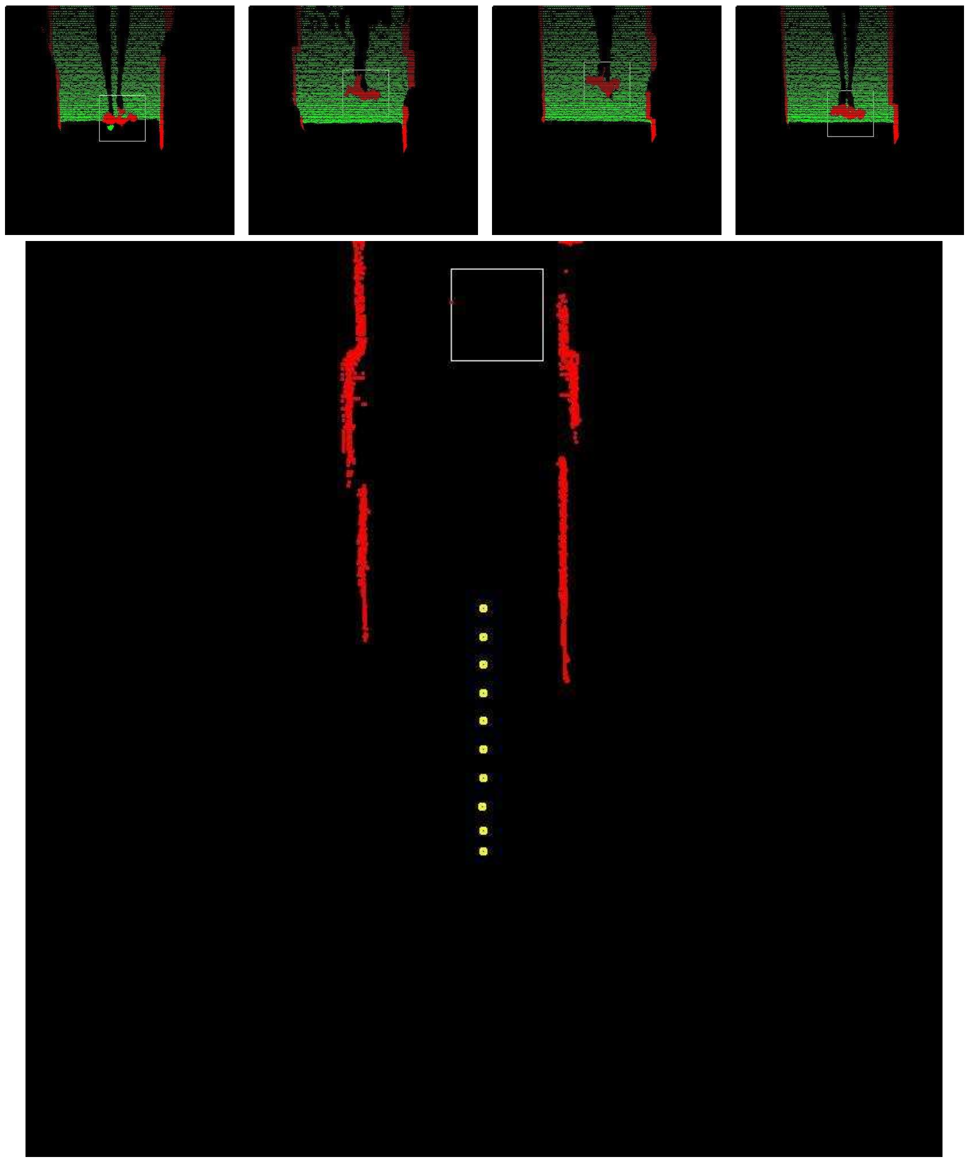

Figure 4.24: Map output down a straight hallway.

Occupancy images, a sample of which is shown in the top panel, are stitched together using the mapping algorithm to yield the map image. Red pixels in the map image are aligned scan points from the first to the current frame, and yellow dots show the motion of the robot down the straight hallway. The white rectangle is the position of the leader in the current frame.

be at an angle $\theta_i$ relative to the robot position during that frame. Let $r_i$ be the radial distance between the point location and the robot location in the $(x, z)$ plane. Then, using the total rotation and translation estimates from Eqn. 4.2 and Eqn. 4.3

respectively, the scan point is situated on the map at:

$$\begin{aligned} x_{i_{n_{total}}} &= x_{n_{total}} + \cos(\theta_{n_{total}}) \cdot r_i \\ z_{i_{n_{total}}} &= z_{n_{total}} + \sin(\theta_{n_{total}}) \cdot r_i \end{aligned} \tag{4.5}$$

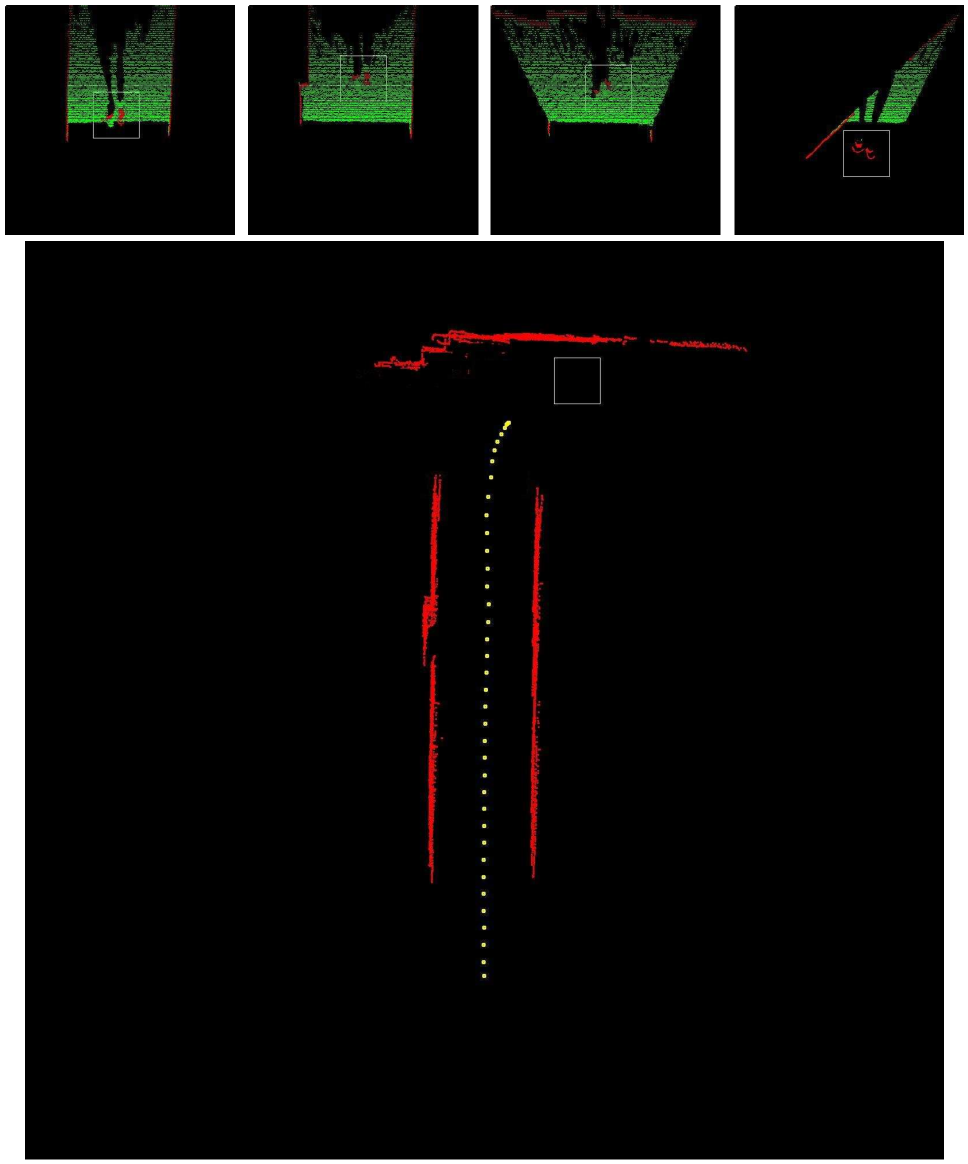

Figure 4.25: Map output at a L-junction.

The layout and characteristic features in this figure are identical to Figure 4.24. Yellow dots show the motion of the robot as it turns around the L-shaped hallway.

The map is reset when one or more of the following conditions are satisfied:

1. No RANSAC line estimate could be found for the given frame.

2. Leader is close to one of the edges of the map image.

3. Leader position is inferred to be on one of the ‘occupied’ map pixels.

4. Robot position is inferred to be on one of the ‘occupied’ map pixels.

While the last two conditions are obvious indicators that something has gone wrong with the mapping output, the second condition is simply a map reset triggered by the range of the map. For the practical Level-3 follower, a range of $16 \times 16$ meters was found to be sufficient, however, there may be environments in which a larger map may be required. Alternately, it should be possible to completly eliminate range resets by discarding older positional information and shifting the entire map up-down or left-right using a shifting logic appropriate for the application. A logical resolution of the first reset condition remains elusive. Since rotation and translation estimates both rely on good Manhattan estimates, a RANSAC failure propagates all the way to the final output. Hence, RANSAC failures mandate a map reset.

The output of the map for three typical hallway configurations is shown in a Figures 4.24, 4.25, and 4.26. In all of these figures, the four images at the top are occupancy maps at various interesting or representative stage in map building. The image at the bottom of each figure shows the final map output, with the white box in the figure showing leader position in the final frame and yellow squares showing the position of the robot as it followed the leader during the trial.

In Figure 4.24, the robot follows a leader down a straight passage. The fact that door frames seen in the occupancy image neatly overlap in the map output is indicative of the translation estimate being accurate. In case of poor translation

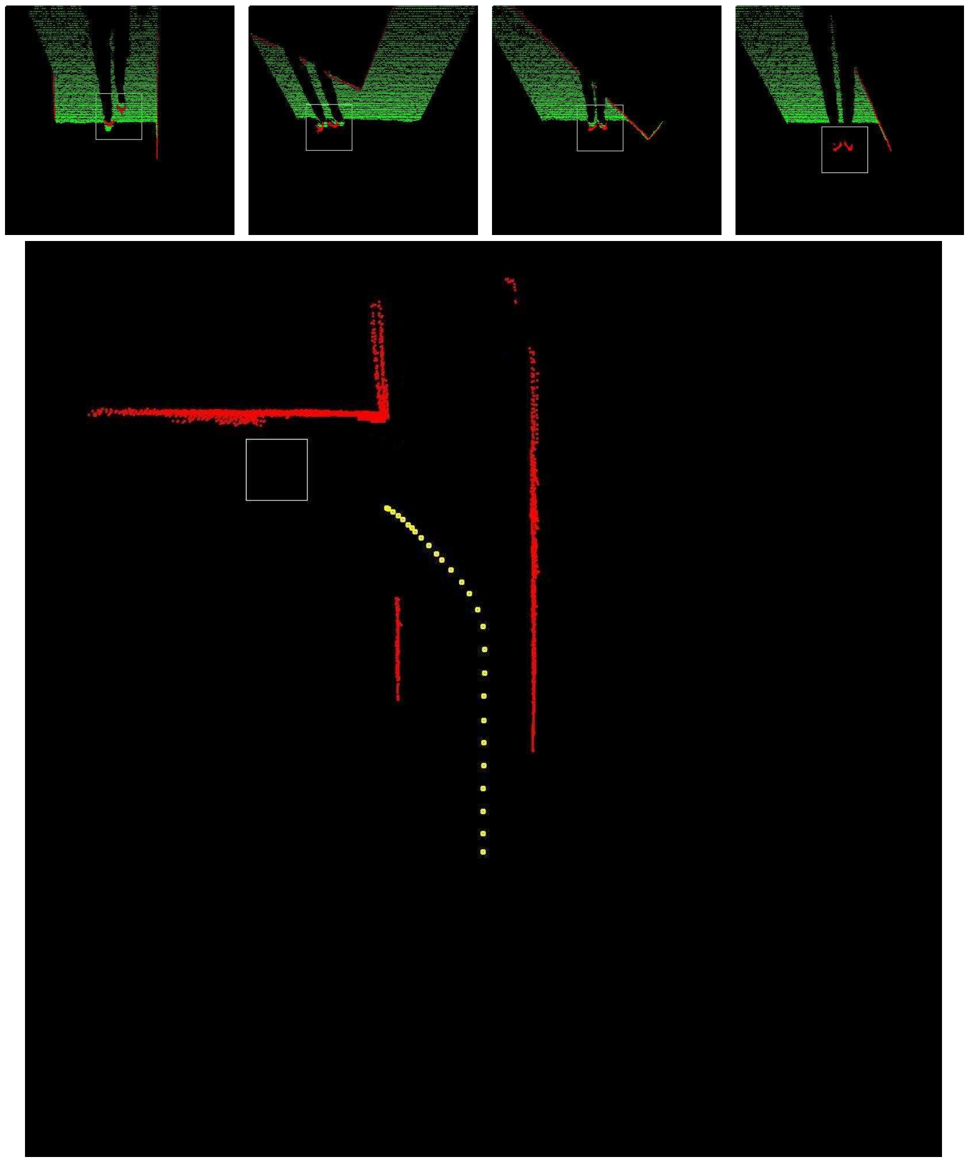

Figure 4.26: Map output at a T-junction.

The layout and characteristic features in this figure are identical to Figure 4.24. Yellow dots show the motion of the robot as it turns around the T-shaped hallway.

estimates, the overlap for such features in the environment is poor. In Figure 4.25, the robot follows the leader around a L-junction after a long straight route in the initial part of the trial. Performance over both the straight section (as seen by the alignment for the door frame on the left side of the map image) and around the corner is seen to be good. The map output is clean. A similar observation can be made for Figure 4.26. The robot turns into the T-junction, and the corners of the junction are aligned.

A combination of Manhattan rotation estimation and translation estimates using dead reckoning, with floor segmentation, scan generation, and RANSAC processing the raw sensor data, thus generates a local environment map. This map is used as an input to the path planner in the event that the leader is occluded.

## 4.4 Person following using predictive fields

### 4.4.1 Setup for predictive fields person following

In Section 2.4, a representation of workspaces for using the predictive fields path planner in the person following problem was described. The outline of the algorithm was as follows:

1. Track the location of the leader using the RGB-D sensor.
2. When the leader is occluded or close to the end of the sensor range, mark the last observed location of the leader as the 'goal' position for the path planner.
3. Represent the workspace as a composite of circular obstacles.
4. Represent moving obstacles using an elliptical predictive field.
5. Use navigation inputs to drive the robot to goal.

These steps are repeated until the end of the trial. The end of the trial can be any user-defined event. In this case, the leader standing still in front of the robot for 3 seconds was used to signal the intent of the leader to stop the trial.

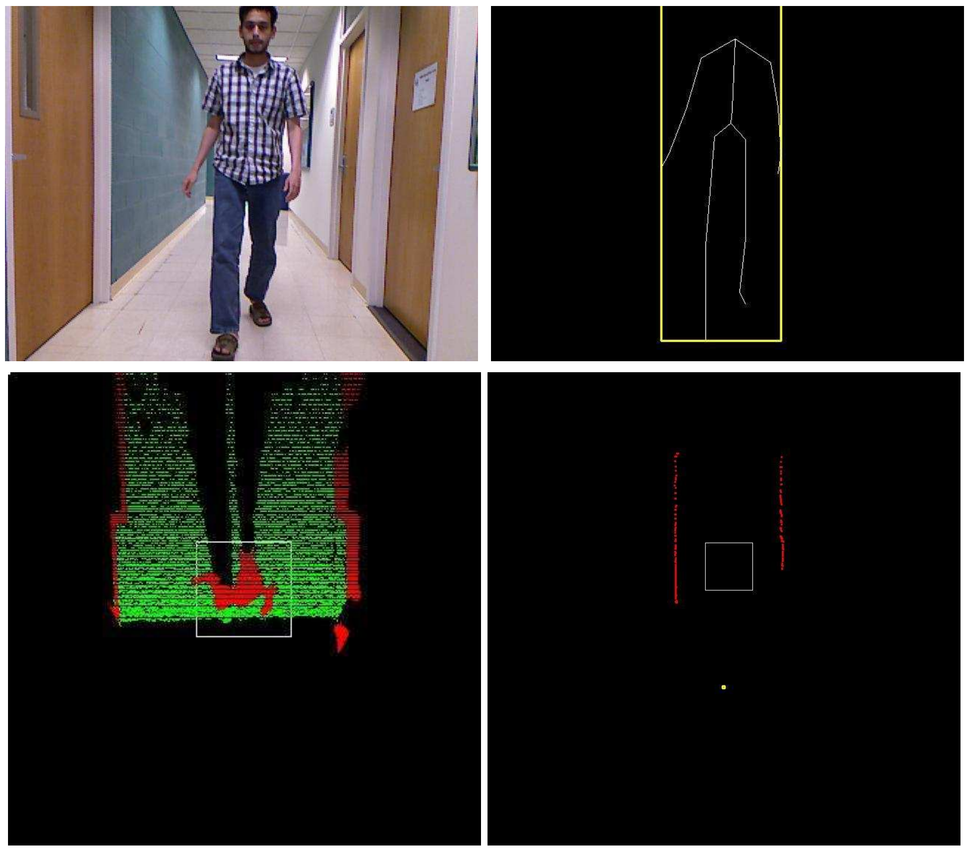

Figure 4.27: Initialization for a trial.

A trial is initialized by a person standing in front of the robot. The image on the top right shows that this person is detected as the leader and a descriptor is generated. A bounding box is created for the leader to avoid leader pixels from factoring into RANSAC estimates. The occupancy image and leader box is shown in the image on the bottom left. The bottom right image shows map initialzation, in which wall points are marked by red pixels, leader box is the white rectangle, and robot initial position is the yellow dot.

From the above list, the connection between person following, as described in this chapter, and path planning, described in the previous two chapters, can clearly be established. Path planning requirements for the person following classification of Level-3 are defined in Section 4.1. The leader is ideintified and his/her location tracked using the combination of skeletal tracking and appearance-based descriptors from Section 4.2. For path planning inputs to be calculated, the algorithm relies on a map of the environment generated in Section 4.3.

The setup for the use of path planning integrated with person following is as follows. A forward-looking Kinect sensor is mount on a tripod on a Pioneer P3-AT robot. Both the Kinect and Pioneer are interfaced with the laptop sitting at the back of the Pioneer. As a calibration step, the floor plane may be established by the user using the procedure from Section 3.3.1. A floor plane threshold of 3.5 was found to be acceptable for the forward-looking sensor. An experimental trial begins with the leader standing in front of the robot. When the skeletal tracker has detected the person, a leader descriptor is generated and used as the person identification reference for the rest of the trial. Initialization data for a typical trial is shown in Figure 4.27.

### 4.4.2 Person following strategy - exact following and path planning

The robot attempts to follow the leader 'exactly' as long as the leader is visible. This means that the control input to the robot is similar to a proportional control input with saturation, i.e.

$$\begin{aligned} \dot{r} &= \min(r_{observed} - r_{desired}, \dot{r}_{max}) \\ \dot{\theta} &= \theta_{observed} - \theta_{desired} \end{aligned}$$

where $(r_{observed}, \theta observed)$ are polar coordinates of the leader with respect to the robot. The desired straight line distance to the leader is given by $r_{desired}$ and the leader should ideally be at the center of the Kinect's field of view, i.e. $\theta_{desired} = 90°$. Translation and rotation inputs are in mm/sec and degrees/sec respectively.

When the leader is occluded or moves out of sensor range, the leader following module switches to the path planner. As explained in Section 4.1, Level-3 following requires a 'patient leader', i.e. someone who waits for the robot to overcome occlusions

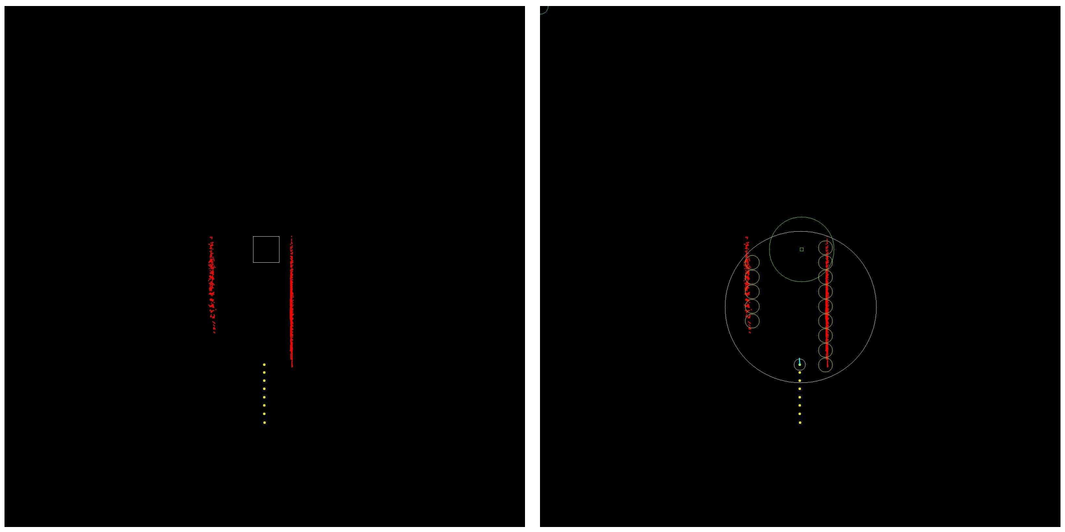

Figure 4.28: Transition from exact following to path planning.

When the leader moves out of sensor range or is occluded, the path planner gets activated. In the image on the left, the leader (white rectangle) is about to move out of sensor range relative to the robot (yellow dots). This activates the path planner. Adjacent circles along the red pixels are wall obstacles. The small circle around the last yellow dot from the image on the left is the robot initial position, with blue and white lines indicating actual and desired heading as per navigation inputs. The small dot at the top of the workspace is the leader position, and the green circle around it is the stopping radius around the leader, fixed by the minimum sensing distance for the Kinect. If the robot reaches the border of this circle, navigation stops and robot waits to reacquire the leader.

or environmental obstacles during the trial. So the underlying assumption is that the leader waits, or at least does not move a great distance relative to the position where he/she was 'lost' to the robot. The switch from exact following to path planning requires the robot's environment to be characterized using circular envelopes in the manner described in Section 2.4.

To get this representation, the goal position is identified as the last observed location of the leader relative to the local map. Robot initial position is the current position of the robot relative to the map. To get obstacle positions, the map image is divided into a grid of $m \times n$ square cells. The number of red pixels, signifying an occupied pixel location in the map, in each cell is counted. If this number is above a threshold, then a wall obstacle is assigned to that cell, with the same diameter as the width of the cell. The workspace envelope is placed at the central point between robot initial position and goal position. Its radius is assigned to be the distance to the robot (or goal) plus a padding value to ensure that the robot does not start close to the workspace boundary.

The output of this process is seen in Figure 4.28. The image on the left shows the point in the trial where the leader is about to move out of robot sensor range. This triggers the path planning mode of operation, and the workspace representation is generated as shown in the image on the right. Walls are seen to be enveloped with orange circles, designating the detected obstacles for the path planner. Yellow dots show the path taken by the robot in previous frames, and the initial position of the robot is marked by the yellow dot with a circle drawn around it. There are two lines overlaid on this robot circle. The goal position is marked by a small rectangle near the top of the workspace envelope.

### 4.4.3 Experimental results for path planning

The performance of the predictive fields path planner is demonstrated using three typical scenarios:

- Robot overcomes sensor range occlusion in the presence of environmental obstacles.
- Robot overcomes sensor range occlusion in the presence of a stationary human in the workspace.
- Robot overcomes moving obstacle occlusion, where the moving obstacle is another human in the workspace.

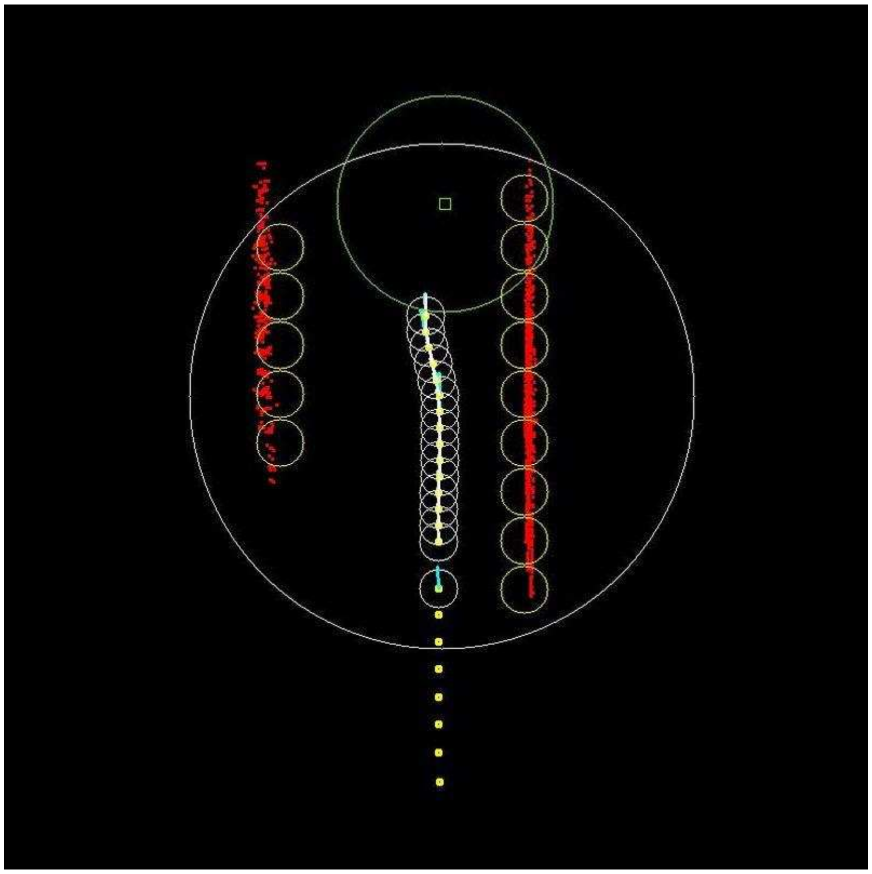

Figure 4.29: Path planning to overcome sensor range occlusion.

Example of sensor range occlusion recovery. The significance of the features in the map is explained in Figure 4.28. Overlapping white circles show the path of the robot to the last observed leader position.

The description of Figure 4.28 is completed by commenting on objects in the image which represent run-time events. The blue line is the observed heading of the robot, from Manhattan rotation estimates, and the white line is the desired heading. Another circle has been added to the representation and that is the circle drawn around the goal position. If the robot is within this circle and the leader has been reidentified, then the path planner switches off and the 'exact following' mode resumes. In every case, the trial stops after the leader is stationary for a few seconds.

The navigation method for the robot to move to goal is described as follows. On establishing the workspace configuration, the path planner returns a directional vector as the velocity input to the robot. This is converted to a heading in degrees. The current heading of the robot is estimated using the scan data - RANSAC - Manhattan rotation system. The robot is rotated gradually to its desired heading (to allow for a more accurate inter-frame Manhattan estimate) and then translated for a fixed period of time at a fixed velocity along this new orientation. This process continues until the robot has converged to goal.

Figure 4.29 shows the path planning-based recovery from sensor range occlusion of the leader. In this type of occlusion, the leader travels beyond the sensor range of the Kinect ($4000mm$) and the robot has to go to the last observed leader location to recover from this event. Small overlapping circles in the image show the path taken by the robot from the time the leader has been occluded to the time it is close enough to be able to reidentify the leader. If the leader has, once again, moved out of sensor range of the Kinect, the robot waits at the goal position and it is expected that the leader will return to the Kinect's field of view to allow a resumption of the person following activity. The last requirement is appropriate for the 'patient leader' scenario.

Figure 4.30 shows an example of the robot planning a path in the case of sensor range occlusion with the leader and another individual. The image to the left shows the robot leader and another person in the field of view of the Kinect. Eventually, the leader (standing to the right) moves out of sensor range. In keeping with the occlusion recovery method, the algorithm first tries to match the descriptor of the person still in sensor range, and an inadequate match score triggers the path planning method for occlusion recovery. Wall obstacles are identified using the grid method, and the detected, non-leader person is labeled as a potential moving obstacle

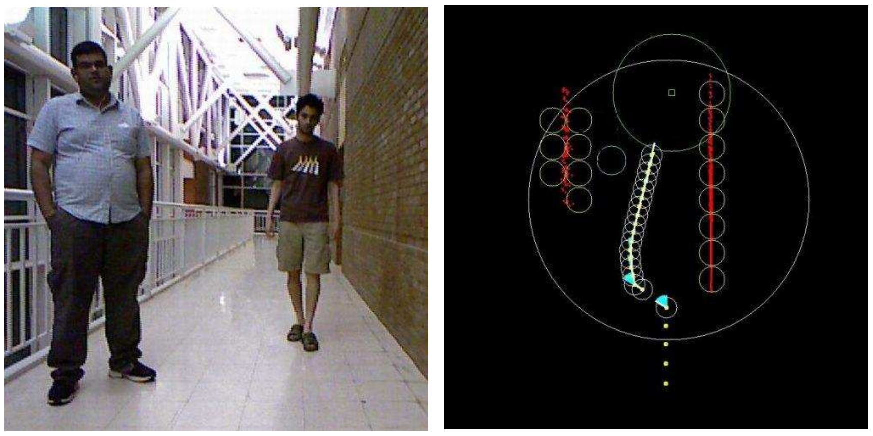

Figure 4.30: Path planning around a single stationary person.

Example of path planning with a single stationary obstacle. In addition to wall obstacles, the stationary person is represented by the blue circle in the workspace. The significance of the rest of the features in the map is explained in Figure 4.28. Overlapping white circles show the path of the robot to the last observed leader position. The robot is initially pushed away from the wall obstacle to the bottom right before it moves towards the goal, avoiding the person in the process.

(represented by a blue circle in the figure). As long as the person is stationary, as was the case throughout this trial, the predictive field around him remains the circular obstacle envelope.

The robot is initially driven by a sequence of rotation commands, because of its proximity to the wall when it began occlusion recovery. After this, the robot is attracted to goal while steering past the stationary individual in the workspace.

Figure 4.31 shows an example of the robot handling leader occlusion by a moving obstacle using predictive fields path planning. To set up this proof of concept demonstration, the leader gradually walked away from the robot until, at about half the distance from the robot and the leader, the occluding person began crossing the path of the leader to occlude him. The image on the left in the figure shows the initial condition of the workspace at the time of occlusion.

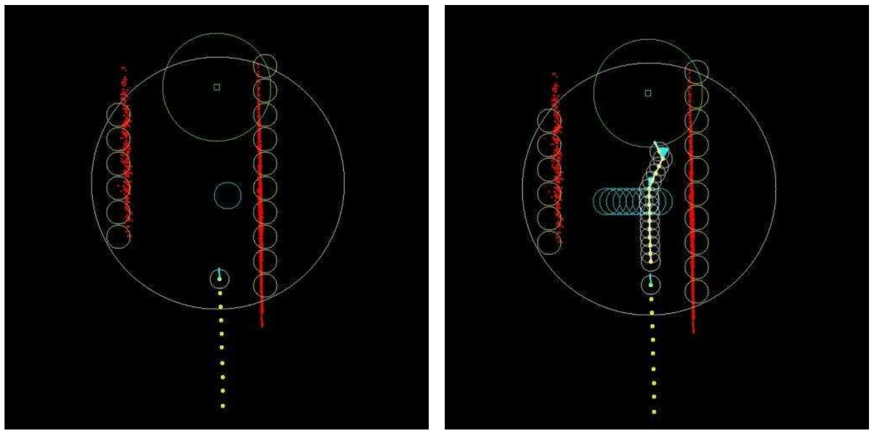

Figure 4.31: Path planning around a moving occluding person.

Example of path planning with a single moving obstacle. In addition to wall obstacles, the moving obstacle is represented by overlapping blue circle in the workspace. The obstacle moves from the right of the image to the left. The significance of the rest of the features in the map is explained in Figure 4.28. Overlapping white circles show the path of the robot to the last observed leader position. The robot moves towards the goal, avoiding the moving obstacle using motion prediction to keep it away from the path of the obstacle.

Since the person was moving from the right to the left of the image, the generated ellipse reflected this direction of motion, as seen in Figure 4.32. The position of the moving obstacle was projected along the major axis for reasons outlined in the discussion on predictive path planning. This form of 'advance knowledge' of the motion of the person kept the robot away from the projected path of the person. The image to the right in Figure 4.31 shows the trajectory of the robot and the occluding person.

Occlusion handling is successfully completed as the robot crosses the moving obstacle without collisions and moves close to the leader. The leader is reidentified using the generated descriptor and 'exact following' resumes.

This completes the demonstration of the predictive fields path planner as part of the person following system. At this point, all modules of the person following robotic system,represented block diagramatically in Figure 1.1, have been developed

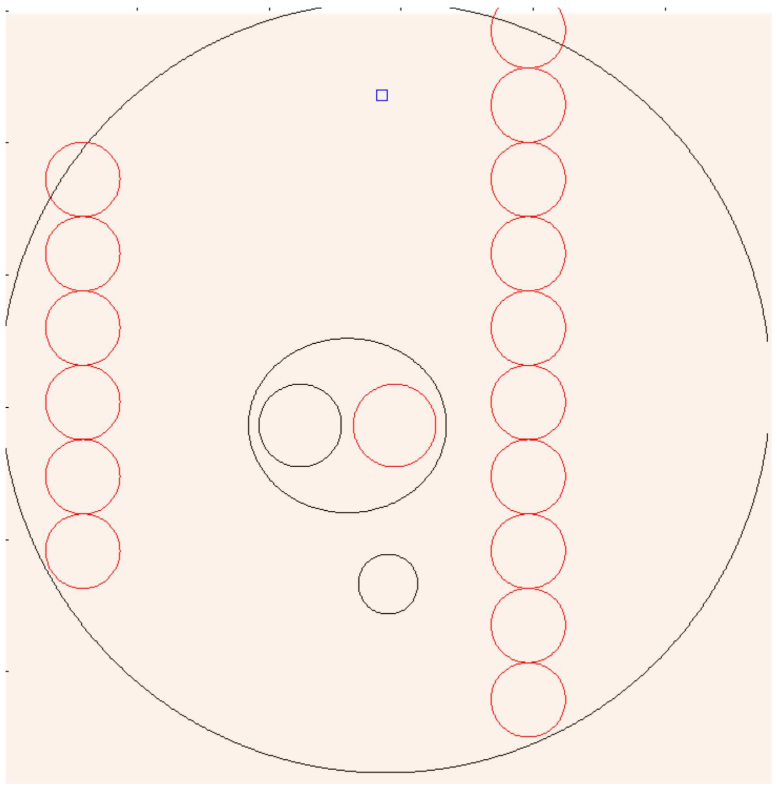

Figure 4.32: Ellipse generated around the occluding person.

Navigation inputs to the robot are computed in MATLAB using its COM server environment, and the output is relayed to the C++ program. Moving obstacle ellipse as plotted in MATLAB is shown in this figure. The red circle shows actual position of the obstacle, and black circle shows its projected position. The robot, shown using a black circle at the bottom of the image, converges to the goal, shown by a blue square at the top of the image.

and their results demonstrated. In the next chapter, a summary of the present state of our person following system is presented and potential future work directions highlighted.

# Chapter 5

# Conclusions and future work

The goal of the work presented here was the development of a robotic person follower capable of identifying its leader, handling leader occlusions, generating a map of its local environment, and navigating to its a position relative to the leader by using a combination of 'exact following' and path planning. In this chapter, the technical contributions made are reviewed and future research directions are discussed.

## 5.1 Conclusions

Person follower systems in described in literature have been either explicitly or implicitly defined in terms of the capabilities of the robot follower. The role of the human, central to this human-robot interaction system, has not been defined. In the work here, **a novel human leader-based classification system for person followers was developed** (Section 4.1). This classification system identifies four levels of expected leadership: 'Level 1' or 'Fully cooperative leader', 'Level 2' or 'Partially cooperative leader', 'Level 3' or 'Patient leader', and 'Level 4' or 'Independent leader'. Contemporary person followers were classified with the system to illustrate how the system can be used to identify the similarities and differences between disparate robotic systems. Such a system may be useful to identify the robot 'class' when service robots with a strong or central person following component become commercially viable.

The work proposed here best fits the 'Level 3' follower classification. For Level 3 systems, occlusion handling is mandated, and **an occlusion detection and recovery algorithm was developed** (Section 4.2) for this purpose. This algorithm is based on building an appearance descriptor around the reliable and robust Kinect skeletal tracker. Skeletal information from the tracker is augmented with a descriptor based on HSI and L*a*b* (CIE 1976) color spaces to create a leader descriptor. After the leader descriptor is generated, descriptors in subsequent frames are compared to infer and handle occlusions. It was found that the generated descriptor was sufficiently discriminative and the robotic follower was consistently able to identify its leader and infer occlusions.

To follow a person around occlusions, the robot needs to localize itself in its environment. To enable this, **a simple mapping approach was developed** (Section 4.3). This localization is achieved using a combination of multi-line RANSAC, Manhattan rotation estimates, and dead reckoning odometry. Low-drift local maps were generated as a result, and it was found that a good RANSAC implementation was central to the consistent performance of the system. The combination of these elements yields an improved approach to generate low-drift maps using low-cost, off-the-shelf sensors.

The local map serves as input to the path planning module. The navigation function path planner was chosen for its mathematical rigor and modified to develop **a path planner sensitive to obstacle motion** (Section 2.2). This path planner, called the predictive fields path planner, uses an elliptical envelope to represent the predicted motion of obstacles. The repulsive field generated by such a representation drives the robot away from the path of danger, i.e. away from the predicted paths of obstacles. The concept of danger was quantified using a metric called the 'risk score', and it was shown that using the motion encoding ellipse generates a lower risk score than the no-ellipse case for a variety of typical scenarios. This work represents a significant enhancement to the static navigation function approach as it facilitates path planning in more realistic, dynamic environments.

To guide the robot to goal, **a method to generate practical control inputs to the robot is developed** (Section 2.3). Navigation function path planning resulted in unpredictably high control inputs and extremely sensitive gain parameters. It was shown that using a normalized control input, used by predictive fields path planners, resulted in a stable system; moreover, normalized inputs (in the magnitude range $[-1 \ldots 1]$) could be interpreted as direction inputs which could easily be followed by the robotic system. Experimental and simulation implementations confirm this feature of the control method.

To apply the controller in a practical environment, **a method to implement predictive fields in practical workspaces was developed** (Section 2.4). This representation obviated the need for the special 'star-world' transformation required by navigation functions for the robot to operate in practical worlds. This representation also included leader waypoint generation method which makes it possible for the path planner to navigate in highly dynamic workspaces where the robot, obstacles, and goal may all be simultaneously in motion. Simulation results corroborate the utility of the workspace representation and the path planning technique in general.

Finally, **an experimental verification of predictive fields path planning was provided** (Chapter 3). This is one of the first experimental demonstrations of navigation functions in literature. Navigation functions, though widely cited for their formulation and mathematical properties, have rarely been used in mobile robot experiments. Various prohibiting factors were discussed in previous points. However, after overcoming these limitations with the modified approach, it was possible to demonstrate both navigation functions and predictive fields in an experimental setup. Two types of experiments were conducted. The first used a combination of the Kinect and iRobot Roomba; the second was the demonstration of predictive fields navigation in the framework of the person follower (Section 4.4.3). This is compelling demonstration of navigation functions in everday environments using standard sensors and robots and it is hoped that this encourages more widespread experimental development of this classic path planning technique.

Thus, a complete robotic system to follow a person around occlusions in indoor environments using path planning was designed and experimentally demonstrated.

## 5.2 Future work

Possible future directions for the work described here are:

- **Develop benchmarks to augment the person follower classification system**. The classification system, in its present form, is a handy guideline for expected human-robot interaction for a given person follower. However, this system, and the area of service robotics research in general, does not have a set of benchmarks against which the performance of a follower could be measured. For example, though it is possible to categorize a system as a 'Level 3' follower, there is no way of comparing one 'Level 3' system with any other. Thus, the question of quality of a person follower has only subjective explanations.
- **Develop a leader model using additional modalities to supplement**

**the appearance model**. The leader appearance model, even with its use of robust color spaces for descriptor generation, has a known failure case when two persons wearing a similar set of clothes occlude each other and reemerge in front of the robot. The robot begins to follow the wrong person in such a case. For certain applications, e.g. hospital assistants for doctors, such a failure case cannot be tolerated. Hence, other identification modalities, such as face recoginition or RFID tags or gait recognition, could be investigated as additions to the existing leader tracking and occlusion handling framework.

- **Develop various geometries for predictive fields**. Predictive fields used in our work have all been elliptical, since directionality and speed of obstacle motion are captured well by an elliptical envelope. However, it might be interesting to create different motion models for different types of moving obstacles, e.g. humans, carts, other robots, and develop predictive field geometries specific to each type of motion.

- **Develop a path planner with minimal tuning requirements**. Even with improved workspace and obstacle representation and practical control inputs, the current system requires its navigation gain to be tuned for the robot to converge. Were this requirement to be relaxed, either by learning tuned values over many trials, or by an iterative method such as the one suggested by Filippidis [77], the setup time and effort to run an experiment in a new environment would be greatly reduced.

- **Develop an application specific person following system**. Our person follower was developed as a generic solution for various facets of the problem. However, a specific application such as ‘hospital assistant’ or ‘grocery cart’ will introduce a set of specific design requirements. Such design specifications will, in turn, define additional modules, e.g. speech recognition, telepresence, which will bring the system closer to its intended goal of assisting people in everyday environments.

- **Develop event detection modules to improve navigation behavior**. Since our person follower operates in indoor hallways, its navigation behavior could improve with an ability to detect events which are common to such environments. For example, detecting events such as a door being opened will allow the robot to anticipate the introduction of an obstacle into the workspace, and even in the absence of the physical obstacle, plan a path which takes it away from the door.

In summary, the person following problem provides an interesting set of challenges in terms of robot research and development. In the work presented in this dissertation, methods to address some of these challenges have been developed, and directions for improvements to our system and to the area of person following in general have been identified.

# Bibliography

[1] R. Schraft and G. Schmierer, *Service robots: products, scenarios, visions.* A K Peters, 2000.

[2] R. Kirby, J. Forlizzi, and R. Simmons, "Natural person-following behavior for social robots," in *Proceedings of Human-Robot Interaction*, March 2007, pp. 17–24.

[3] S. Thrun, M. Beetz, M. Bennewitz, W. Burgard, A. Cremers, F. Dellaert, D. Fox, D. Hähnel, C. Rosenberg, N. Roy, J. Schulte, and D. Schulz, "Probabilistic algorithms and the interactive museum tour-guide robot Minerva," *International Journal of Robotics Research*, vol. 19, no. 11, pp. 972–999, 2000.

[4] J. Buhmann, W. Burgard, A. Cremers, D. Fox, T. Hofmann, F. Schneider, J. Strikos, and S. Thrun, "The mobile robot Rhino," *AI Magazine*, vol. 16, no. 1, 1995.

[5] A. Haasch, S. Hohenner, S. Huwel, M. Kleinehagenbrock, S. Lang, I. Toptsis, G. A. Fink, J. Fritsch, B. Wrede, and G. Sagerer, "Biron - the bielefeld robot companion," in *in Proc. Int. Workshop on Advances in Service Robotics*, 2004, pp. 27–32.

[6] M. Takahashi, T. Suzuki, H. Shitamoto, T. Moriguchi, and K. Yoshida, "Developing a mobile robot for transport applications in the hospital domain," *Robotics and Autonomous Systems*, vol. 58, no. 7, pp. 889–899, Jul. 2010.

[7] U. Reiser, C. Connette, J. Fischer, J. Kubacki, A. Bubeck, F. Weisshardt, T. Jacobs, C. Parlitz, M. Hägele, and A. Verl, "Care-o-bot$^{®}$: creating a product vision for service robot applications by integrating design and technology," in *Proceedings of the IEEE Conference on Intelligent Robots and Systems (IROS)*, 2009, pp. 1992–1998.

[8] T. Breuer, G. Giorgana Macedo, R. Hartanto, N. Hochgeschwender, D. Holz, F. Hegger, Z. Jin, C. Mller, J. Paulus, M. Reckhaus, J. lvarez Ruiz, P. Plger, and G. Kraetzschmar, "Johnny: An autonomous service robot for domestic environments," *Journal of Intelligent and Robotic Systems*, vol. 66, no. 1-2, pp. 245–272, 2012.

[9] T. Wisspeintner, T. van der Zant, L. Iocchi, and S. Schiffer, "RoboCup@Home: Scientific competition and benchmarking for domestic service robots," *Interaction Studies*, vol. 10, no. 3, pp. 393–428, 2009.

[10] N. Roy, G. Baltus, D. Fox, F. Gemperle, J. Goetz, T. Hirsch, D. Margaritis, M. Montemerlo, J. Pineau, J. Schulte, and S. Thrun, "Towards personal service robots for the elderly," in *Proceedings of the Workshop on Interactive Robots and Entertainment (WIRE 2000)*, Pittsburgh, PA, May 2000.

[11] H.-M. Gross, C. Schröter, S. Müller, M. Volkhardt, E. Einhorn, A. Bley, C. Martin, T. Langner, and M. Merten, "Progress in developing a socially assistive mobile home robot companion for the elderly with mild cognitive impairment," in *Proceedings of the IEEE Conference on Intelligent Robots and Systems (IROS)*, 2011, pp. 2430–2437.

[12] U.S. Dept. of Health and Human Services, "A profile of older americans: 2012," 2012. [Online]. Available: http://www.aoa.gov/Aging_Statistics/Profile/index.aspx

[13] A. Tani, G. Endo, E. F. Fukushima, S. Hirose, M. Iribe, and T. Takubo, "Study on a practical robotic follower to support home oxygen therapy patients-development and control of a mobile platform-," in *Proceedings of the IEEE Conference on Intelligent Robots and Systems (IROS)*, sept. 2011, pp. 2423 –2429.

[14] K. Kida, "Home oxygen therapy in japan: Clinical application and considerations for practical implementation," *Japan Medical Association Journal*, vol. 54, pp. 99–104, 2011.

[15] D. Feil-Seifer and M. Mataric, "Defining socially assistive robotics," in *Proceedings of the 9th International Conference on Rehabilitation Robotics*, 2005, pp. 465–468.

[16] T. Yoshimi, M. Nishiyama, T. Sonoura, H. Nakamoto, S. Tokura, H. Sato, F. Ozaki, N. Matsuhira, and H. Mizoguchi, "Development of a person following robot with vision based target detection," in *Proceedings of the IEEE Conference on Intelligent Robots and Systems (IROS)*, 2006, pp. 5286–5291.

[17] Z. Chen and S. T. Birchfield, "Person following with a mobile robot using binocular feature-based tracking," in *Proceedings of the IEEE Conference on Intelligent Robots and Systems (IROS)*, Oct. 2007.

[18] W. han Yun, D. Kim, and J. Lee, "Person following with obstacle avoidance based on multi-layered mean shift and force field method," in *Proceedings of the IEEE International Conference on Systems, Man, and Cybernetics (SMC)*, oct. 2010, pp. 3813 –3816.

[19] J. Miura, J. Satake, M. Chiba, K. Ishikawa, K. Kitajima, and H. Masuzawa, "Development of a person following robot and its experimental evaluation," in *Proceedings of the 11th International Conference on Intelligent Autonomous Systems*, 2010, pp. 89–98.

[20] J. Satake and J. Miura, "Robust stereo-based person detection and tracking for a person following robot," in *ICRA Workshop on Person Detection and Tracking*, 2009.

[21] X. Ma, C. Hu, X. Dai, and K. Qian, "Sensor integration for person tracking and following with mobile robot," in *Proceedings of the IEEE Conference on Intelligent Robots and Systems (IROS)*, 2008, pp. 3254–3259.

[22] M. Enzweiler and D. M. Gavrila, "A multilevel mixture-of-experts framework for pedestrian classification," *IEEE Transactions on Image Processing*, vol. 20, no. 10, pp. 2967–2979, 2011.

[23] M. Bansal, S.-H. Jung, B. Matei, J. Eledath, and H. S. Sawhney, "A real-time pedestrian detection system based on structure and appearance classification." in *Proceedings of the IEEE International Conference on Robotics and Automation (ICRA)*, 2010, pp. 903–909.

[24] M. Enzweiler and D. M. Gavrila, "Integrated pedestrian classification and orientation estimation," in *Proceedings of the IEEE Conference on Computer Vision and Pattern Recognition (CVPR)*, 2010, pp. 982–989.

[25] M. Enzweiler, A. Eigenstetter, B. Schiele, and D. M. Gavrila, "Multi-cue pedestrian classification with partial occlusion handling," in *Proceedings of the IEEE Conference on Computer Vision and Pattern Recognition (CVPR)*, 2010, pp. 990–997.

[26] M. Enzweiler and D. M. Gavrila, "Monocular pedestrian detection: Survey and experiments," *IEEE Transactions on Pattern Analysis and Machine Intelligence*, vol. 31, pp. 2179–2195, 2009.

[27] M. D. Breitenstein, F. Reichlin, B. Leibe, E. Koller-Meier, and L. J. V. Gool, "Online multiperson tracking-by-detection from a single, uncalibrated camera," *IEEE Transactions on Pattern Analysis and Machine Intelligence*, vol. 33, no. 9, pp. 1820–1833, 2011.

[28] A. Ess, B. Leibe, K. Schindler, and L. J. V. Gool, "A mobile vision system for robust multi-person tracking," in *Proceedings of the IEEE Conference on Computer Vision and Pattern Recognition (CVPR)*, 2008.

[29] B. Leibe, E. Seemann, and B. Schiele, "Pedestrian detection in crowded scenes," in *Proceedings of the IEEE Conference on Computer Vision and Pattern Recognition (CVPR)*, 2005, pp. 878–885.

[30] B. Wu and R. Nevatia, "Detection and tracking of multiple, partially occluded humans by bayesian combination of edgelet based part detectors," *International Journal of Computer Vision*, vol. 75, no. 2, pp. 247–266, 2007.

[31] J. Shotton, A. W. Fitzgibbon, M. Cook, T. Sharp, M. Finocchio, R. Moore, A. Kipman, and A. Blake, "Real-time human pose recognition in parts from single depth images," in *Proceedings of the IEEE Conference on Computer Vision and Pattern Recognition (CVPR)*, 2011, pp. 1297–1304.

[32] S. Pundlik and S. Birchfield, "Motion-based view-invariant articulated motion detection and pose estimation using sparse point features," in *International Symposium on Visual Computing*, 2009.

[33] B. Daubney, D. Gibson, and N. Campbell, "Real time pose estimation of articulated objects using low-level motion," in *Proceedings of the IEEE Conference on Computer Vision and Pattern Recognition (CVPR)*, July 2008.

[34] J. Brookshire, "Person following using histograms of oriented gradients," *International Journal of Social Robotics*, vol. 2, pp. 137–146, 2010.

[35] C. Weinrich, M. Volkhardt, M. Einhorn, and H.-M. Gross, "Prediction of human avoidance behavior by lifelong learning for socially compliant robot navigation," in *Proceedings of the IEEE International Conference on Robotics and Automation (ICRA)*, 2013, pp. 376–381.

[36] C. Weinrich, C. Vollmer, and H.-M. Gross, "Estimation of human upper body orientation for mobile robotics using an svm decision tree on monocular images," in *Proceedings of the IEEE Conference on Intelligent Robots and Systems (IROS)*, 2012, pp. 2147–2152.

[37] N. Dalal and B. Triggs, "Histograms of oriented gradients for human detection," in *Proceedings of the IEEE Conference on Computer Vision and Pattern Recognition (CVPR)*, 2005, pp. 886–893.

[38] M. C. Martin, "Evolving visual sonar: Depth from monocular images," *Pattern Recognition Letters: Evolutionary Computer Vision and Image Understanding*, vol. 27, no. 11, pp. 1174 – 1180, August 2006.

[39] A. Saxena, S. H. Chung, and A. Y. Ng, "Learning depth from single monocular images," in *NIPS 18*. MIT Press, 2005.

[40] L. Xia, C. Chen, and J. Aggarwal, "Human detection using depth information by kinect," in *Computer Vision and Pattern Recognition Workshops (CVPRW), 2011 IEEE Computer Society Conference on*, 2011, pp. 15–22.

[41] G. Doisy, A. Jevtic, E. Lucet, and Y. Edan, "Adaptive person-following algorithm based on depth images and mapping," in *Proceedings of the Workshop on Robot Motion Planning: Online, Reactive, and in Real-time, IEEE/RSJ International Conference on Intelligent Robots and Systems (IROS 2012)*, 2012.

[42] G. Shu, A. Dehghan, O. Oreifej, E. Hand, and M. Shah, "Part-based multiple-person tracking with partial occlusion handling," in *Proceedings of the IEEE Conference on Computer Vision and Pattern Recognition (CVPR)*, 2012, pp. 1815–1821.

[43] A. Elgammal and L. Davis, "Probabilistic framework for segmenting people under occlusion," in *Proceedings of the IEEE International Conference on Computer Vision (ICCV)*, vol. 2, 2001, pp. 145–152 vol.2.

[44] M. Tarokh and P. Merloti, "Vision-based robotic person following under light variations and difficult walking maneuvers," *Journal of Field Robotics*, vol. 27, no. 4, pp. 387–398, 2010.

[45] A. Treuille, S. Cooper, and Z. Popović, "Continuum crowds," in *SIGGRAPH '06: ACM SIGGRAPH 2006*, 2006, pp. 1160–1168.

[46] P. Henry, C. Vollmer, B. Ferris, and D. Fox, "Learning to navigate through crowded environments," in *Proceedings of the IEEE International Conference on Robotics and Automation (ICRA)*, 2010.

[47] P. Trautman and A. Krause, "Unfreezing the robot: Navigation in dense, interacting crowds," in *Proceedings of the IEEE Conference on Intelligent Robots and Systems (IROS)*, 2010.

[48] B. D. Ziebart, N. Ratliff, G. Gallagher, C. Mertz, K. Peterson, J. A. D. Bagnell, M. Hebert, A. Dey, and S. Srinivasa, "Planning-based prediction for pedestrians," in *Proceedings of the IEEE Conference on Intelligent Robots and Systems (IROS)*, October 2009.

[49] M. Bennewitz, W. Burgard, G. Cielniak, and S. Thrun, "Learning motion patterns of people for compliant robot motion," *International Journal of Robotic Research*, vol. 24, no. 1, pp. 31–48, 2005.

[50] S. M. LaValle, *Planning Algorithms.* Cambridge University Press, 2006.

[51] H. Durrant-Whyte and T. Bailey, "Simultaneous localization and mapping (SLAM): part I," *Robotics Automation Magazine, IEEE*, vol. 13, no. 2, pp. 99–110, 2006.

[52] T. Bailey and H. Durrant-Whyte, “Simultaneous localization and mapping (SLAM): part II,” *Robotics Automation Magazine, IEEE*, vol. 13, no. 3, pp. 108–117, 2006.

[53] F. Steinbruecker, J. Sturm, and D. Cremers, “Real-time visual odometry from dense rgb-d images,” in *Workshop on Live Dense Reconstruction with Moving Cameras at the Intl. Conf. on Computer Vision (ICCV)*, 2011.

[54] D. Nistér, O. Naroditsky, and J. R. Bergen, “Visual odometry,” in *Proceedings of the IEEE Conference on Computer Vision and Pattern Recognition (CVPR)*, 2004, pp. 652–659.

[55] K. S. Arun, T. S. Huang, and S. D. Blostein, “Least-squares fitting of two 3D point sets,” *IEEE Transactions on Pattern Analysis and Machine Intelligence*, vol. 9, no. 5, pp. 698–700, May 1987.

[56] P. J. Besl and N. D. McKay, “A method for registration of 3-d shapes,” *IEEE Transactions on Pattern Analysis and Machine Intelligence*, vol. 14, no. 2, pp. 239–256, Feb. 1992.

[57] A. Diosi and L. Kleeman, “Fast laser scan matching using polar coordinates,” *International Journal of Robotic Research*, vol. 26, no. 10, pp. 1125–1153, Oct 2007.

[58] E. Olson, “Real-time correlative scan matching,” in *Proceedings of the IEEE International Conference on Robotics and Automation (ICRA)*, June 2009, pp. 4387–4393.

[59] B. Peasley, S. T. Birchfield, A. Cunningham, and F. Dellaert, “Accurate on-line 3D occupancy grids using manhattan world constraints,” in *Proceedings of the IEEE Conference on Intelligent Robots and Systems (IROS)*, 2012, pp. 5283–5290.

[60] Y. Furukawa, B. Curless, S. M. Seitz, and R. Szeliski, “Manhattan-world stereo,” in *Proceedings of the IEEE Conference on Computer Vision and Pattern Recognition (CVPR)*, 2009, pp. 1422–1429.

[61] E. Rimon and D. Koditschek, “Exact robot navigation using artificial potential functions,” *IEEE Transactions on Robotics and Automation*, vol. 8, no. 5, pp. 501–518, 1992.

[62] O. Khatib, “Real-time obstacle avoidance for manipulators and mobile robots,” *International Journal of Robotic Research*, vol. 5, no. 1, pp. 90–98, 1986.

[63] R. Arkin, “Motor schema based navigation for a mobile robot: An approach to programming by behavior,” in *Proceedings of the IEEE International Conference on Robotics and Automation (ICRA)*, vol. 4, Mar. 1987, pp. 264–271.

[64] B. Krogh and C. Thorpe, "Integrated path planning and dynamic steering control for autonomous vehicles," in *Proceedings of the IEEE International Conference on Robotics and Automation (ICRA)*, April 1986, pp. 1664 – 1669.

[65] Y. Koren and J. Borenstein, "Potential field methods and their inherent limitations for mobile robot navigation," in *Proceedings of the IEEE International Conference on Robotics and Automation (ICRA)*, 1991, pp. 1398–1404.

[66] J. Hagelbäck and S. J. Johansson, "Using multi-agent potential fields in real-time strategy games," in *Proceedings of the 7th international joint conference on Autonomous agents and multiagent systems - Volume 2*, ser. AAMAS '08, 2008, pp. 631–638.

[67] S. S. Ge and Y. J. Cui, "Dynamic motion planning for mobile robots using potential field method," *Autonomous Robots*, vol. 13, pp. 207–222, 2002.

[68] E. Rimon and D. Koditschek, "The construction of analytic diffeomorphisms for exact robot navigation on star worlds," *Transactions of the American Mathematical Society*, vol. 327, no. 1, pp. 71–115, 1991.

[69] D. Koditschek, "The control of natural motion in mechanical systems," *ASME Journal of Dynamic Systems, Measurement, and Control*, vol. 113, no. 4, pp. 547–551, 1991.

[70] D. Koditschek and E. Rimon, "Robot navigation functions on manifolds with boundary," *Advances in Applied Mathematics*, vol. 11, no. 4, pp. 412–442, 1990.

[71] H. Tanner and A. Boddu, "Multi-agent navigation functions - have we missed something?" University of Delaware, Tech. Rep., 2010. [Online]. Available: http://dspace.udel.edu:8080/dspace/handle/19716/5657

[72] J. Chen, D. Dawson, M. Salah, and T. Burg, "Cooperative control of multiple vehicles with limited sensing," *International Journal of Adaptive Control and Signal Processing*, vol. 21, no. 2-3, pp. 115–131, 2007.

[73] H. Tanner, S. Loizou, and K. Kyriakopoulos, "Nonholonomic navigation and control of cooperating mobile manipulators," *IEEE Transactions on Robotics and Automation*, vol. 19, no. 1, pp. 53 – 64, feb 2003.

[74] A. Widyotriatmo and K.-S. Hong, "Navigation function-based control of multiple wheeled vehicles," *IEEE Transactions on Industrial Electronics*, vol. 58, no. 5, pp. 1896–1906, 2011.

[75] I. Filippidis, K. J. Kyriakopoulos, and P. K. Artemiadis, "Navigation functions learning from experiments: Application to anthropomorphic grasping," in *Proceedings of the IEEE International Conference on Robotics and Automation (ICRA)*, may 2012.

[76] I. Filippidis and K. J. Kyriakopoulos, "Navigation functions for everywhere partially sufficiently curved worlds," in *Proceedings of the IEEE International Conference on Robotics and Automation (ICRA)*, May 2012, pp. 2115–2120.

[77] I. Filippidis and K. Kyriakopoulos, "Adjustable navigation functions for unknown sphere worlds," in *Proceedings of IEEE Conference on Decision and Control and European Control Conference (CDC-ECC)*, dec. 2011, pp. 4276 –4281.

[78] N. Pradhan, T. C. Burg, S. T. Birchfield, and U. Hasirci, "Indoor navigation for mobile robots using predictive fields," in *Proceedings of the American Control Conference (ACC)*, June 2013.

[79] N. Pradhan, T. C. Burg, and S. T. Birchfield, "Robot crowd navigation using predictive position fields in the potential function framework," in *Proceedings of the American Control Conference (ACC)*, June 2011, pp. 4628–4633.

[80] P. Melchior, B. Metoui, S. Najar, M. Abdelkrim, and A. Oustaloup, "Robust path planning for mobile robot based on fractional attractive force," in *Proceedings of the American Control Conference (ACC)*. Piscataway, NJ, USA: IEEE Press, 2009, pp. 1424–1429.

[81] A. Poty, P. Melchior, and A. Oustaloup, "Dynamic path planning by fractional potential," in *IEEE International Conference on Computational Cybernetics*, 2004.

[82] ——, "Dynamic path planning for mobile robots using fractional potential field," in *International Symposium on Control, Communications and Signal Processing*, 2004, pp. 557 – 561.

[83] S. S. Ge and Y. Cui, "New potential functions for mobile robot path planning," *IEEE Transactions on Robotics and Automation*, vol. 16, no. 5, pp. 615–620, 2000.

[84] J. Chen, D. Dawson, M. Salah, and T. Burg, "Multiple uav navigation with finite sensing zone," in *Proceedings of the American Control Conference (ACC)*, June 2006.

[85] J. Chen, D. M. Dawson, M. Salah, and N. Pradhan, "Multiple uav navigation with finite sensor range," Clemson University, Clemson, SC, USA, Tech. Rep., 2005. [Online]. Available: http://www.clemson.edu/ces/crb/publictn/tr.htm

[86] R. Saber and R. Murray, "Flocking with obstacle avoidance: cooperation with limited communication in mobile networks," in *Proceedings of the IEEE Conference on Decision and Control (CDC)*, vol. 2, 2003, pp. 2022 – 2028 Vol.2.

[87] J. J. Slotine and W. Li, *Applied Nonlinear Control.* Prentice Hall, 1991.

[88] D. Eberly, "Least squares fitting of data," 1999. [Online]. Available: http://www.geometrictools.com/Documentation/LeastSquaresFitting.pdf

[89] Microsoft Corp., "Microsoft kinect," 2010. [Online]. Available: http://www.xbox.com/en-US/kinect

[90] ——, "Kinect for windows SDK," 2011. [Online]. Available: http://www.microsoft.com/en-us/kinectforwindows/develop/new.aspx

[91] D. S. Alexiadis, P. Kelly, P. Daras, N. E. O'Connor, T. Boubekeur, and M. B. Moussa, "Evaluating a dancer's performance using kinect-based skeleton tracking," in *Proceedings of the 19th ACM international conference on Multimedia*, 2011, pp. 659–662.

[92] P. Yanik, J. Manganelli, J. Merino, A. Threatt, J. Brooks, K. Green, and I. Walker, "Use of kinect depth data and growing neural gas for gesture based robot control," in *Pervasive Computing Technologies for Healthcare (PervasiveHealth), 2012 6th International Conference on*, 2012, pp. 283–290.

[93] M. Reyes, G. Dominguez, and S. Escalera, "Featureweighting in dynamic time-warping for gesture recognition in depth data," in *Computer Vision Workshops (ICCV Workshops), 2011 IEEE International Conference on*, 2011, pp. 1182–1188.

[94] R. C. Gonzalez and R. E. Woods, *Digital Image Processing*, 2nd ed. Boston, MA, USA: Addison-Wesley Longman Publishing Co., Inc., 2001.

[95] A. Ford and A. Roberts, "Color space conversions," 1998. [Online]. Available: http://www.poynton.com/PDFs/coloureq.pdf

[96] M. Stokes, M. Anderson, S. Chandrasekar, and R. Motta, "A standard default color space for the internet — srgb," November 1996. [Online]. Available: http://www.color.org/contrib/sRGB.html

[97] D. G. Lowe, "Distinctive image features from scale-invariant keypoints," *International Journal of Computer Vision*, vol. 60, no. 2, pp. 91–110, 2004.

[98] H. Bay, A. Ess, T. Tuytelaars, and L. Van Gool, "Speeded-up robust features (surf)," *Comput. Vis. Image Underst.*, vol. 110, no. 3, pp. 346–359, jun 2008.

[99] S. T. Birchfield and S. J. Pundlik, "Joint tracking of features and edges," in *Proceedings of the IEEE Conference on Computer Vision and Pattern Recognition (CVPR)*, 2008.

[100] S. Leutenegger, M. Chli, and R. Siegwart, “Brisk: Binary robust invariant scalable keypoints,” in *Proc. of the IEEE International Conference on Computer Vision (ICCV)*, 2011.

[101] R. B. Rusu and S. Cousins, “3D is here: Point cloud library (pcl),” in *Proceedings of the IEEE International Conference on Robotics and Automation (ICRA)*, may 2011.

[102] A. Geiger, P. Lenz, and R. Urtasun, “Are we ready for autonomous driving? the kitti vision benchmark suite,” in *Proceedings of the IEEE Conference on Computer Vision and Pattern Recognition (CVPR)*, 2012.

[103] R. B. Rusu, N. Blodow, and M. Beetz, “Fast point feature histograms (FPFH) for 3D registration,” *Proceedings of the IEEE International Conference on Robotics and Automation (2009)*, pp. 3212–3217, 2009.

[104] H. Moravec and A. Elfes, “High resolution maps from wide angle sonar,” in *Proceedings of the IEEE International Conference on Robotics and Automation (ICRA)*, vol. 2, 1985, pp. 116–121.

[105] F. Lu and E. Milios, “Robot pose estimation in unknown environments by matching 2d range scans,” *Journal of Intelligent Robotics Systems*, vol. 18, no. 3, pp. 249–275, Mar. 1997.

[106] M. A. Fischler and R. C. Bolles, “Random sample consensus: A paradigm for model fitting with applications to image analysis and automated cartography,” *Communications of the ACM*, vol. 24, no. 6, pp. 381–395, 1981.

[107] M. Zuliani, “RANSAC for dummies,” University of California at Santa Barbara, Santa Barbara, USA, Tech. Rep., 2011.